Spring 5-2022

Understanding Biogeochemical and Physical Controls on Methane Air-Sea Exchange Fluxes in the Pacific Ocean

Sarah Raney

Understanding Biogeochemical and Physical Controls on Methane Air-Sea Exchange Fluxes in the Pacific Ocean

by

Sarah Elizabeth Raney

A Thesis
Submitted to the Graduate School,
the College of Arts and Sciences
and the School of Ocean Science and Engineering
at The University of Southern Mississippi
in Partial Fulfillment of the Requirements
for the Degree of Master of Science

Approved by:

Dr. Alan Shiller, Committee Chair
Dr. Christopher Hayes
Dr. Kevin Dillon

May 2022

Published by the Graduate School

ABSTRACT

Methane and trace element samples were collected on GEOTRACES GP15 Pacific Meridional Transect (PMT) cruise conducted between the Aleutian Islands (57 °N) and Tahiti (20 °S) from September to November 2018. Uncertainty in methane air-sea exchange fluxes was determined using a propagation of errors approach. Fluxes ranged from -0.88 to 4.9 μmol CH_4 m^{-2} d^{-1}. Average CH_4 flux along the Alaskan margin was 2.2 ± 2.9 μmol CH_4 m^{-2} d^{-1}. Methane fluxes decreased moving southward and increased to their open ocean maximum around 20 °N before declining in equatorial waters. Near 20 °N, phosphorus-limiting conditions were observed, suggesting methylphosphonate (MPn) utilization may have occurred to elevate CH_4 fluxes. Methane fluxes measured at open ocean stations ranged from -0.31 to 2.9 μmol CH_4 m^{-2} d^{-1}, matching those reported in previous studies. Atmospheric methane and near-surface dissolved methane concentrations differed significantly between the hemispheres (paired Student's t test, $p < 0.01$). The temperate North Pacific average CH_4 fluxes (0.40 ± 0.76 μmol CH_4 m^{-2} d^{-1}) significantly differed from average fluxes measured in the subtropical North Pacific (1.5 ± 0.80 μmol CH_4 m^{-2} d^{-1}; $p < 0.01$) and the equatorial Pacific (0.92 ± 0.44 μmol CH_4 m^{-2} d^{-1}; $p < 0.05$). Lanthanum (La) to ytterbium (Yb) ratios and light rare earth element (LREEs) to heavy (HREEs) ratios were lower in South Pacific compared to North Pacific, indicating possible methane oxidation through use of LREEs as enzyme co-factors.

ACKNOWLEDGMENTS

I would like to thank my adviser, Dr. Alan Shiller, and my committee members Dr. Christopher Hayes and Dr. Kevin Dillon. I would also like to thank Dr. Laura Whitmore, Dr. Virginie Sanial, and Melissa Gilbert for data collection and processing as well as their feedback regarding data analysis. I appreciate the input I received from the following colleagues regarding this work: Amy Moody, Dr. Shaily Rahman, Neil Redmond, Allison Savoie, Bryce Melzer, and Bethany Pertain. I would like to acknowledge the chief scientists of the GEOTRACES GP15 Pacific Meridional Transect cruise as well as captain and crew of the R/V Roger Revelle for making the collection of these data possible. This work was funded by NSF Chemical Oceanography Program grant OCE 1737024.

DEDICATION

I would like to dedicate this work to my family. Thank you to my parents, Bill and Laura, my brother, Danny, and my grandma, Dianne, for inspiring me and for your unwavering encouragement. I would also like to thank my partner, Bryce, and my friends for making the journey more enjoyable. Your support has made this work possible.

TABLE OF CONTENTS

LIST OF TABLES

LIST OF ILLUSTRATIONS

CHAPTER I - INTRODUCTION

Methane (CH_4) is a potent greenhouse gas and the most abundant hydrocarbon in the atmosphere. The National Oceanic and Atmospheric Administration Global Monitoring Laboratory (NOAA GML) reported that atmospheric CH_4 concentrations reached 1900.5 ppb in September 2021 (Dlugokencky 2021), which is roughly a 2.5 factor increase from pre-industrial concentrations of 722 ppb (Ciais et al. 2013). Methane has contributed to roughly 20% of Earth's warming since pre-industrial times (Karl et al. 2008) and has a 100-year warming potential that is ~23 times that of carbon dioxide (Hartmann et al. 2013). The ocean contributes 1-4% of annual global CH_4 emissions, yet a lack of knowledge regarding oceanic CH_4 contributes to uncertainty in the global CH_4 budget (Hamdan and Wickland 2016; Kirschke et al. 2013; Reeburgh 2007). Changes to CH_4 distribution in the ocean and the ocean's storage capacity have occurred in the geologic past (i.e., Paleocene Eocene Thermal Maximum) and may occur in the future with anthropogenic climate change (e.g., Zachos et al. 2001; Zachos et al. 2008).

The ocean acts as an important reservoir of CH_4, a critically important source, and plays a crucial role in the global carbon cycle. Supersaturation of CH_4 relative to the atmosphere is common in the ocean, particularly in the mixed layer. This raises the question of why the ocean is not a more significant source of CH_4 to the atmosphere. Microbially mediated oxidation of CH_4 acts as a significant sink, resulting in only minor releases of CH_4 to the atmosphere over much of the ocean (Valentine 2011; Reeburgh 2007; Chan et al. 2019). Furthermore, rates of CH_4 oxidation likely limit the amount of CH_4 that reaches the atmosphere from oceanic sources (Pack et al. 2015; Ciais et al. 2013; Zhang et al. 2011). Analyzing oceanic sources and sinks of CH_4 is essential for

understanding the controls on the CH_4 balance. Changes to this balance have potential repercussions for the climate (Ruppel & Kessler 2017). Furthermore, understanding today's baselines and controls on CH_4 distribution can aid in predictions regarding global climate change. Although our knowledge of CH_4 in the ocean is increasing, high uncertainty regarding CH_4 in the marine environment persists due to sparse sampling. Coastal CH_4 emissions and CH_4 seeps have often received greater research attention than the open ocean (e.g., Weber et al. 2019; Chan et al. 2019; Valentine et al. 2001). As a result, many questions remain regarding CH_4 distribution in the open ocean.

This thesis seeks to fill in existing knowledge gaps regarding scientific understanding of the oceanic distribution of CH_4, air-sea exchange fluxes, and other processes that affect CH_4 in the marine environment, with a particular focus on the open ocean. Samples were collected aboard the GEOTRACES GP15 Pacific Meridional Transect (PMT) cruise, spanning coastal and open ocean stations in the Pacific Ocean. Studying a transect of stations in the Pacific Ocean may facilitate greater understanding of the processes that control CH_4 distribution. By comparing CH_4 measurements to physical and biogeochemical parameters, we can elucidate the controls on CH_4 air-sea exchange fluxes in the Pacific Ocean. Atmospheric, benthic, and coastal CH_4 sources were anticipated to be the primary drivers of high CH_4 concentrations in the collected samples, while CH_4 oxidation was expected to be the primary CH_4 sink.

CHAPTER II – REVIEW OF RELATED LITERATURE

To understand the ocean's role in supplying CH_4 to the atmosphere, it is necessary to examine the known sources and sinks. The following section outlines the important sources of CH_4 in coastal and open ocean waters, specifically the Pacific Ocean, as well as the major sinks in these regions. Better constraining the oceanic CH_4 budget will promote greater accuracy in the global CH_4 budget. Important questions for the future are why the ocean does not supply more CH_4 to the atmosphere and how might the source term of atmospheric evasion increase with global climate change?

2.1 OCEANIC METHANE SOURCES

2.1.1 SOURCES FROM THE ATMOSPHERE

There are often physical processes resulting in surface mixed layer waters being supersaturated with CH_4 relative to the atmosphere. Some examples include air injection and variations in seasonal cooling. However, CH_4 has a limited change in solubility with temperature change, so seasonal temperature changes may have a minimal effect on CH_4 concentrations in the upper water column (Wanninkof 2014; Wiesenburg and Guinasso 1979). Bubble entrainment is another method of CH_4 injection from the atmosphere, referring to bubble generation and release. When wind speeds are high (e.g., > 15 m s^{-1}), atmospheric invasion fluxes are higher and can introduce more bubbles than under intermediate wind speeds (e.g., 3-15 m s^{-1}; Wanninkhof 2014). Dissolution of bubbles, either partial or total, can introduce CH_4 to the water column, resulting in supersaturation relative to the atmosphere (Reeburgh 2007).

2.1.2 COASTAL, WATER COLUMN, AND BENTHIC SOURCES

Coastal sources may contribute up to 75% of the global oceanic CH_4 emissions to the atmosphere (Bange et al. 1994; Weber et al. 2019). Supersaturations of greater than 200% are common on continental shelves and productive upwelling zones (Weber et al. 2019; Bange et al. 1994; Reeburgh 2007). These regions can have especially high CH_4 concentrations (i.e., supersaturations of ~20 nM) due to fluxes of organic matter (OM) and development of anoxic sediments (Reebugh 2007; Popp et al. 1995; Bange et al. 1994). Export production transfers OM to the sediments. With enough OM accumulation and rapid depletion of oxygen through microbial respiration, anoxic conditions can persist. Methanogenesis is the biological production of CH_4 through anaerobic remineralization of OM. When oxygen is depleted, microbes utilize anaerobic respiration to break down OM. Methanogenesis is the final redox reaction in the chain of potential electron acceptors for respiration. Using organic carbon (OC) as the electron acceptor, CH_4 is generated as a byproduct of fermentation. Acetate or H_2 generated from the breakdown of OC is thought to be important for CH_4 fermentation (Reeburgh 2007). Resuspension, diffusion, and ebullition from anoxic sediments can introduce CH_4 into the water column (Reeburgh 2007), resulting in supersaturated waters with respect to the atmosphere. In some cases, ebullition may drive a diffusive flux to the atmosphere (McGinnis et al. 2006; Weber et al. 2019). However, this process is generally of minor importance in the oceanic CH_4 budget due to the limited conditions under which bubbles released from the sediments would reach the surface and exchange with the atmosphere (Reeburgh 2007; Hamdan & Wickland 2016).

Advection along the continental shelf can also generate CH_4 plumes from benthic sources (Charlou et al. 1998; Reeburgh 2007). Manganese (Mn) concentrations can be indicative of benthic sources from anoxic sediments. Mn facilitates redox reactions by acting as an electron acceptor in anaerobic respiration. In anoxic sediments where methanogenesis occurs, Mn will have already been utilized for anaerobic respiration through use of MnO_2 or Mn(IV) because it is thermodynamically more favorable than methanogenesis, and Mn^{2+} is a product of this reaction. Aqueous Mn^{2+} can diffuse into the water column, potentially resulting in high Mn concentrations at the sediment-water interface. Coinciding signals of high CH_4 and high Mn concentrations near the sediment water interface suggest a benthic flux due to sediment resuspension or diffusion (e.g., Zhang et al. 2011).

Frequently, CH_4 can have two or more maxima on the continental shelf: one in or just below the mixed layer (Ward 1992) and the second at the base of the euphotic zone yet above the sediment-seawater interface (Popp et al. 1995; Cynar & Yayanos 1992; Reeburgh 2007). The mixed layer maximum may be associated with microbially mediated methanogenesis in microenvironments on zooplankton fecal pellets (Tilbrook & Karl 1995; Schmale et al. 2018). Previous studies have noted water column CH_4 maxima at the pycnocline (~50-150 m) (Bates et al. 1996; Scranton & Brewer 1977; Burke Jr. et al. 1983). Furthermore, pronounced oxygen minimum zones (OMZs) or "shadow zones" below highly productive surface waters may coincide with a CH_4 maxima at the bottom of the euphotic zone (Reeburgh 2007). Higher loads of sinking OM fuel aerobic respiration, which depletes oxygen. Microenvironments associated with sinking OM may facilitate anaerobic methanogenesis (Tilbrook & Karl 1995; Schmale et al. 2018), which

may produce a CH_4 supersaturation of less than 5 nM (Reeburgh 2007). Coinciding signals of high CH_4 and low oxygen may be observed within the pycnocline and in waters below up to ~1500 m (e.g., Scranton & Brewer 1977; Burke Jr. et al. 1983). However, it is likely to be a result of physical processes limiting resupply of oxygen, which could help facilitate anaerobic respiration, although anoxia is unlikely to occur in the water column.

While coastal runoff and upwelling may stimulate planktonic sources that contribute to CH_4 supersaturation along continental shelves (Ward 1992; Cynar and Yayanos 1992), these sources do not explain CH_4 supersaturations up to 120% in the open ocean (Bange et al. 1994; Karl et al. 2008; Tilbrook & Karl 1995). The trend of CH_4 supersaturation extends to open ocean surface waters but breaks down near the equator, which may be a result of changes in stratification regime with increasing precipitation in the tropics (Reeburgh 2007; Karl et al. 2008).

Archaea have traditionally been considered the only methanogens; however, recent research suggests that CH_4 production occurs in all three domains of life: Bacteria, Archaea, and Eukarya (e.g., Bižić et al. 2020, Klintzsch et al. 2019; Lenhart et al. 2016; Repeta et al. 2016; Sosa et al. 2019). Research by Bižić et al. (2020) suggests that cyanobacteria play a role in the marine CH_4 cycle that needs to be further investigated. Suggested pathways for how cyanobacteria produce CH_4 include demethylation of methylphosphonate (MPn) or symbiotic relationships with methanogenic archaea (Bižić et al. 2020). Cyanobacteria are not the only marine phytoplankton that produce CH_4. Marine algae, such as the coccolithophore *Emiliania huxleyi* and haptophytes *Phaeocystis globosa* and *Chrysochromulina sp.* produce CH_4 under oxic conditions (Klintzsch et al.

2019; Lenhart et al. 2016). Marine phytoplankton CH_4 production assuredly contributes to CH_4 supersaturation in the mixed layer but is likely not the only source of CH_4 (Klintzsch et al. 2019; Bižić et al. 2020; Lenhart et al. 2016). The rapid response of CH_4 production to light conditions suggests that it may be tied to photosynthesis, possibly through the photosynthetic electron transfer chain (Bižić et al. 2020), but the exact mechanism has not yet been determined.

In phosphorus-depleted regions (i.e., the majority of the open ocean), MPn can be used as a sole source of phosphorus for aerobic growth in some organisms, which, in turn, releases CH_4 (Karl et al. 2008; White & Metcalf 2007; Metcalf et al. 2012; Sosa et al. 2019). Therefore, MPn utilization by microbes can serve as a CH_4 source in P-limited waters. Karl et al. (2008) observed rapid MPn consumption and production of CH_4 in the Pacific Ocean. For samples where phosphate was added, they observed lower rates of CH_4 production compared to P-limited conditions where MPn utilization was measured. Their results suggest that when phosphate is less limiting, perhaps MPn decomposition is inhibited or does not proceed as quickly as it would in phosphate-stressed conditions, resulting in a decrease in CH_4 production. Repeta et al. (2016) demonstrated that the observed CH_4 production occurred via C-P lyase pathways. Finally, they suggested that only 0.25% of the daily cycled dissolved organic matter (DOM) polysaccharide pool needed to be metabolized to support the measured CH_4 supersaturation fluxes (Repeta et al. 2016). It seems likely that in at least some regions of the marine system, coupling of the CH_4 cycle with decomposition of MPn can explain CH_4 supersaturations in oligotrophic regions (Karl et al. 2008; Repeta et al. 2016; Metcalf et al. 2012). Although

open ocean sources may produce lower CH_4 concentrations than coastal sources, they are a critical component of the oceanic CH_4 budget and require further research.

2.1.3 HYDROTHERMAL AND SEEP SOURCES

Hydrothermal activity is a source of abiotic CH_4 production (Reeburgh 2007). Plumes with concentrations up to ~50 nM have been observed near hydrothermal vents (Charlou et al. 1998). Loihi Seamount, which is included in the GP15 transect, appears to provide a minor source of CH_4 to intermediate waters (Jenkins et al. 2020). Hydrothermal activity at Loihi is not anticipated to affect surface water CH_4 concentrations. Natural CH_4 seeps can also introduce CH_4 supersaturations at depth (Hamdan & Wickland 2016).

2.2 OCEANIC METHANE SINKS

2.2.1 AEROBIC OXIDATION

Aerobic oxidation of CH_4 is microbially-mediated and one of the primary sinks of CH_4 in marine waters (Hamdan & Wickland 2016). Methanotrophy, or methane oxidation, drives CH_4 undersaturation in most of the oceanic water column (Karl et al. 2008; Reeburgh 2007). In the Eastern Tropical North Pacific, rates of CH_4 oxidation ranged from 3.4×10^{-5} to 4 nmol CH_4 L^{-1} d^{-1} (Pack et al. 2015). Previously reported rates of CH_4 oxidation ranged from 0.001 to 10 nmol CH_4 L^{-1} d^{-1} at an Arctic fjord in Norway (Mau et al. 2013). Chan et al. (2019) observed CH_4 concentrations ranging from 2.9 to 79 nmol kg^{-1} near an active CH_4 seep in Hudson Canyon. Research by Chan et al. (2019) documented the kinetics of methanotrophy as a first order process and first-order

oxidation rate constants on CH_4 seeps average of 0.22 ± 0.05 d^{-1} and an off-seep average of 0.12 ± 0.09 d^{-1}. In their mesocosm experiments, removal of an average of 90 ± 40 µmol L^{-1} of CH_4 over the course of the incubation was observed (Chan et al. 2019). Additional studies following the Deepwater Horizon Blowout in the Gulf of Mexico documented elevated rates of methanotrophy reaching up to 5,900 nmol L^{-1} d^{-1} in the months following (e.g., Crespo-Medina et al. 2014). In coastal regions, CH_4 oxidation rates would be expected to mimic rates similar to those reported by Mau et al. (2013) or higher like those reported in Chan et al. (2019). For open ocean Pacific stations without additional sources of CH_4 (i.e., coastal, or benthic), CH_4 oxidation rates similar to those reported by Pack et al. (2015) would be expected, which ranged from near-zero to 4 nmol CH_4 L^{-1} d^{-1}.

There are two important enzymes involved in aerobic oxidation: methane monooxygenases (MMOs) and methanol dehydrogenase (MDH). Methanotrophs use MMOs to convert CH_4 to methanol. Methanotrophs use MDH to oxidize methanol. There are at least two forms of MDH and MMO. Only two forms of MMOs: soluble methane monooxygenase (sMMO) and particulate methane monooxygenase (pMMO), will be discussed here. Placement within the cell varies: sMMO is cytoplasmic, whereas pMMO is membrane bound (Semrau et al. 2018). In the case of methanotrophs that can express both forms, a “copper (Cu) switch” controls which is expressed. pMMO is more efficient because it has a greater affinity for CH_4; it also uses Cu as a co-factor (Semrau et al. 2018). On the other hand, sMMO has a higher maximum turnover rate of CH_4 and tends to be expressed under Cu deficient conditions (Semrau et al. 2018). Given the proclivity

of pMMO for CH_4 and use of Cu as a co-factor, depletions in Cu may be an indicator of aerobic oxidation of CH_4 in the mixed layer (Semrau et al. 2018).

The second step of CH_4 oxidation is catalyzed by MDH, which oxidizes methanol. Some methanotrophs use light rare earth elements (LREEs) or lanthanides as co-factors in MDH. Additionally, the LREEs appear to be more commonly incorporated into MDH than the heavy REEs (HREEs). The enzyme has at least two homologs: MxaF and XoxF. MxaF is Ca^{2+} dependent and incorporates Cu and Fe as co-factors (Chistoserdova 2019; Kalyuzhnaya et al. 2013), while XoxF uses LREEs as co-factors (Semrau et al. 2018; Pol et al. 2014), which include lanthanum (La), cerium (Ce), praseodymium (Pr), and neodymium (Nd). La appears to be the most important co-factor for XoxF (Semrau et al. 2018). The lanthanides behave similarly to Ca^{2+}; however, they are stronger Lewis acids, meaning they are more efficient catalysts for hydrolysis (Lim & Franklin 2004; Semrau et al. 2018), which may explain why they are also used as a co-factor in MDH. In microbes that contain genes for both MDH types, a "lanthanide switch" activates the XoxF gene and inhibits the MxaF gene (Semrau et al. 2018; Daumann 2019). The XoxF type of MDH has greater efficiency and is preferentially used when LREEs are present in sufficient abundance (Daumann 2019; Semrau et al. 2018). Methanotrophy may also have a coinciding signal of LREE depletion as was observed by Shiller et al. (2017) following the Deepwater Horizon blowout. Meyer et al. (2021) observed LREE depletions relative to HREEs (REEs with an atomic mass greater than 147 i.e., Sm, Eu, Gd, Tb, Dy, Ho, Er, Tm, Yb and Lu) in the upper water column (~200-500 m) in the Sargasso Sea. Additional studies have indicated that La, Ce, Pr, Nd, and

samarium (Sm) may be important co-factors in the oxidation of CH_4 and methanol (Huang et al. 2018; Picone & Op den Camp 2019; Pol et al. 2014; De Baar et al. 2018).

In marine water columns, CH_4 concentration can reach a maximum of ~20 nmol L^{-1} (Bange et al. 1994). Removal through CH_4 oxidation has been observed in the range of days to months (DeAngelis et al. 1993; Valentine et al. 2001; Ward & Kilpatrick 1993). Chan et al. (2019) observed that it took weeks for the microbial community to respond to the addition of CH_4 in mesocosm experiments. However, once microbes associated with methanotrophy bloomed, CH_4 oxidation proceeded rapidly with increased rates. As CH_4 concentrations are much lower throughout much of the ocean than those near CH_4 seeps, slower turnover rates would be expected. These studies provide support that aerobic oxidation of CH_4 occurs rapidly in the water column. Additionally, aerobic oxidation may take place in oxic sediments at the benthic boundary layer as well as in oxic waters surrounding hydrothermal vents (Reeburgh 2007). Aerobic oxidation is likely the primary driver of CH_4 undersaturation in the deep ocean, except for anoxic sediments where anaerobic CH_4 oxidation may occur (Scranton & Brewer 1977).

2.2.2 ANAEROBIC OXIDATION OF METHANE (AOM)

Sediments may provide a benthic source of CH_4, where CH_4 is also removed through microbially-mediated anaerobic oxidation of methane (AOM, formerly abbreviated AMO). This process rarely occurs in the water column and only in regions of anoxia. However, AOM can occur within anoxic sediments and microenvironments of anoxia, such as in the guts of zooplankton or other organisms (Schmale et al. 2018; Tilbrook & Karl 1995; Reeburgh 2007). AOM may take place in response to

methanogenesis in anoxic sediments as microbes produce CH_4. Beal et al. (2009) found that manganese (Mn)- and iron (Fe)-dependent AOM can occur. They noted that use of Mn and Fe may be more energetically favorable electron acceptors than AOM through a sulfate-dependent process. Furthermore, studies of sediment porewater have indicated depletions of Mn and Fe in portions of sediment where AOM has occurred (D'Hondt et al. 2004). Methane seeps may also have a coinciding presence of methanotrophs. Following flux of CH_4 to the atmosphere, microbially-mediated oxidation, aerobic or anaerobic, is the next largest sink to oceanic CH_4 (Reeburgh 2007).

2.2.3 FLUX FROM OCEAN TO ATMOSPHERE

If oceanic surface waters are sufficiently supersaturated relative to the atmosphere (e.g., significant benthic sources in shallow waters or high rates of methanogenesis), atmospheric evasion acts as a major sink in the oceanic CH_4 budget (Reeburgh 2007). Atmospheric evasion removes CH_4 from the ocean and transfers it across the air-sea interface to be released into the atmosphere. Portions of the ocean, especially in coastal regions, can act as sources of CH_4 to the atmosphere, thereby removing CH_4 from the oceanic CH_4 budget (Kirschke et al. 2013; Hamdan & Wickland 2016). The degree to which this occurs, in part, depends on gas transfer velocity, OM load, and rates of methanogenesis in surface waters (Weber et al. 2019; Wanninkhof 2014; Reeburgh 2007). Even though the oceanic source to the atmosphere is often weak in surface waters, previous studies suggest the oceans emit roughly 0.5 to 8.2 μmol CH_4 m^{-2} d^{-1} (reported as 6 to 12 Tg-CH_4 yr^{-1}) to the atmosphere due to vast swaths of the ocean acting as a weak source (Reeburgh 2007; Kirschke et al. 2013; Weber et al. 2019). Changes in gas

solubility with warming waters due to climate change may alter evasion flux in the coming decades with the potential for greater evasion rates (Kirschke et al. 2013).

2.3 OCEANIC METHANE MASS BALANCE AND FLUXES

2.3.1 SIMPLIFIED MASS BALANCE FOR THE PACIFIC OCEAN

Setting up a mass balance provides a framework for assessing hypotheses that should be testable with the available data from the GEOTRACES GP15 Pacific Meridional Transect (PMT) cruise. Below, a simplified mass balance equation of anticipated sources and sinks in the Pacific Ocean is presented (Eq. 1; Fig. 2.1). It assumes that the system is at steady state; therefore, the sources equal the sinks. Figure 2.1 provides a graphical representation of Equation 1. Previous studies have described the nature of these processes and their presence in the Pacific (e.g., Karl et al. 2008; Metcalf et al. 2012; Sosa et al. 2019; Weber et al. 2019). The atmospheric invasion and atmospheric evasion terms together can be considered ocean-atmosphere exchange. The biological production term defines any production by biota, including methanogenesis (aerobic or anaerobic) and microbially mediated CH_4 production on fecal pellets and within zooplankton guts. MPn utilization is also microbially mediated; however, due to its expected importance in the subtropical gyres of the Pacific (e.g., Karl et al. 2008), it is considered a separate term of biological production taking place only in the euphotic zone.

(1)

Atmospheric invasion + biological production + MPn utilization + hydrothermal activity + benthic sediment fluxes
=
aerobic or anaerobic methane oxidation + atmospheric evasion

Figure 2.1 *Simplified oceanic methane mass balance of Pacific Ocean*

Schematic of simplified mass balance of source and sink processes occurring in the mixed layer, thermocline, and deep waters of the Pacific. Arrows pointing into the box are sources, and arrows pointing out of the box are sinks. Shapes positioned within the water column or sediments indicate processing within the water column or sediments, respectively. Processes that occur in multiple zones are positioned in the appropriate region, such as aerobic methane oxidation occurring in the mixed layer, thermocline, and deep waters.

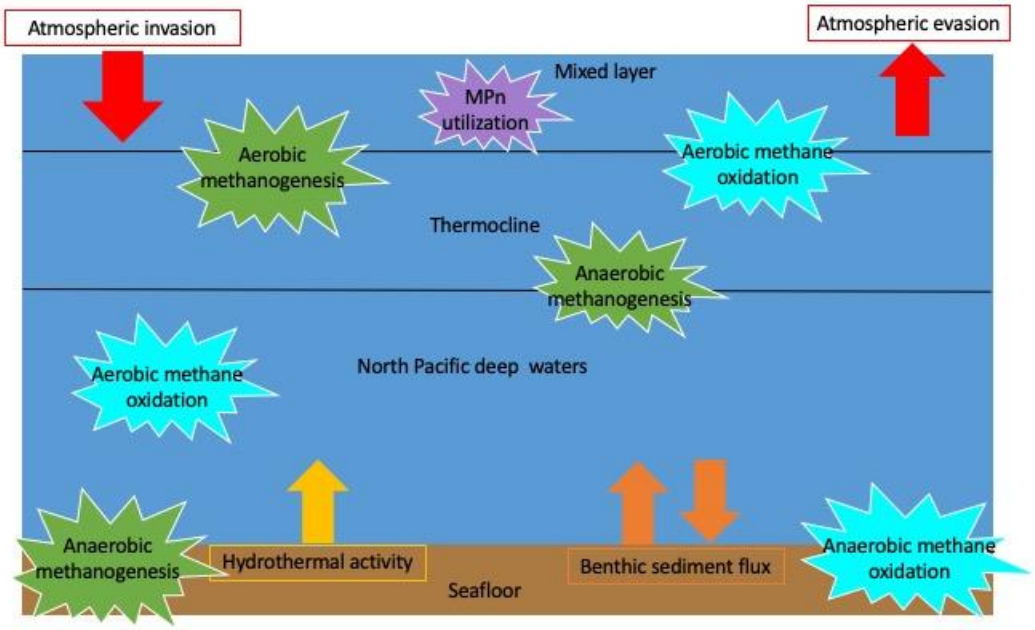

This thesis, however, will not generate a complete mass balance. Instead, using samples from the GP15 cruise will facilitate quantifying ocean-atmosphere exchange fluxes (i.e., atmospheric invasion and evasion). However, a mass balance has been included for illustrative purposes and allows for a conceptual framework for the potential controls on CH_4 distribution. This framework will be critical for assessing parameters

measured on the GP15 cruise and comparing trends in trace metals, nutrients, and plant pigments, among other parameters, with CH_4 distribution to tease apart factors that contribute to ocean-atmosphere exchange. The calculated ocean-atmosphere exchange fluxes, as described in the methods section, will provide insight into the processes that control CH_4 distribution in the open ocean of the Pacific. These fluxes control the contribution of oceanic CH_4 to the atmosphere. Understanding the rates associated with the GP15 transect, particularly at open ocean stations, will provide important information regarding CH_4 distribution in the Pacific.

2.3.2 OCEANIC METHANE AIR-SEA EXCHANGE FLUXES

Sources like methanogenesis and sinks like methanotrophy often occur in close proximity to one another (Chan et al. 2019; Reeburgh 2007). Weber et al. (2019) calculated total oceanic CH_4 emissions between 3 and 6 μmol CH_4 m^{-2} d^{-1} (reported as 6-12 Tg-CH_4 yr^{-1}) with a global diffusive flux from the ocean to the atmosphere of 0.5 to 3 μmol CH_4 m^{-2} d^{-1} (reported as 2-6 Tg-CH_4 yr^{-1}). The difference between total oceanic CH_4 emissions and global diffusive flux is that the total includes diffusive and ebullitive fluxes, which reflects the upper and lower bounds of ebullitive flux uncertainty, whereas global diffusive flux only includes the diffusive term (Weber et al. 2019).

Even though the open ocean has low diffusive fluxes of CH_4, its large expanse generates a source term of 0.3 to 0.7 μmol CH_4 m^{-2} d^{-1} (reported as 0.6-1.4 Tg-CH_4 yr^{-1}), which makes it the second largest emitter of CH_4 to the atmosphere from marine sources, following coastal waters at a rate of 0.4 to 2.0 μmol CH_4 m^{-2} d^{-1} (reported as 0.8-3.8 Tg-CH_4 yr^{-1}; Weber et al. 2019; Cook & Carleton 2000). When extending past the

continental shelf, other sources include outer shelf and continental slope margins, which contribute 0.3 to 0.8 μmol CH_4 m^{-2} d^{-1} with rates between those reported for coastal and open ocean regions (reported as 0.5-1.6 Tg-CH_4 yr^{-1}; Weber et al. 2019). The remaining uncertainty in CH_4 fluxes comes from ebullition fluxes as there are limited studies quantifying these rates (Weber et al. 2019). However, for a given station in the Pacific Ocean transect, the evasion rate is likely at the magnitude of 0 to 1.4 μmol CH_4 m^{-2} d^{-1} (reported as 0-0.5 mmol CH_4 m^{-2} yr^{-1}) based on Weber et al.'s findings (2019), making these stations a minor contribution to the atmospheric CH_4 budget. Much of the Pacific Ocean acts as a weak source of CH_4 to the atmosphere (Karl et al. 2008). Portions of the subtropical Pacific may be P-depleted, resulting in MPn utilization, which produces CH_4 as a by-product (Karl et al. 2008; Repeta et al. 2016). This process could provide a weak source of CH_4 to the atmosphere. Additionally, the deeper the release depth of CH_4, the less likely it is to become a source term to the atmosphere, especially if the release is below 500 m (Weber et al. 2019; Reeburgh 2007). Ebullitive fluxes are a small CH_4 source term in shallow ocean waters (Weber et al. 2019).

The primary research questions this project seeks to address are why the ocean is not a greater source of CH_4 to the atmosphere, what are the major processes that control CH_4 distribution in the Pacific Ocean, how can analysis of trace metals provide greater details regarding CH_4 distribution in the water column, and how may these processes be altered to result in a greater CH_4 source to the atmosphere? Global change may have affected CH_4 concentrations in the past and has the potential to alter CH_4 concentrations in future as a result of anthropogenic global climate change (Reeburgh 2007; Ciais et al. 2013; Kirschke et al. 2013; Ruppel & Kessler 2017). The goal of this project is to

compare the CH_4 distribution with parameters that may provide an indication if the CH_4 distribution is responding to factors that affect the sources and sinks of CH_4.

2.4 HYPOTHESES

The hypotheses for the study are as follows: 1) margin stations have larger net positive ocean-atmosphere fluxes to the atmosphere than open ocean stations, 2) ocean-atmosphere CH_4 fluxes are larger in the North Pacific than in the South Pacific because atmospheric CH_4 concentrations are higher in the Northern Hemisphere than the Southern Hemisphere, 3) wind speed is the primary physical control on ocean-atmosphere exchange fluxes, 4) phosphorus-limited, open ocean stations have elevated mixed layer CH_4 maxima compared to stations with less depleted phosphorus concentrations through MPn utilization, and 5) REE depletions suggest CH_4 oxidation has occurred.

CHAPTER III - METHODOLOGY

3.1 SAMPLE LOCATIONS

Samples were collected on the 2018 GEOTRACES GP15 Pacific Meridional Transect (PMT) cruise stopping at 54 stations from the Aleutian Islands (USA) to Papeete (Tahiti; Table 3.1 and Fig. 3.1). The cruise was conducted from September 18 to November 24, 2018, on the R/V Roger Revelle. The ship left port in Seattle (USA) on September 18 and stopped in Hilo (USA) on October 21-24 and Papeete (Tahiti) on November 24. Dr. Laura Whitmore collected CH_4 samples on the first leg of the cruise, while Dr. Virginie Sanial collected these samples on the second leg. Trace element (TE) samples were collected by Ocean Data Facility (ODF) super technicians. Sampling procedures followed those described in Cutter et al. (2017). Analysis of TE samples after the cruise were performed by Melissa Gilbert. Discrete CH_4 samples were collected from ODF conventional conductivity, temperature, and depth (CTD) rosette casts at 36 stations (Fig. 3.1). Transition metal (TMs) and rare earth elements (REEs) were sampled from GEOTRACES Trace element Carousel (GTC) CTD rosette casts at 36 stations. There were three types of stations where samples were collected from CTD casts: Full, Demi, and Super stations. Full stations sampled from the surface to bottom of the water column with 2 GTC and 3 ODF casts at 24 depths, or 3 GTC and 4 ODF casts at 36 depths (Fig. 3.1, green squares). Demi stations sampled only in the upper 1000 m at 12 depths, using 1 GTC and 1 ODF cast (Fig. 3.1, orange inverted triangles). Super stations involved sampling via 4 GTC and 4 ODF casts at 36 depths (Fig. 3.1, blue diamonds). Underway samples were collected using the ship's flow-through seawater system (sampled from ~3.5 m depth). Near-surface waters were also sampled using a towed fish ("Geo-fish"

from a 40’ aluminum boom extending off the starboard side of the boat, ~3.5 m depth) at intermediate stations between some vertical profiling stations. “Arriving fish” sampling was done within one hour before arriving at vertical profiling stations.

Figure 3.1 *Map of GP15 cruise track*

GP15 cruise track from September 18 to November 24, 2018. Black circles are shelf and slope stations. Green squares are full stations. Orange inverted triangles are demi stations. White triangles are intermediate towed geo-fish stations. Blue diamonds are super stations. Methane samples were collected at all stations.

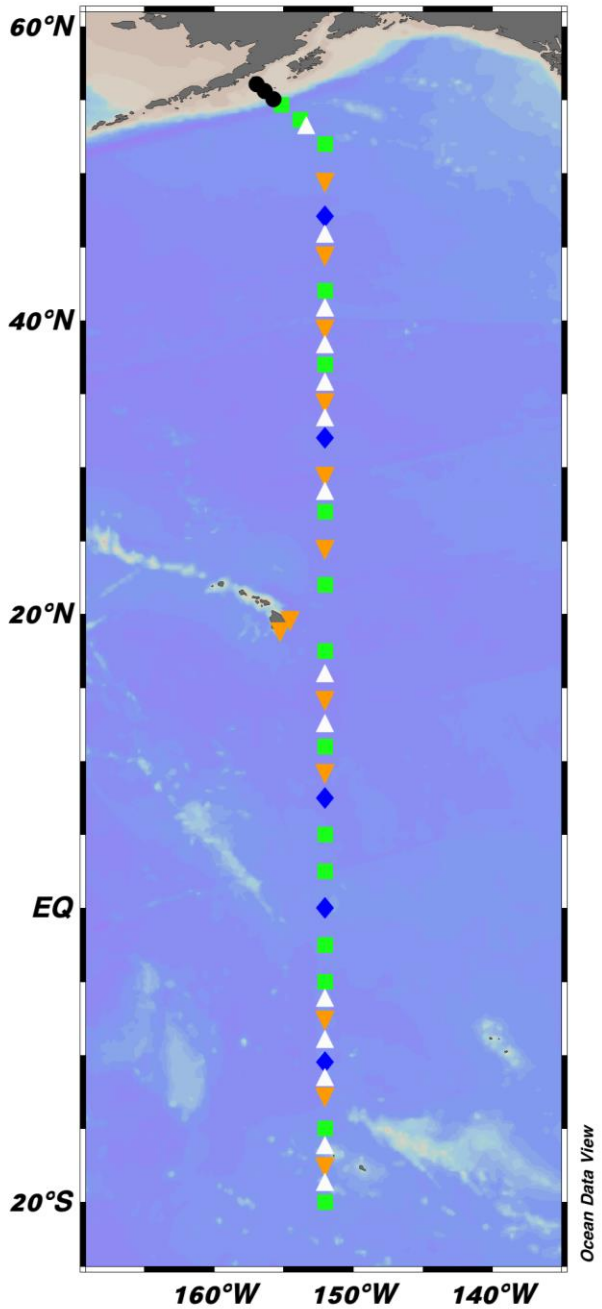

Table 3.1 *GP15 station locations*

Station locations on GP15 cruise. Station 11.5 is marked in red because there was an error in reporting the time of sampling. UTC date and time reflect the time of arrival at a given station.

Station	Latitude (°N)	Longitude (°E)	UTC Date	UTC Time	Station Type
1	56.0585	-156.9628	9/26/18	11:45	Margin
2	55.5958	-156.3469	9/26/18	20:21	Margin
3	55.0803	-155.7202	9/27/18	19:00	Margin
4	54.6602	-155.1707	9/28/18	18:56	Full
5	53.6671	-153.8006	9/24/18	8:56	Full
5.5	53.1551	-153.3521	10/1/18	4:02	Intermediate
6	52.0020	-152.0003	10/1/18	14:35	Full
7	49.5002	-151.9999	10/3/18	15:50	Demi
8	47.0001	-151.9996	10/4/18	11:02	Super
8.5	45.7690	-152.0000	10/6/18	17:44	Intermediate
9	44.5003	-151.9999	10/7/18	1:47	Demi
10	42.0003	-151.9999	10/7/18	22:58	Full
10.5	40.7278	-151.9999	10/9/18	13:21	Intermediate
11	39.5002	-152.0002	10/9/18	20:30	Demi
11.5	38.2812	-152.0000	10/10/18	20:00	Intermediate
12	37.0002	-152.0001	10/10/18	13:17	Full
12.5	35.7500	-152.0000	10/12/18	11:15	Intermediate
13	34.4991	-152.0017	10/12/18	18:22	Full
13.5	33.2501	-152.0000	10/13/18	3:55	Intermediate
14	32.0003	-151.9999	10/13/18	10:54	Super
15	29.4998	-151.9998	10/16/18	0:40	Demi
15.5	28.2500	-152.0000	10/16/18	5:41	Intermediate
16	26.9997	-152.0000	10/16/18	16:02	Full
17	24.4999	-152.0003	10/18/18	14:37	Demi
18	22.0004	-152.0004	10/19/18	7:38	Full
18.3	19.6808	-154.5132	10/21/18	14:16	Demi
18.6	18.9064	-155.2580	10/25/18	14:10	Demi
19	17.5000	-152.0003	10/26/18	19:30	Full
19.5	15.8621	-152.0002	10/28/18	21:33	Intermediate
20	14.2517	-152.0002	10/29/18	6:37	Demi
20.5	12.6250	-152.0000	10/29/18	18:03	Intermediate
21	11.0002	-152.0004	10/30/18	2:55	Full
22	9.2472	-151.9965	11/1/18	1:22	Demi

Table 3.1 (continued)

Station	Latitude (°N)	Longitude (°E)	UTC Date	UTC Time	Station Type
23	7.4995	-152.0082	11/1/18	13:49	Super
25	5.0003	-151.9954	11/4/18	5:23	Full
27	2.4998	-151.9998	11/6/18	9:35	Full
29	0.0023	-151.9987	11/8/18	17:03	Super
31	-2.4998	-151.9992	11/11/18	2:07	Full
33	-5.0004	-152.0006	11/13/18	2:20	Full
33.5	-6.2500	-152.0000	11/14/18	20:15	Intermediate
34	-7.5001	-152.0002	11/15/18	2:51	Demi
34.5	-9.0000	-152.0000	11/15/18	12:48	Intermediate
35	-10.5002	-152.0002	11/15/18	20:19	Super
35.5	-11.6250	-152.0000	11/18/18	0:40	Intermediate
36	-12.7503	-152.0001	11/18/18	6:24	Demi
37	-15.0001	-152.0003	11/18/18	21:20	Full
37.5	-16.2500	-152.0000	11/20/18	15:06	Intermediate
38	-17.4999	-152.0005	11/20/18	23:24	Demi
38.5	-18.7500	-152.0000	11/21/18	8:11	Intermediate
39	-19.9998	-152.0003	11/21/18	16:08	Full

The stations sampled cover four distinct physical regimes: subarctic, temperate, subtropical, and equatorial (Levitus 1982). The Subarctic North Pacific/Alaskan Margin encompasses 55 to 57 °N, Temperate North Pacific includes 30 to 55 °N, Subtropical North Pacific ranges from 10 to 30 °N, and Equatorial North Pacific and South Pacific covers from 10 °N to 20 °S. Due to similarities in chemical distributions between the Equatorial Pacific (10 °N to 10 °S) and South Pacific (10 to 20 °S), a combined Equatorial Pacific and South Pacific regime (10 °N to 20 °S) is discussed in this manuscript. Considering these different regimes can offer insight into the changes in CH_4 distribution along the GP15 transect.

3.2 UNDERWAY METHANE ANALYSIS

3.2.1 SAMPLE COLLECTION AND PROCESSING

Underway CH_4 samples, standards, and blanks were measured with a G2301 cavity ring-down spectroscopy (CRDS) analyzer (Picarro). Breathing air (~2 ppm CH_4) was also measured throughout the cruise; although not a true standard, it will be referred to as standard 1. Two true standards were used: Methane-free zero air (herein, zero air; standard 2), and ~5 ppmv CH_4 (standard 3). Gas standards were measured for three minutes each while on station (i.e., full, demi, and super stations) to check for instrument drift. Nitrogen gas (N_2) served as a procedural blank, and its analysis provided an assessment of drying efficiency (Fig. 3.2). If N_2 water vapor percentage was greater than 3%, analysis of samples and standards was halted to dry silica beads. Standards were connected directly to the back end of the CRDS analyzer and passed through a Nafion dryer to remove excess water vapor before analysis on the front end of the CRDS analyzer (Fig. 3.2).

Bow air samples were also collected. Bow air entered through an inlet at the bow of the ship, which was not near smokestacks or any other portions of the ship that could contaminate the air. Bow air samples reflect the atmospheric concentration of CH_4. The bow air sample line was also connected to the back end of the CRDS analyzer, which routed directly through a condenser to remove excess water vapor (Fig. 3.2). From there, the bow air analytical stream was routed through either only the Nafion dryer or both a silica column and Nafion dryer for removal of condensate before analysis in the front end of the CRDS analyzer (Fig. 3.2). Bow air samples were measured for 10 minutes while

transiting between stations. Bow air was never sampled while stopped at a station because of the increased risk of contamination from the ship while stationary (Johnson 1999). Bow air samples were also processed to act as CH_{4air} measurements, which were used in CH_4 air-sea flux calculations. Bow air samples were typically run after measuring standards.

Figure 3.2 *Diagram of underway CRDS analyzer (Picarro)*

Diagram of CRDS analyzer (Picarro), which was modified from a version made by Eric Chan. Nitrogen gas (N_2) was used as a blank. The standards were as follows: Std.1 breathing air (~2 ppm CH_4), Std.2 zero air (0 ppm CH_4), and Std.3 5 ppm CH_4. Standards and N_2 had direct inlet lines to the back end of the CRDS analyzer. Black boxes indicate valves. Bow air samples went through condensers then a Nafion dryer to remove excess moisture before measurement. A silica column was also used as a desiccant. CRDS represents the front end of the instrument where samples were measured. Green arrows represent the analytical stream, yellow arrows represent the dryer stream, and blue arrows represent the condensate stream.

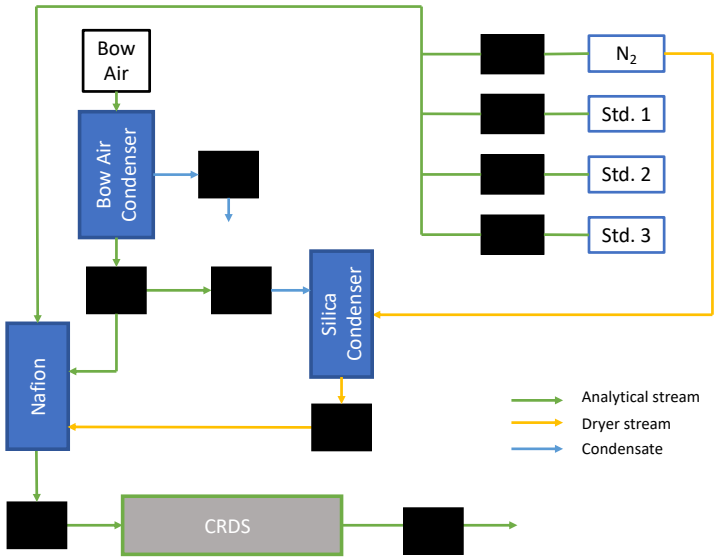

Unfortunately, there were portions of time on the GP15 cruise where the underway CRDS analyzer was not functioning properly and had to be shut off. During

these periods, no bow air data were collected. Data gaps in bow air sampling were addressed by using polynomial fits to existing data to extrapolate the bow air concentrations that might have been measured had the CRDS analyzer been working. Figure A.1 in the appendix illustrates the fit. If there were stations missing bow air data, but adjacent stations had bow air measurements, an average of the bow air CH_4 concentration at the two adjacent stations was used to predict the bow air concentration at the station missing data. For example, bow air CH_4 concentrations at some stations at higher latitudes were determined in this manner.

3.2.2 METHANE CONCENTRATION CALCULATIONS

For the standards, blanks, and bow air samples, the Bunsen solubility coefficient, as parameterized by Wiesenburg and Guinasso (1979), allowed for conversion from partial pressure of CH_4 (pCH_4) measured in ppm to dissolved CH_4 (dCH_4) in nmol kg^{-1} (Eq. 2). The constants used can be found in Table 3.2.

(2)

$$C^* = \exp\left[\ln(pCH_4 \times 10^{-6}) + A_1 + A_2\frac{T}{100} + A_3 \ln\left(\frac{T}{100}\right) + A_4\frac{T}{100} + S \times \left\{B_1 + B_2\frac{T}{100} + B_3\frac{T^2}{100}\right\}\right]$$

$$\text{Where } T = (T_{meas} + 273.15)/100$$

Where pCH_4 (ppm) is the CH_4 concentration measured by the CRDS analyzer, T is absolute temperature (K), T_{meas} is the measured temperature (°C), S is salinity, and C^* is dissolved CH_4 concentration in nmol kg^{-1}.

Table 3.2 *Constants to calculate C* in nmol kg^{-1}*

Constants used to calculate C* by converting pCH_4 (ppm) to equilibrated water CH_4 concentration (nmol kg^{-1}) as described in Wiesenburg and Guinasso (1979).

Constant	nmol kg^{-1}
A1	-417.5053
A2	599.8626
A3	380.3636
A4	-62.0764
B1	-0.064236
B2	0.034980
B3	-0.0052732

3.3 DISCRETE METHANE ANALYSIS

3.3.1 SAMPLE COLLECTION AND PROCESSING

Discrete CH_4 samples were collected at vertical profiling stations from Niskin bottles on the Scripps ODF CTD rosette and from the ship's flow-through sink at intermediate stations and within an hour of arriving at vertical profiling stations. Discrete samples were collected from surface to bottom depth on station and reflect a snapshot of water column conditions at the time of sampling. Samples were collected following methods described by Roberts and Shiller (2015), which are as follows. A 140 mL syringe was rinsed three times with zero air and used to collect 70 mL of water from a silicon tube connected to the Niskin bottles after all bubbles were expelled to ensure an air-free sample. After attaching the tube to the syringe, any bubbles were evacuated via

manipulation of a three-way Luer lock valve after collecting ~30 mL of water for rinsing. The syringe and Luer lock valve were rinsed three times with the sample water.

After sample collection, 70 mL of zero air headspace was added to the syringe. The syringe was placed on a shaker table for approximately 30 minutes to allow the headspace to equilibrate and reach room temperature. However, the temperatures did not need to exactly match because temperature does not strongly affect CH_4 solubility (Wiesenburg & Guinasso 1979). Even so, temperature of each syringe was checked and recorded prior to analysis of the headspace using an infrared thermometer gun. Samples were processed and analyzed within four hours of collection on a CRDS analyzer (Picarro), which was separate from the CRDS analyzer used for underway sampling.

While the sample equilibrated, a procedural blank and standards were measured on the CRDS analyzer. Procedural blank was a transfer of 70 mL of zero air between two syringes, herein referred to as zero air transfer (ZAT). This procedural blank is different from measuring a zero-air standard because it offers an assessment of the error associated with the transfer between syringes. Triplicate measurements of zero air, breathing air, and 5 ppm CH_4 were measured by collecting 70 mL in a 140 mL syringe. After running the standards and procedural blank (ZAT), the equilibrated headspace from the seawater sample syringe was then transferred to an empty, zero air rinsed 140 mL syringe. After connecting the dry syringe to the sample syringe, a small amount of headspace gas was used to rinse the valve pathway between the two syringes. As much headspace as possible without introducing water was transferred to the clean syringe. The valves and syringe interior were checked for water before injecting the sample into the CRDS analyzer as water can damage the instrument.

The sample was measured using the discrete CRDS analyzer via an intake valve on the front end of the instrument by connecting the syringe valve to the intake valve on the CRDS analyzer (Fig. 3.3). The instrument took in the headspace from the syringe, and syringes were removed once all the gas was drawn out. ZAT measurements generated an average blank value 0.00307 ppm (± 0.00063; n = 277) and were measured at each full, demi, super, and intermediate station before measuring discrete samples. Procedural blanks also provided assessment of the uncertainty of CH_4 being introduced to the sample because of the transfer process (~6%; Roberts & Shiller 2015).

Figure 3.3 *Diagram of discrete CRDS analyzer (Picarro)*

Diagram of CRDS analyzer (Picarro) used for measuring discrete samples, standards, and blanks. Samples were added through an inlet on the front end of the CRDS analyzer. Green arrows represent the analytical stream into and out of the instrument.

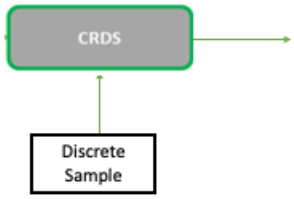

3.3.2 METHANE CONCENTRATION CALCULATIONS

Using the solubility equation from Wiesenburg and Guinasso (1979) allows for determining pCH_4 concentration in equilibrium at temperature T (in Kelvin) and salinity (Eq. 2). Constants for calculating concentrations in nmol kg^{-1} can be found in Table 3.2, and the calculation is described in Equation 2 to convert the headspace pCH_4, which was measured shipboard, to the equilibrated water concentration (C*).

Henry's law (Eq. 3) is used to add up the pCH_4 in the equilibrated headspace, plus C* to determine the original CH_4 concentration in the water.

(3)

$$K_h = \frac{C^* \times 10^{-9}}{pCH_4 \times 10^{-6}}$$

The mass balance equation (Eq. 4) then converts pCH_4 concentration to nmol kg^{-1} for discrete samples. pCH_4 is the concentration of CH_4 (ppm) in equilibrated headspace measured on the Picarro. pCH_4^B is CH_4 concentration measured in the procedural blank. pCH_4^{init} is the initial CH_4 concentration of the equilibration gas or zero air, which is, generally, very close to zero. V_{head} is the volume of the headspace (70 mL). V_{water} is the volume of the water sample (70 mL). R is the gas constant.

(4)

$$CH_4 = [(pCH_4 - pCH_4^B) \times 10^{-6} \times \left(K_h + \frac{(V_{head}/V_{water})}{RT}\right) - \left(pCH_4^{init} \times 10^{-6}\right) \times \frac{V_{head}/V_{water}}{RT}] \times 10^9$$

3.4 U_{10} CALCULATIONS AND WIND SPEED AVERAGING

Wind speed is one of the controlling factors for gas transfer velocity across the air-sea interface. However, wind speed varies at different elevations (z). Wind speed measurements must be standardized to 10 m (z_{10}) above the sea surface (u_{10}). The wind speed power law (Eq. 5; Wanninkhof 2014) allows for calculating u_{10} from the observed wind speed. The wind shear coefficient (α) is an assumed value based on local and atmospheric conditions observed at the sample site. Hsu et al. (1994) determined that

0.11 ± 0.03 provides an appropriate approximation of α for at-sea conditions. Shipboard anemometers mounted at 17 m above sea level (z_{meas}) provided the U_{meas} values of true wind speed.

(5)

$$U_{10} = U_{meas}\left(\frac{z_{10}}{z_{meas}}\right)^{\alpha}$$

After calculating U_{10}, a daily average of wind speed at each station was determined. All U_{10} values within $\pm$ 0.50° latitude on the day of sampling were averaged to determine daily average wind speed. In the case of stations that were sampled over multiple days, a daily average was calculated for each day. Average U_{10} values in Table A.1 correspond to the cast day on which the nearest to the surface discrete CH_4 samples were collected.

3.5 GAS TRANSFER VELOCITY CALCULATIONS

Using U_{10}, the gas transfer velocity (k) can be calculated (Eq. 6). It is frequently calculated as a function of wind speed. Even though complex boundary layer processes control gas transfer velocity, many of them are influenced by wind speed. The introduction of turbulence and shear forcing into the boundary layer from wind influences the transfer of gases with low solubility (Wanninkhof 2014). Changes in turbulence and wind regimes influence gas transfer velocities. Equation 6 is a valid approximation for intermediate wind speeds (3-15 m s^{-1}) (Wanninkhof 2014).

(6)

$$k = 0.251x\ U_{10ave}\ x\ (Sc/660)^{-0.5}$$

U_{10ave} is the average wind speed calculated for true wind speed measurements (Eq. 6). The Schmidt number (Sc) was calculated for each station (Eq. 7) as described by Wanninkhof (2014) using the surface water CTD temperature (°C). The values of the constants for CH_4 are listed in Table 3.3 (Wanninkhof 2014).

(7)

$$Sc = A + BT + CT^2 + DT^3 + ET^4$$

Table 3.3 *Constants to calculate Schmidt number*

Constants used to calculate Schmidt number for CH_4 values as described in Wanninkhof (2014).

Constant	Coefficient
A	2101.2
B	-131.54
C	4.4931
D	-0.08676
E	0.00070663

3.6 FLUX CALCULATIONS

Gas exchange and wind speed can be used to estimate bulk fluxes of CH_4 across the air-sea interface (Wanninkhof 2014). The bulk flux equation uses the gas transfer velocity (k), solubility of CH_4, and partial pressures of CH_4 in water and air (pCH_{4w} and pCH_{4a}, respectively; Eq. 8). C_a and C_w are CH_4 partial pressures converted into nmol kg^{-1} using Equations 2 and 4. Bulk flux will be calculated for each station based on discrete near-surface CH_4 samples.

(8)

$$F = k(C_w - \alpha C_a)$$

where α is the Ostwald coefficient. It is calculated similarly to the Bunsen coefficient. The Bunsen solubility coefficient is calculated as described in Equation 9. When using the Ostwald coefficient, it is calculated using Equation 9, but the sampling temperature is used rather than standard temperature (25 °C), as described in Wiesenburg and Guinasso (1979).

(9)

$$\alpha = [C]/\{p_c/(RT)\}$$

C_a is the concentration of gas (mol m^{-3}) in the air. The Ostwald coefficient is used to convert the air phase into a water phase concentration. The air phase concentration was determined using bow air samples collected shipboard during the GP15 cruise.

3.7 MIXED LAYER DEPTH CALCULATIONS

Mixed layer depth was calculated using the fixed density criterion as described by Monterey and Levitus (1997) and Bishop and Wood (2009; Eq. 10). TEOS-10 equations for σ_t from CTD temperature, salinity, and pressure measurements for each station were used to calculate σ_t and density in the upper 200 m of the water column. The base of the mixed layer was noted by a difference in σ_t of 0.125 kg m^{-3} from surface waters at a given station. This value for σ_t accounts for seasonal mixing (Bishop and Wood 2009).

(10)

$$\Delta\sigma_t = 0.125 \text{ kg/m}^3$$

3.8 TRACE ELEMENT ANALYSIS

3.8.1 SAMPLE COLLECTION

Trace element samples were collected from the GEOTRACES trace-metal clean (GTC) carousel following methods outlined by Cutter and Bruland (2012). Water samples were filtered through pre-cleaned, 0.2 µm filter capsules (Acropak 200 or Supor; Pall Corp.) following methods described by Cutter et al. (2017). Filtered water was stored in 250-mL HDPE bottles (Nalgene). Bottles were precleaned by soaking in hot 1.2 M HCl (reagent grade) for at least eight hours followed by thorough rinsing with ultrapure distilled deionized water (Barnstead E-pure).

3.8.2 SAMPLE PREPARATION

Sorption of trace metals to bottle walls is well-documented (e.g., Massee et al. 1981; Jensen et al. 2020). As a result, samples were acidified to pH < 2 with 6 N ultrapure HCl (Fisher Optima). The acidified samples were left to sit for at least one month prior to analysis to allow metals to solubilize. Sample analysis included transition metals (TMs) and rare earth elements (REEs) plus yttrium (herein, referred to as YREEs).

Dissolved TMs (e.g., Ni, Cu, Cd, Pb, Mn, and Co) and dissolved YREEs were determined by isotope dilution inductively coupled plasma mass spectrometry (ICP-MS) in separate yet similar analytical runs. In both cases, samples were spiked with an isotopically enriched solution. The sample to spike ratio was chosen such that the analytical isotope ratios were approximate to the geometric mean between the natural and enriched spike isotope ratios (e.g., Ho et al. 2018). Pipette calibrations by weight were

performed to ensure accurate volumes of spikes, samples, and dilution water. Sample analyses were performed by Melissa Gilbert (USM).

3.8.3 SAMPLE ANALYSIS

Dissolved TMs were determined using 14 mL of sample, which was spiked with an isotopically enriched solution containing ^{62}Ni, ^{65}Cu, ^{111}Cd, and ^{207}Pb in 1% HNO_3 (Oak Ridge National Labs). Samples were pre-concentrated using a SeaFAST system (Elemental Scientific, Inc.) operated in offline mode, a procedure modified from Lagerstrom et al. (2013) and Ho et al. (2018). A 10-mL sample loop was used, and elution volume was 750 µL. Extracted samples were analyzed using sector field ICP-MS (Thermo Element XR). A PC3 spray chamber (Elemental Scientific, Inc.) was used as the front-end setup for analysis of dissolved TMs. All TMs were determined in medium resolution, except for Cd, which was determined in low resolution. For Mn, the Ni and Cu spikes served as internal standards. A molybdenum standard was measured to check for interference of Mo oxides on Cd isotopes.

Dissolved YREEs were determined using a separate yet similar SeaFAST extraction procedure modified from Hathorne et al. (2012) for extraction in offline mode. The YREE isotopically enriched solution contained ^{142}Ce, ^{145}Nd, ^{149}Sm, ^{153}Eu, ^{155}Gd, ^{161}Dy, ^{167}Er, and ^{171}Yb in 1% HNO_3. An Apex-FAST high efficiency sample introduction system (Elemental Scientific, Inc.) with Spiro desolvator (Elemental Scientific, Inc.) was used as the front-end ICP-MS setup for analysis of YREEs. Dissolved YREEs were determined in low resolution.

Two different types of blanks were measured. The first was a reagent blank, which was eluent taken directly from the eluent bottle. This provided a check as to whether the eluent or the bottle itself could have been a source of contamination to the samples. The second blank was a procedural blank, which was an air blank eluted from the seaFAST in the same manner as a sample, but instead only air was taken into the sample loop. The procedural blank validated any buffer, manifold, column contamination, and carryover between samples. Air blank measurements were analyzed at the beginning and end of each run, providing a comparison of instrument drift and recovery of samples from start to finish. The eluent (10% HNO_3) or reagent blank was measured at the beginning, end, and every 8 samples during the ICP-MS run. The reagent blank was monitored over the course of the run to watch for increasing counts and instrument drift. The Mo standard was measured at the end of each analytical run.

3.8.4 YREEs SHALE-NORMALIZATION AND CALCULATIONS

REE concentrations are often normalized to REE concentrations in source rocks. The normalization provides a potential reference to which REE changes can be compared, such as effects of chemical processes on REE mobilization (e.g., LREE depletion associated with methanotrophy) as well as helping remove Oddo-Harkins effect. Samples were normalized to Post-Archean Australian Shale (PAAS). Values used were described by McLennan and Taylor (1985), Condie (1993), and McLennan (2001). In subsequent equations, subscript sn indicates shale-normalized concentration.

Two types of REE anomalies were calculated: La and Ce. Equations 11 and 12 describe La anomaly calculations (Wang et al. 2020). Equations 13 and 14 describe Ce

anomaly calculations (Wang et al. 2020). A molar ratio of La to Yb was also calculated (Eq. 15). Molar ratio of LREEs to HREEs was calculated as described by Meyer et al. (2021) in Equation 16. LREEs included La, Pr, and Nd; Ce is excluded because of its unique redox chemistry (Meyer et al. 2021; Wang et al. 2020; Wang et al. 2021). HREEs included REEs with an atomic mass greater than 147 (i.e., Sm, Eu, Gd, Tb, Dy, Ho, Er, Tm, Yb and Lu), as described by Meyer et al. (2021).

(11)

$$\text{La anomaly} = \text{La}/\text{La}^*, \text{ where}$$

(12)

$$\text{La}^* = \text{Pr}_{\text{sn}}^3/\text{Nd}_{\text{sn}}^2$$

(13)

$$\text{Ce anomaly} = \text{Ce}/\text{Ce}^*, \text{ where}$$

(14)

$$\text{Ce}^* = \text{Pr}_{\text{sn}}^2/\text{Nd}_{\text{sn}}$$

(15)

$$\text{La/Yb} = \text{La}_{\text{sn}}/\text{Yb}_{\text{sn}}$$

(16)

$$\text{LREE/HREE} = (\text{La}_{\text{sn}} + \text{Pr}_{\text{sn}} + \text{Nd}_{\text{sn}})/$$

$$(\text{Sm}_{\text{sn}} + \text{Eu}_{\text{sn}} + \text{Gd}_{\text{sn}} + \text{Tb}_{\text{sn}} + \text{Dy}_{\text{sn}} + \text{Ho}_{\text{sn}} + \text{Er}_{\text{sn}} + \text{Tm}_{\text{sn}} + \text{Yb}_{\text{sn}} + \text{Lu}_{\text{sn}})$$

Finally, portions of the GP15 trace element dataset can be accessed through the Biological and Chemical Oceanography Data Management Office (BCO-DMO; Shiller 2021a, b).

3.9 ANCILLARY DATA

Pigment data were collected and analyzed at Oregon State University and provided by cruise organizers. Pigment samples were collected from the ODF rosette cast for pigments, Radium, and Thorium isotopes (PigRaTh). Pigments were sampled from the shallowest 6 depths at full and super stations. It is important to note that these samples were collected from different casts than CH_4 and TE samples on Leg 1 of the cruise. During Leg 2, CH_4 samples were also collected from Niskin bottles of the PigRaTh casts. Fluorescence data were collected via fluorometer mounted to the CTD sensor array (Casciotti et al. 2020). Transmissometer data were collected via sensors on the CTD array and analyzed by the Bishop lab group at University of California Berkeley (Casciotti et al. 2020).

Nutrient data were collected and analyzed by ODF cast technicians aboard the R/V Roger Revelle (Casciotti et al. 2021a; Casciotti et al. 2021b). Nutrients measured included nitrate, nitrite, phosphate, and silica following methods described by Becker et al. (2019). Nutrient samples were collected from all stations and intermediate fish casts. Nutrient analyses were performed on a Seal Analytical continuous-flow AutoAnalyzer 3 (AA3), which has detection limit of 0.02 μmol kg^{-1} for nitrate and phosphate. For assessing nutrient limitations, the following calculations were performed. Apparent oxygen utilization (AOU) was calculated as described by Redfield (1934). Calculations regarding PO_4 and NO_3 used updated Redfield ratios as described in Broecker et al. (1998) and Anderson and Sarmiento (1994), for example. Phosphate star (herein, P*) was calculated as described in Deutsch et al. (2007). Nitrate star (herein, N*) was calculated as described by Gruber and Sarmiento (1997).

Methane air-sea fluxes and other data from previous studies were found via literature review and use of the MarinE MethanE and NiTrous Oxide (MEMENTO) database (Bange et al. 2009).

3.10 DATA ANALYSIS PROGRAMS

Analysis of hydrographic, underway CH_4, discrete CH_4, and trace element data were performed in RStudio (R Core Team, 2021). RStudio package TheSource created by Kelly (2019) was used for coding of TEOS-10 equations of state, AOU, and nutrient analyses (e.g., N* and P*). Figures were prepared in RStudio (R Core Team 2021) and Ocean Data View (Schlitzer 2021). Statistical analyses (i.e., paired student's t test) were performed in RStudio. Paired t tests were used to compare CH_4 fluxes between various physical regimes sampled on the GP15 cruise. These included the North and South Pacific as well as different gyre regimes separated into categories of Subarctic North Pacific/Alaskan Margin, Temperate North Pacific, Subtropical North Pacific, and Equatorial North and South Pacific.

3.11 ERROR ANALYSIS

Error analysis and quantification of propagation of errors will provide assessment for the degree of uncertainty regarding the flux calculations. Wanninkhof (2014) reports 20% relative standard deviation (RSD) for the gas transfer velocity (Eq. 6). This uncertainty relates to the parameterization of k. Wind speed and k have a non-linear relationship, meaning 20% RSD results from the quadratic fit used by Wanninkhof (2014). Roberts and Shiller (2015) estimated a 6% RSD for determination of dissolved

CH_4 concentrations at typical oceanic concentrations. The atmospheric CH_4 or bow air concentrations have an associated 4.7% RSD, as described in Johnson (1999). For a conservative error estimate, values of 20%, 10%, and 5% were used for k, dissolved CH_4, and atmospheric CH_4, respectively.

A propagation of errors formula translates the variance in individual results into the estimate of error in the result. This formula is quite useful for simple equations, but only works if the error associated with a given variable is not correlated with the error associated with another variable in the equation. A generalized formula for a function x = f(u, v, …) is as follows with σ^2 representing the sample variance (Glover et al. 2011):

(17)

$$\sigma_x^2 = \sigma_u^2 \left(\frac{\partial x}{\partial u}\right)^2 + \sigma_v^2 \left(\frac{\partial x}{\partial v}\right)^2 + \cdots$$

Equation 18 outlines how this method has been used to calculate the variance associated with the flux calculations based on Equation 9 or Flux = $k(C_w - \alpha C_a)$ and simplified using the approach outlined in Equation 17. This value is merely an estimate of the relative uncertainty of the flux equations and may be a conservative estimate.

(18)

$$\sigma_{Flux}^2 = (C_w - \alpha C_a)^2 \sigma_k^2 + k^2 (\sigma_{C_w}^2 + \alpha^2 \sigma_{C_a}^2)$$

Previous studies have used a propagation of errors approach (Weber et al. 2019; Bates et al. 1996), which has sometimes been combined with Monte Carlo analysis (Weber et al. 2019), to determine the uncertainty of flux calculations. Weber et al. (2019)

reported that uncertainty in the difference between C_w and C_a was greater than uncertainty in k. When comparing the effects of each component on the overall flux uncertainty, Weber et al. (2019) found that C_w dominated. Differences in C_a RSD had a negligible effect on CH_4 flux RSD compared to k and C_w. Although C_w and k certainly contribute the most to flux uncertainty, small differences in C_w changed the flux RSD more than small differences in k.

CHAPTER IV – ANALYSIS OF DATA

4.1 METHANE DISTRIBUTION

Results of the discrete sample processing indicate that seawater CH_4 concentrations were highest at stations along the continental margin and in the upper 200-500 m throughout the transect (Fig. 4.1). Previous studies have noted water column CH_4 maxima above the pycnocline (~50-150 m) (Bates et al. 1996; Scranton & Brewer 1977; Burke Jr. et al. 1983; Yoshikawa et al. 2014). CH_4 concentrations decreased rapidly within the thermocline and were typically less than 2 nmol kg^{-1} in deeper waters (i.e., depth > 1000 m; Fig. 4.1 and 4.2). These findings align with previously described research (e.g., Bates et al. 1996; Karl et al. 2008; Reeburgh 2007). Methane concentrations were often highest in the upper 100-200 m of the water column (Fig. 4.1 and 4.2). Methane saturation (%) followed the same trends as CH_4 concentrations in the upper 500 m of the water column (Fig. 4.3). Atmospheric equilibrium CH_4 concentration was approximately 2.3 nmol kg^{-1}. Apart from waters from ~5 °S to 15 °S, all near-surface waters (< 100 m) were supersaturated with CH_4 relative to the atmosphere (Fig. 4.3). Along the continental margin, supersaturations greater than 200% were common (Fig. 4.3). Mixed layer and coastal CH_4 supersaturations have been previously reported in other studies (e.g., Reeburgh 2007; Weber et al. 2019).

Figure 4.1 *Methane concentration in upper 500 m of water column*

Methane concentration (nmol kg^{-1}) in upper 500 m for GP15 transect. Color bar is scaled such that values less than 2 nmol kg^{-1} are purple and values greater than 4 nmol kg^{-1} are peach.

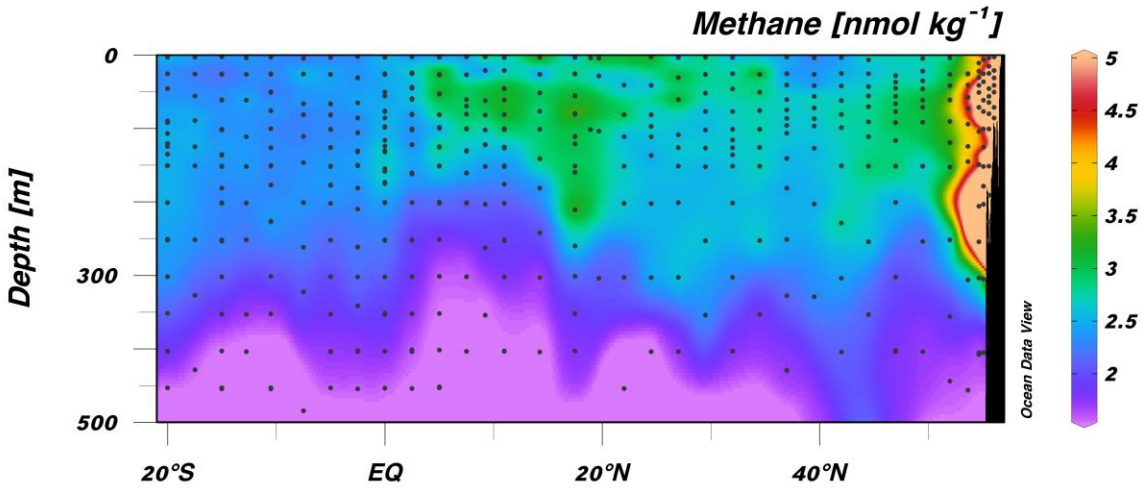

Figure 4.2 *Methane concentration with depth (m)*

Measured methane concentration (nmol kg^{-1}) with depth (m) for all stations.

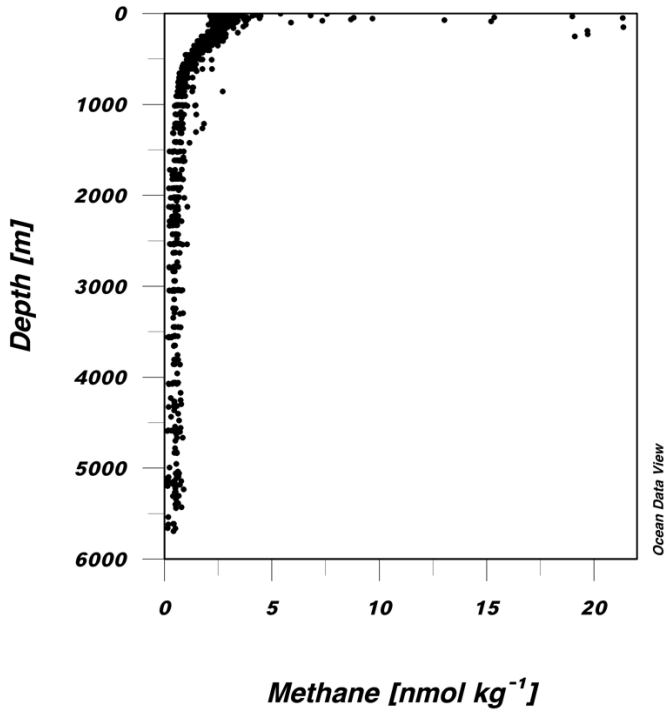

Figure 4.3 *Methane saturation (%) in upper 500 m*

Methane saturation (%) in upper 500 m for GP15 transect. Red contour indicates 100% saturation relative to the atmosphere (atmospheric equilibrium value equivalent to approximately 2.3 nmol kg^{-1} CH_4). Red to yellow shading indicates supersaturated waters relative to atmosphere, and blue shading indicates undersaturated waters relative to atmosphere.

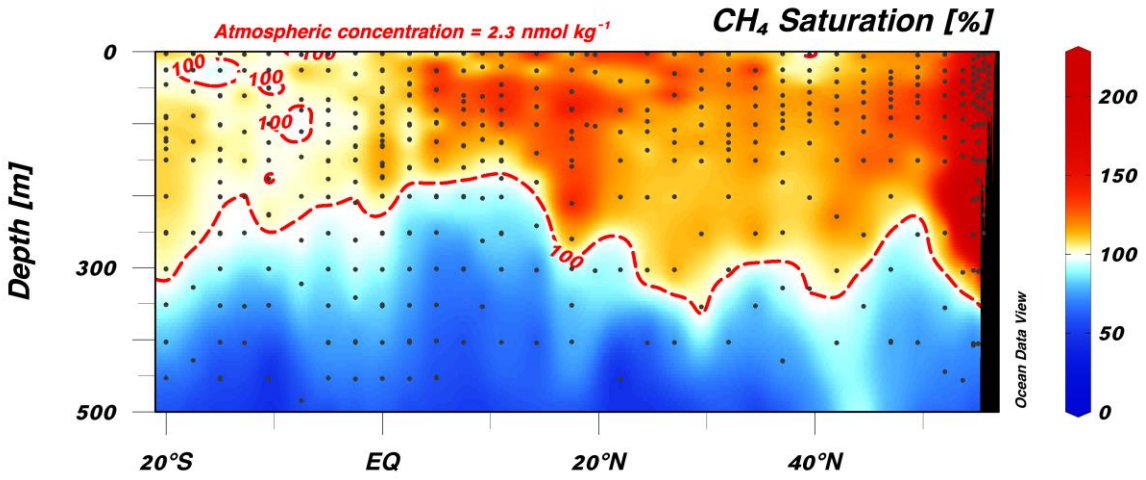

Occasionally, relatively higher CH_4 concentrations were observed in intermediate waters (e.g., > 1.5 nmol kg^{-1}). For example, stations 18.3 and 18.6 off the Hawaiian margin near 20 °N exhibited higher CH_4 and Mn concentrations than other open ocean stations but lower concentrations than were observed along the continental margin (Fig. 4.4 and 4.5, respectively). Hydrothermal activity at the nearby Loihi Seamount and Puna Ridge (Fig. 4.6) may act as a source of some trace metals (Jenkins et al. 2020). This activity may have contributed to higher CH_4 concentrations in intermediate waters at stations 18.3 and 18.6 than were observed at other open ocean stations (Fig. A.2). Additionally, because CH_4 oxidation is the primary sink of CH_4 in deeper waters, these elevated CH_4 concentrations suggest that there must be an additional source term, such as hydrothermal activity (Reeburgh 2007).

Figure 4.4 *Methane concentration at stations 18.3 and 18.6*

Methane (CH_4) concentration (nmol kg^{-1}) at GP15 stations 18.3 and 18.6 near Hawaii. Green circles indicate measurements from station 18.3, and blue squares indicate measurements from station 18.6.

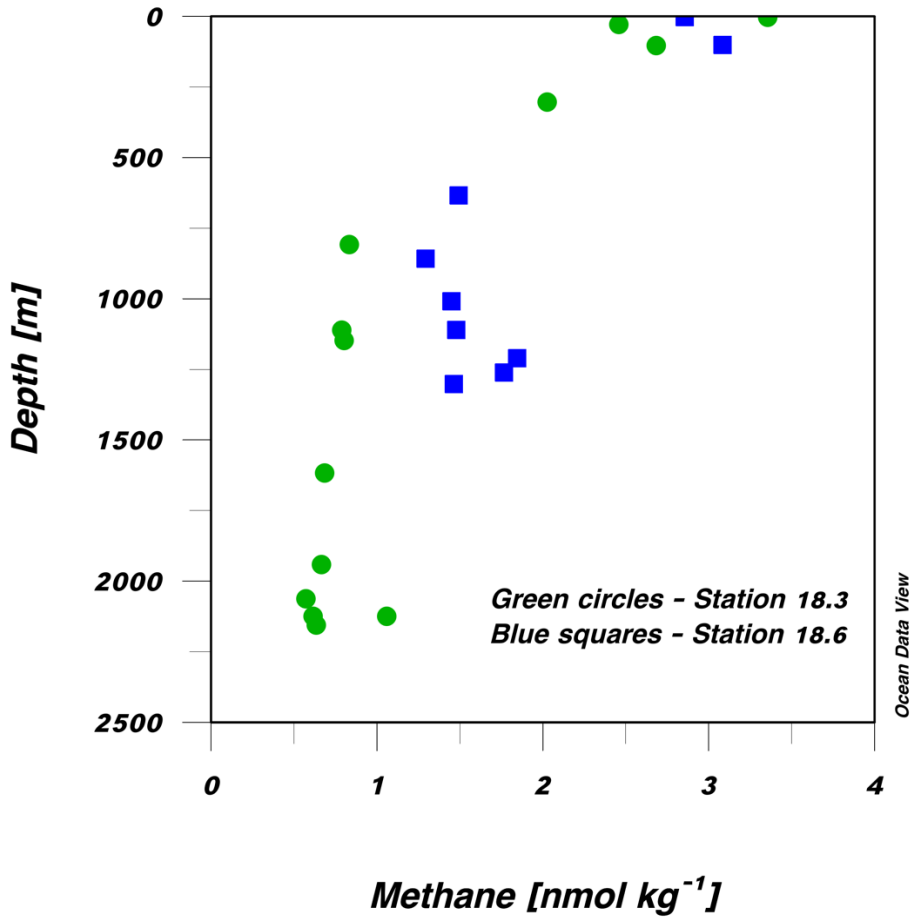

Figure 4.5 *Manganese concentration at stations 18.3 and 18.6*

Manganese (Mn) concentration (nmol kg^{-1}) at GP15 stations 18.3 and 18.6 near Hawaii. Green circles indicate measurements from station 18.3, and blue squares indicate measurements from station 18.6.

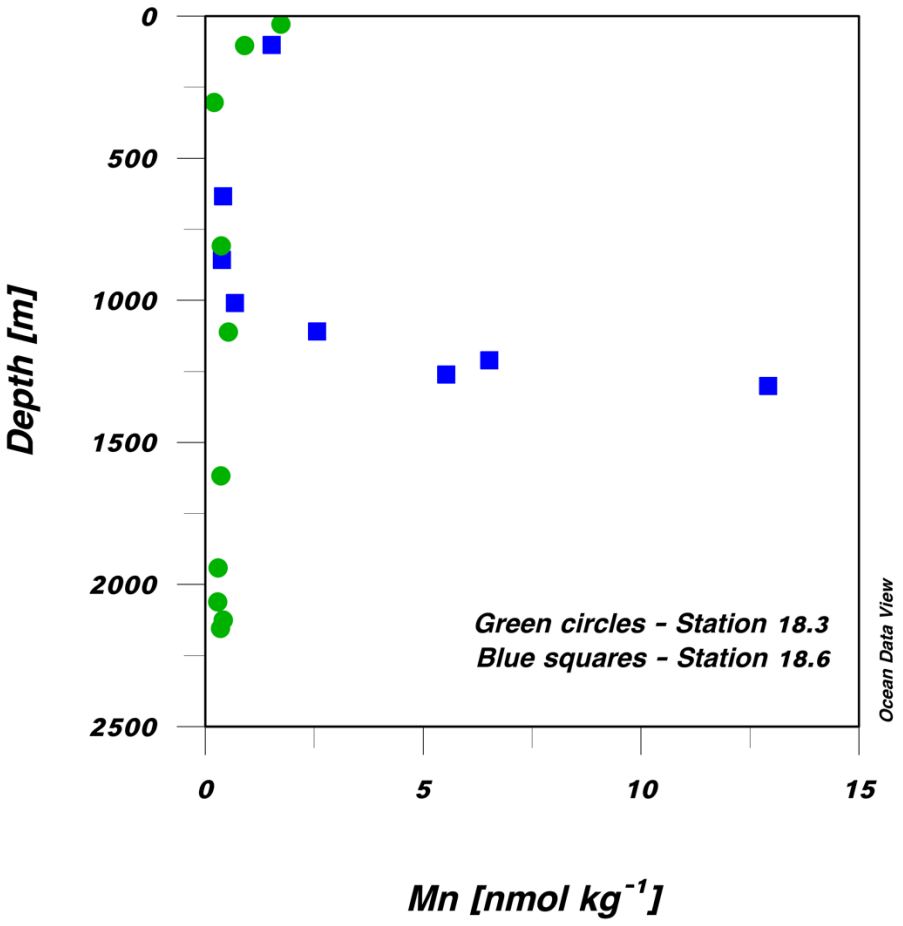

Figure 4.6 *Map of Hawaii marking Loihi Seamount and Puna Ridge*

Map of Hawaii indicating Loihi Seamount and Puna Ridge (yellow pins). Base map generated in Google Earth.

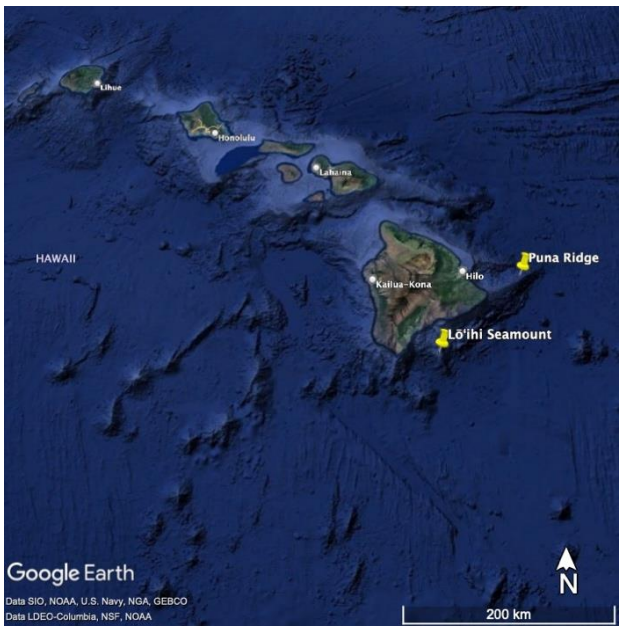

4.2 METHANE AIR-SEA EXCHANGE FLUXES

Air-sea CH_4 fluxes throughout the GP15 transect illustrate potential influences of changes in physical and biogeochemical regimes latitudinally and temporally. CH_4 fluxes ranged from -0.88 to 4.9 µmol CH_4 m^{-2} d^{-1} (Fig. 4.7; Table A.1). Based on the uncertainty calculated using a propagation of errors approach, flux values within ± 1σ µmol CH_4 m^{-2} d^{-1} of zero are not significantly different from zero. Most stations had a near-surface seawater CH_4 measurement collected within 10 m of the surface (Table A.1). All stations had their shallowest sample collected within the mixed layer (Table A.1). The average flux for the transect was 0.96 ± 1.0 µmol CH_4 m^{-2} d^{-1}.

Figure 4.7 *Methane air-sea exchange fluxes for all GP15 stations*

Methane air-sea exchange fluxes (μmol CH_4 m^{-2} d^{-1}) with latitude (°N) for the GP15 transect. Open circles indicate bow air CH_4 concentration was extrapolated, and black circles indicate bow air CH_4 was measured. Error bars reflect the error of determination, which were calculated by propagation of errors. Dashed lines at 10 °N, 30 °N, and 55 °N represent changes in regime from Equatorial North and South Pacific to Subtropical North Pacific to Temperate North Pacific and to Alaskan Margin, respectively.

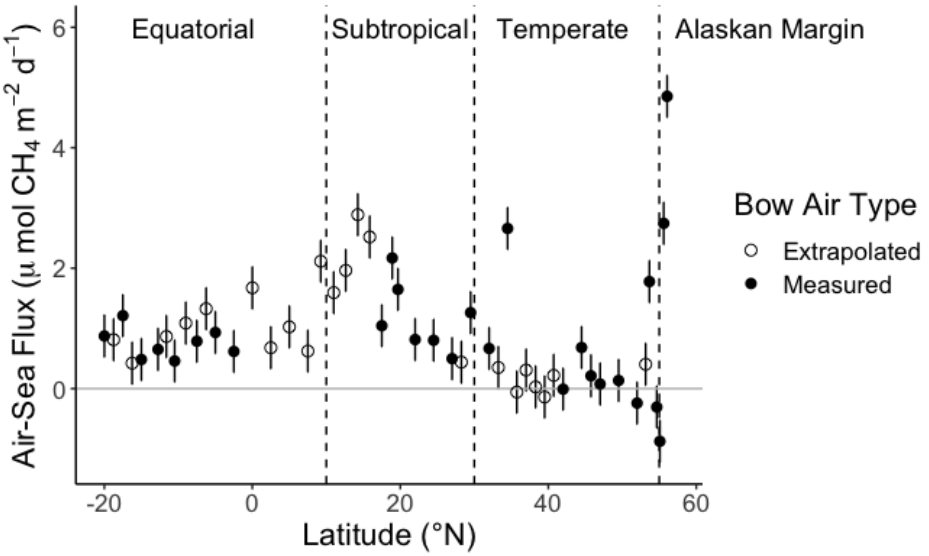

Bow air CH_4 concentrations declined with decreasing latitude (Fig. 4.8). Near-surface seawater CH_4 concentrations were more variable throughout the transect with no clear trends beyond near-surface CH_4 concentrations being highest near the continental margin (Fig. 4.9). When excluding the margin stations, it is apparent that near-surface CH_4 concentrations were often lower in the Temperate North Pacific and Equatorial North and South Pacific than in the Subtropical North Pacific (Fig. 4.9). However, when only the two hemispheres were considered, there were no significant differences between CH_4 fluxes in the North and South Pacific ($p > 0.05$; Table A.2). There were significant differences between bow air CH_4 and discrete near-surface CH_4 concentrations between

the two hemispheres ($p < 0.01$; Table A.2). Bow air CH_4 concentration differences between the two hemispheres align with previously reported latitudinal differences in CH_4 (e.g., Forster et al. 2009; Reeburgh 2007). As previously mentioned, there were no significant differences in CH_4 flux between the two hemispheres regardless of significant differences in near-surface seawater CH_4 and bow air CH_4.

Figure 4.8 *Bow air methane concentration with latitude*

Bow air methane concentration (nmol kg^{-1}) measured by CRDS analyzer as they changed with latitude (°N) throughout the GP15 cruise. Bow air CH_4 values were extrapolated where the instrument failed to measure CH_4 concentration. Open circles indicate extrapolated data, and black circles indicate measured data.

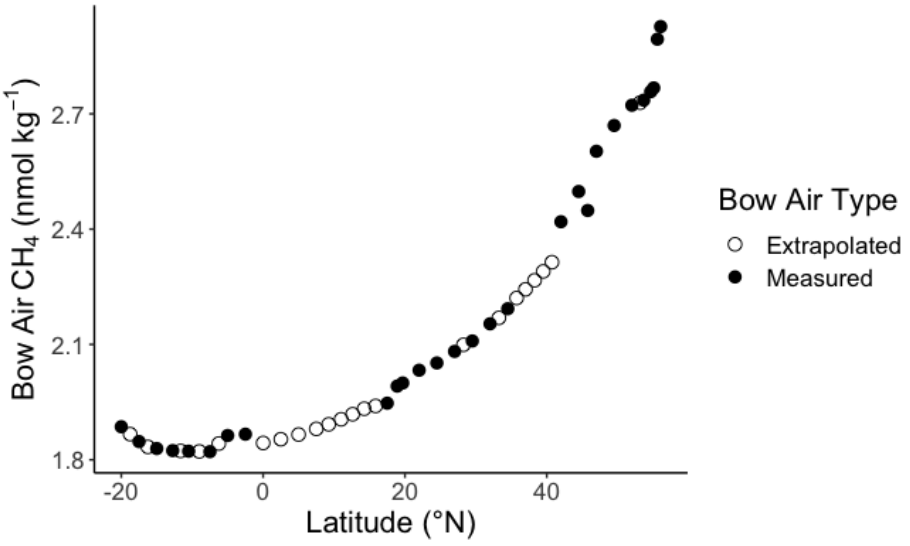

Figure 4.9 *Near-surface seawater methane concentration with latitude*

Near-surface seawater methane concentration (nmol kg^{-1}) measured by discrete sampling with latitude (°N). All samples were collected from the shallowest CTD cast or ship's flow-through sink.

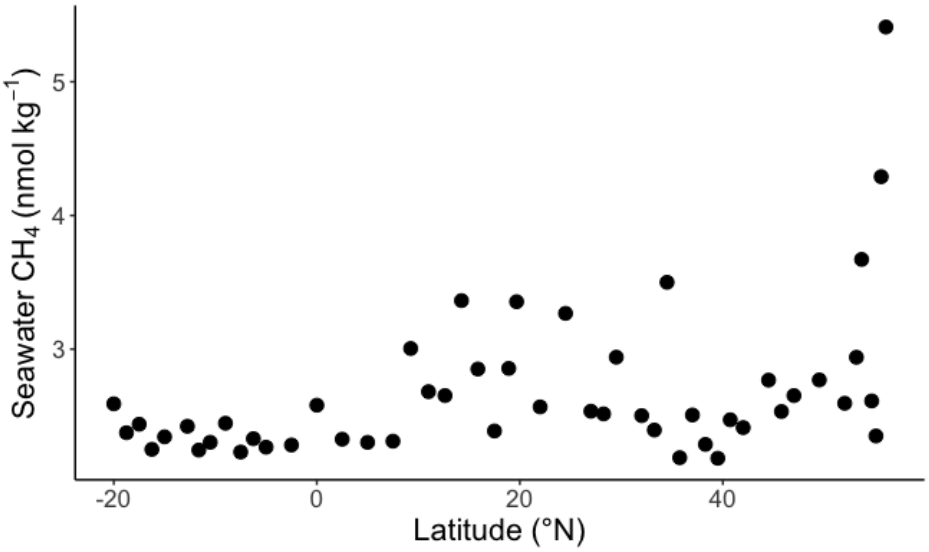

It is well-documented in existing literature that air-sea CH_4 fluxes are highest in estuaries and along the continental margin (e.g., Weber et al. 2019; Borges et al. 2016). Coastal waters contribute to the atmospheric CH_4 budget at a rate of 0.4-1.9 µmol CH_4 m^{-2} d^{-1} (reported as 0.8-3.8 Tg-CH_4 yr^{-1}; Weber et al. 2019; Cook & Carleton 2000). CH_4 fluxes measured at the margin stations along the GP15 transect range from -0.88 to 4.9 µmol CH_4 m^{-2} d^{-1} (Table A.1; stations 1-3). Furthermore, research in the Subtropical South Pacific along 17 °S from the coast of Peru to coast of Australia noted air-sea CH_4 fluxes ranging from -0.20 to 4.8 µmol CH_4 m^{-2} d^{-1}, with the highest fluxes near the coast (Yoshikawa et al. 2014). Comparison with this study suggests good agreement with higher CH_4 flux values measured in the Pacific during the GP15 cruise. Additionally, CH_4 fluxes reported for GP15 are similar in magnitude to flux values reported in previous studies (e.g., Cook & Carleton 2000; Weber et al. 2019).

When excluding the margin stations, trends within the open ocean can be better elucidated. CH_4 fluxes range from -0.31 to 2.9 μmol CH_4 m^{-2} d^{-1} (Fig 4.10; Table A.1). The highest air-sea CH_4 fluxes in the open ocean were observed around 20, 40, and 52 °N (Fig. 4.10). It can be noted that, except for a few stations, CH_4 fluxes were lower in the Temperate North Pacific, increased in the Subtropical North Pacific, and decreased moving towards the equator, and then remained at similar values in the South Pacific compared to the Equatorial Pacific (Fig. 4.10). Throughout much of the transect, stations with higher air-sea CH_4 fluxes appear to coincide with higher discrete near-surface CH_4 concentrations (Table A.2). However, as can be observed near 20 °N, this correlation is not consistent, suggesting that near-surface seawater CH_4 concentration was not a definitive indicator of CH_4 flux (Fig. 4.9). As was discussed previously regarding bow air extrapolated data, the uncertainty in the bow air CH_4 concentration has a minor effect on overall uncertainty of the flux calculations. Variability in CH_4 flux can be high even between adjacent stations where bow air was measured. This further supports the assessment that, although uncertainty in extrapolated bow air CH_4 concentrations contributes to overall uncertainty in the flux calculations, it is minor compared to other equation factors, such as near-surface seawater CH_4 and k.

Figure 4.10 *Methane air-sea exchange fluxes for GP15 open ocean stations*

Methane air-sea fluxes (µmol CH_4 m^{-2} d^{-1}) with latitude (°N) for the open ocean stations on GP15 transect. Open circles indicate bow air CH_4 concentration was extrapolated, and black circles indicate bow air CH_4 was measured. Error bars reflect the error of determination, which were calculated by propagation of errors. Dashed lines at 10 °N and 30 °N represent changes in regime from Equatorial North and South Pacific to Subtropical North Pacific to Temperate North Pacific, respectively.

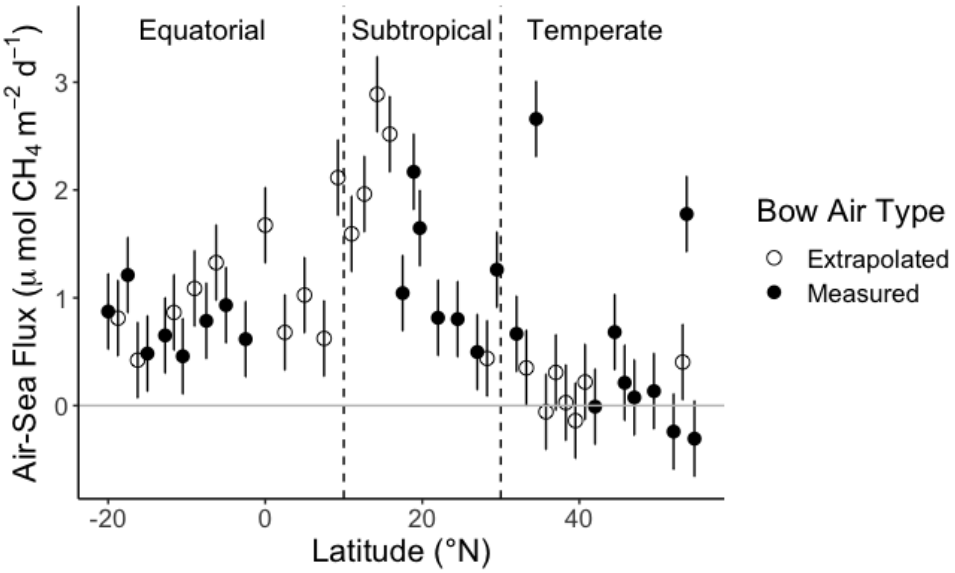

As with the margin stations, the observed CH_4 fluxes align well with previously reported values in the Pacific Ocean. For the Pacific Ocean basin, Weber et al. (2019) estimate air-sea CH_4 fluxes of 0.33 to 0.94 µmol CH_4 m^{-2} d^{-1} (reported as 0.65 to 1.84 Tg-CH_4 yr^{-1}). For all global oceans, they estimated fluxes of 2.0 ± 0.92 µmol CH_4 m^{-2} d^{-1} (reported as 3.9 ± 1.8 Tg-CH_4 yr^{-1}). The majority of the CH_4 air-sea fluxes measured along the GP15 transect fall within Weber et al.'s range for the Pacific Ocean. The highest measured fluxes for GP15 were higher than the range they reported for the Pacific Ocean. However, the higher fluxes fell within the range described for the global open ocean. It is important to note that Weber et al.'s (2019) values were modeled based on existing datasets, and there were notable gaps in data availability for the open ocean.

Reported open ocean fluxes for similar open ocean physical regimes yield flux values of 0.1 to 2 μmol CH_4 m^{-2} d^{-1} (reported as 0.2 to 3 Tg-CH_4 yr^{-1}; Conrad & Seiler 1988; Bates et al. 1996; Rhee et al. 2009). The study performed by Bates et al. (1996) is of particular interest because they assessed similar regions in the Pacific Ocean. Bates et al. (1996) found average zonal fluxes from 75 °N to 75 °S ranged from -0.1 to 0.4 μmol CH_4 m^{-2} d^{-1}. The combined seasonal and zonal fluxes yield a total ocean-to-atmosphere flux of 0.20 μmol CH_4 m^{-2} d^{-1} (reported as 25 Gmol CH_4 yr^{-1}; Bates et al. 1996). Another study in the Subtropical North Pacific observed CH_4 flux rates of 1.6 ± 0.1 μmol CH_4 m^{-2} d^{-1} (Holmes et al. 2000). Our values align well with theirs (-0.31 to 2.9 μmol CH_4 m^{-2} d^{-1}), suggesting good agreement with previously reported studies (e.g., Weber et al. 2019; Bates et al. 1996; Holmes et al. 2000; Rhee et al. 2009). Since the publication of older studies (e.g., Bates et al. 1996; Holmes et al. 2000), equations to constrain CH_4 flux and gas transfer velocity have improved (e.g., Wanninkhof 2014). As a result, GP15 CH_4 data build upon the existing scientific literature with improved calculations of CH_4 fluxes in historically under sampled regions and increase the robustness of seasonal CH_4 distribution for fall and early winter.

Finally, with the distribution of CH_4 fluxes across multiple physical regimes, it is worth noting whether any regions yielded significantly different flux values from others. Because the Alaskan Margin stations exhibited both the largest and smallest CH_4 fluxes on the transect, the average fluxes measured at these stations were not significantly different from any other region on the transect (Table 4.1). The average flux was 2.2 ± 2.9 μmol CH_4 m^{-2} d^{-1} (Table 4.1). In the Temperate North Pacific, average CH_4 flux was 0.40 ± 0.76 μmol CH_4 m^{-2} d^{-1} (Table 4.1). The CH_4 fluxes measured in this region were

significantly different from the Subtropical North Pacific and Equatorial North and South Pacific (Table 4.1). In the Subtropical North Pacific, the average CH_4 measured was 1.5 ± 0.8 µmol CH_4 m^{-2} d^{-1} (Table 4.1). This region was only significantly different from the Temperate North Pacific (Table 4.1). In the Equatorial North and South Pacific, the average CH_4 flux was 0.92 ± 0.44 µmol CH_4 m^{-2} d^{-1} (Table 4.1). Like the Subtropical Pacific, it significantly differed from only the Temperate North Pacific (Table 4.1). Together, these data suggest that there were significantly different rates of air-sea exchange that influenced the CH_4 fluxes in these different regions, resulting in significant differences between some regions.

Table 4.1 *Average methane air-sea exchange fluxes by region*

Average methane fluxes (µmol CH_4 m^{-2} d^{-1}) ± standard deviation for each region of the GP15 transect. Student's t tests were used to determine p values. Significant differences are indicated if $p < 0.05$. Minimum and maximum CH_4 flux values illustrate the range measured in each region.

Region	**GP15 Stations**	**Average CH_4 Flux (µmol CH_4 m^{-2} d^{-1})**	**Significantly Different from Another Region?**	**Min. CH_4 Flux (µmol CH_4 m^{-2} d^{-1})**	**Max. CH_4 Flux (µmol CH_4 m^{-2} d^{-1})**
Alaskan Margin	1-3	2.2 ± 2.9	No	-0.88	4.9
Temperate N. Pacific	4-14	0.40 ± 0.76	Yes, Subtropical ($p < 0.01$) and Equatorial ($p < 0.05$)	-0.31	2.7
Subtropical N. Pacific	15-21	1.5 ± 0.80	Yes, Temperate ($p < 0.01$)	0.44	2.9
Equatorial N. and S. Pacific	22-39	0.92 ± 0.44	Yes, Temperate ($p < 0.05$)	0.42	2.1

4.3 PHYSICAL REGIMES

The primary physical parameters that influence air-sea CH_4 flux, besides CH_4 concentrations, are wind speed and gas transfer velocity (Wanninkhof 2014). Much of the flux uncertainty comes from the calculation of gas transfer velocity (k), which has a non-linear relationship with wind speed. Using a quadratic fit, k generally increases with increasing wind speed (Wanninkhof 2014). As illustrated with Figure 4.9, differences in near-surface seawater CH_4 concentrations alone do not account for the differences in CH_4 flux between stations. When considering U_{10} wind speed, many stations with elevated CH_4 flux (i.e., > 1 μmol CH_4 m^{-2} d^{-1}), also exhibit moderate to high wind speeds (Fig. 4.11). However, this is not a consistent correlation, one example being the stations around 43 °N with observed wind speeds of 10 m s^{-1} or greater but CH_4 fluxes near zero (Fig. 4.11). Furthermore, when comparing gas transfer velocity and CH_4 flux values for all stations, there are no obvious trends (Fig. 4.12). No significant differences were observed in gas transfer velocities between the two hemispheres ($p > 0.05$; Table A.2). However, U_{10} wind speeds were significantly different between the two hemispheres ($p < 0.05$; Table A.2). Although wind speed is the primary physical factor influencing gas transfer velocity, it does not offer a clear-cut explanation as to why some stations have more elevated CH_4 fluxes than others with little correlation between U_{10} wind speed and CH_4 flux (Fig. 4.13).

Figure 4.11 *Methane air-sea exchange fluxes for all stations with U_{10} color bar*

Methane air-sea fluxes (µmol CH_4 m^{-2} d^{-1}) with latitude (°N) for all stations on GP15 transect. Circles indicate bow air CH_4 concentration was extrapolated, and triangles indicate bow air CH_4 was measured. Error bars reflect the error of determination, which were calculated by propagation of errors. Colors indicate U_{10} wind speeds (m s^{-1}). Dashed lines at 10 °N, 30 °N, and 55 °N represent changes in regime from Equatorial North and South Pacific to Subtropical North Pacific to Temperate North Pacific and to Alaskan Margin, respectively.

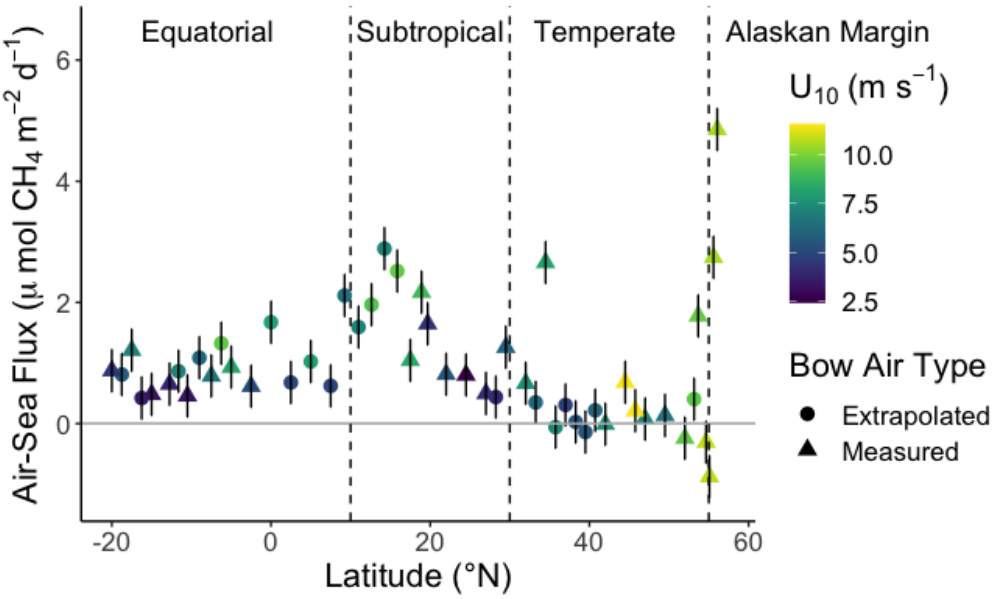

Figure 4.12 *Methane air-sea exchange fluxes for all stations with gas transfer velocity color bar*

Methane air-sea fluxes (µmol CH_4 m^{-2} d^{-1}) with latitude (°N) for all stations on GP15 transect. Circles indicate bow air CH_4 concentration was extrapolated, and triangles indicate bow air CH_4 was measured. Error bars reflect the error of determination, which were calculated by propagation of errors. Colors indicate gas transfer velocity (k; m d^{-1}). Dashed lines at 10 °N, 30 °N, and 55 °N represent changes in regime from Equatorial North and South Pacific to Subtropical North Pacific to Temperate North Pacific and to Alaskan Margin, respectively.

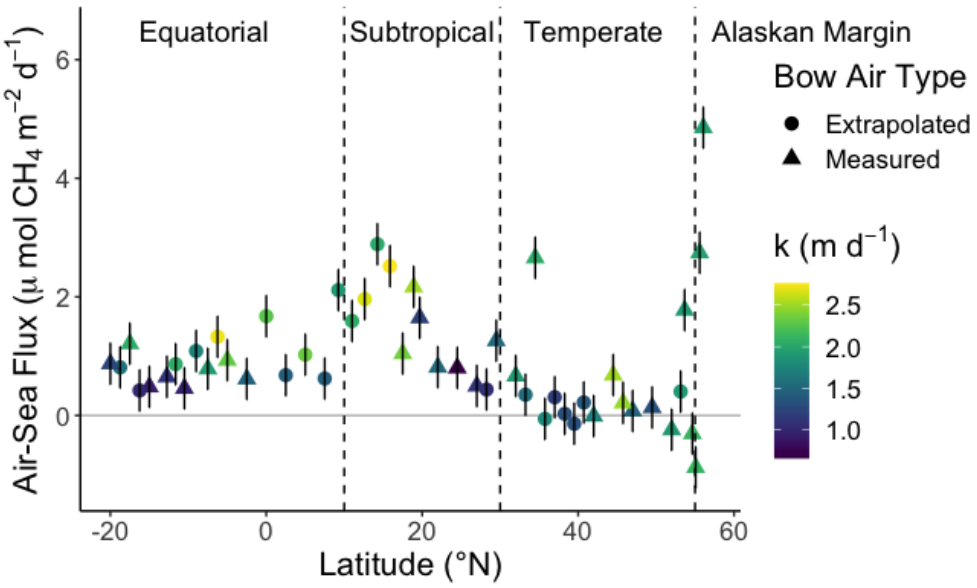

Figure 4.13 *U_{10} wind speeds versus methane air-sea exchange fluxes*

U_{10} wind speeds (m s^{-1}) versus methane air-sea fluxes (µmol CH_4 m^{-2} d^{-1}) for all stations. Open circles indicate bow air CH_4 concentration was extrapolated, and black circles indicate bow air CH_4 concentration was measured.

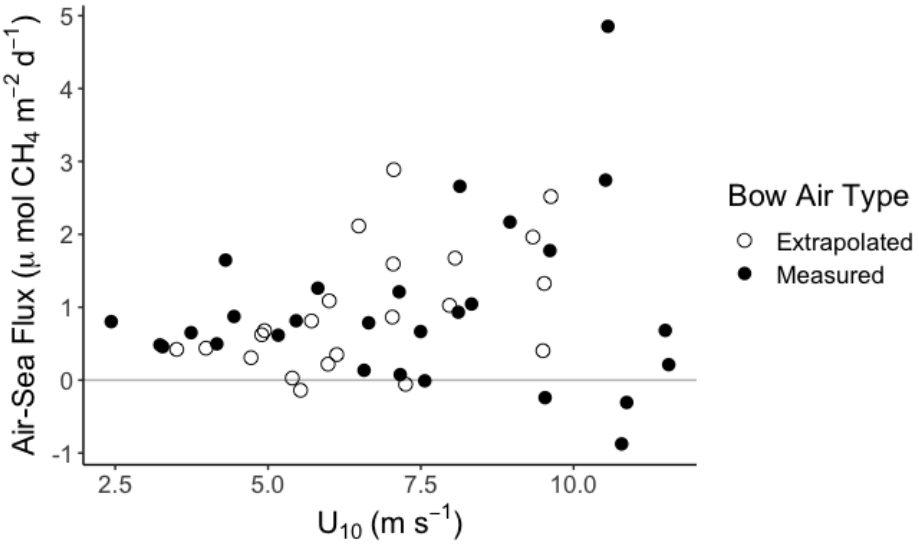

4.3.2 SPATIAL AND TEMPORAL SCALES

Temporal and spatial scales must also be considered when discussing GP15 CH_4 flux trends. Latitudinal differences in atmospheric CH_4 between the Northern and Southern Hemispheres have been previously reported (e.g., Forster et al. 2009; Reeburgh 2007; Chronopoulou et al. 2017). As aforementioned, the GP15 transect covers four distinct physical regimes: subarctic, temperate, subtropical, and equatorial (Levitus 1982). Figures 4.14 and 4.15 demonstrate the changes in temperature and salinity, respectively. The following paragraphs will outline the trends observed in the Subarctic North Pacific/Alaskan Margin (55 to 57 °N), Temperate North Pacific (30 to 55 °N), Subtropical North Pacific (10 to 30 °N), and Equatorial (North and South)/South Pacific (10 °N to 20 °S).

Figure 4.14 *Methane air-sea exchange fluxes for all stations with temperature color bar*

Methane air-sea fluxes (µmol CH_4 m^{-2} d^{-1}) with latitude (°N) for the GP15 transect. Circles indicate bow air CH_4 concentration was extrapolated, and triangles indicate bow air CH_4 was measured. Error bars reflect the error of determination, which were calculated by propagation of errors. Colors indicate temperature (°C). Dashed lines at 10 °N, 30 °N, and 55 °N represent changes in regime from Equatorial North and South Pacific to Subtropical North Pacific to Temperate North Pacific and to Alaskan Margin, respectively.

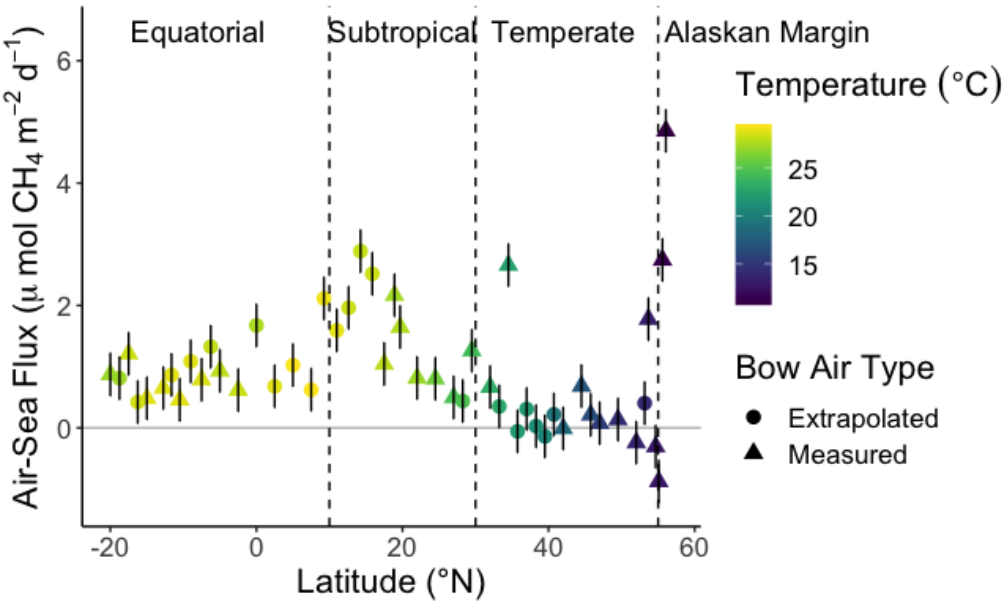

Figure 4.15 *Methane air-sea exchange fluxes for all stations with salinity color bar*

Methane air-sea fluxes (μmol CH_4 m^{-2} d^{-1}) with latitude (°N) for the GP15 transect. Circles indicate bow air CH_4 concentration was extrapolated, and triangles indicate bow air CH_4 was measured. Error bars reflect the error of determination, which were calculated by propagation of errors. Colors indicate salinity. Dashed lines at 10 °N, 30 °N, and 55 °N represent changes in regime from Equatorial North and South Pacific to Subtropical North Pacific to Temperate North Pacific and to Alaskan Margin, respectively.

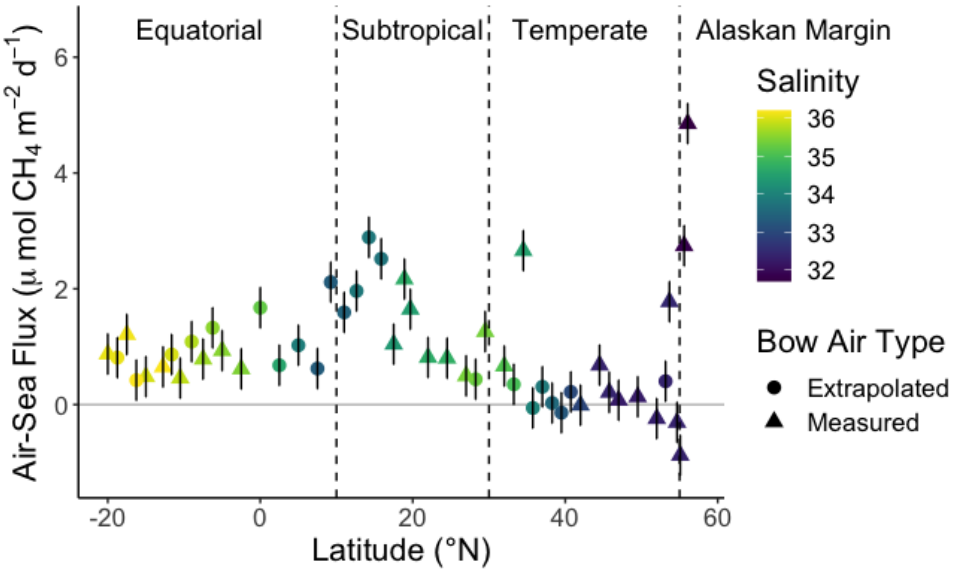

The Subarctic North Pacific/Alaskan Margin section included the three margin stations. Temperature and salinity were lower than values measured in the Subtropical/Equatorial North and South Pacific (Fig. 4.14 and 4.15). Subarctic regions are known to often exhibit lower salinities because of excess precipitation compared to evaporation (Levitus 1982). Between the three margin stations, both the highest and lowest CH_4 fluxes of the entire transect were observed (Table A.1). Coastal waters produce some of the largest air-sea exchange CH_4 fluxes (e.g., Weber et al. 2019; Yoshikawa et al. 2014). Primary productivity and nutrient loads tend to be high, fueling production of OM. Previous studies have noted CH_4 seasonal cycles are tied with OM

availability through influencing rates of methanogenesis and CH_4 oxidation (e.g., Borges et al. 2017; Burke Jr. et al. 1983). The breakdown of OM can facilitate aerobic methanogenesis or anaerobic methanogenesis in small anoxic pockets (Reebugh 2007; Popp et al. 1995; Bange et al. 1994; Karl et al. 2008). Redox reactions in oxygen-limiting conditions may utilize Mn and CH_4 as terminal electron acceptors (Reeburgh 2007). Stations 1-3 along the continental margin were the shallowest stations sampled. As a result of the shallowness and higher rates of primary productivity noted in this region, benthic CH_4 sources may have influenced the CH_4 distribution measured at these stations. Figures 4.16 and 4.17 highlight elevated CH_4 and Mn concentrations below the mixed layer at stations 1 and 2. At both stations, methanogenesis associated with deep chlorophyll maxima may have contributed to relatively elevated CH_4 concentrations near 50 m (Fig. 4.16 and 4.17). At station 2, a sediment source appears to contribute to elevated CH_4 and Mn concentrations between 150 and 250 m (Fig. 4.16 and 4.17).

Figure 4.16 *Methane concentration at stations 1 and 2*

Methane (CH_4) concentration (nmol kg^{-1}) at GP15 stations 1 and 2 along the Alaskan Margin. Red circles indicate measurements from station 1, and blue squares indicate measurements from station 2.

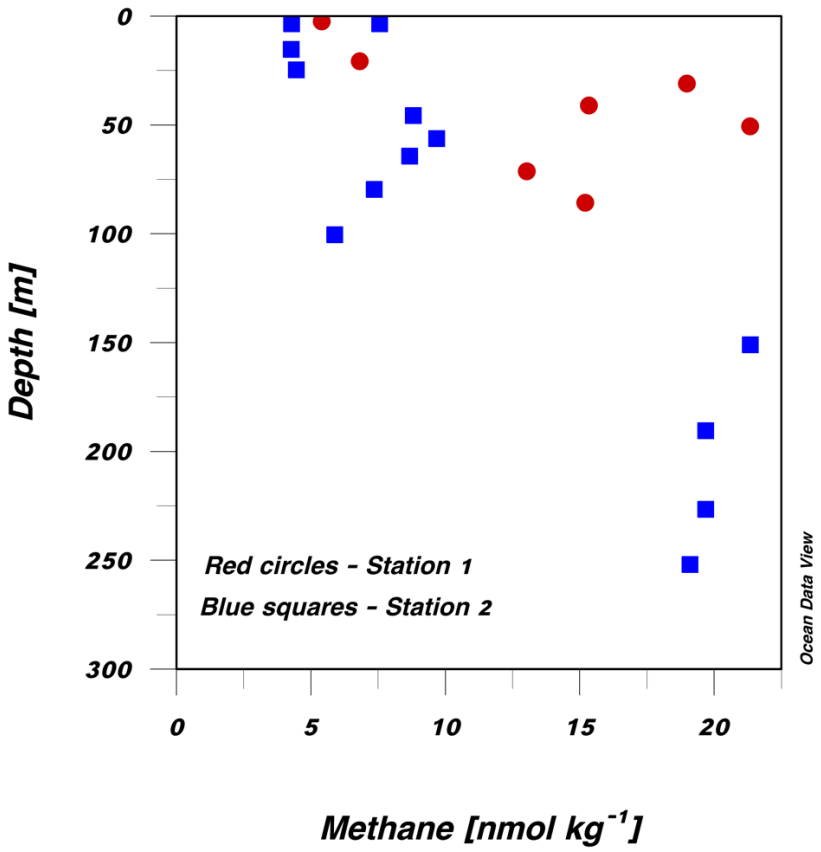

Figure 4.17 *Manganese concentration at stations 1 and 2*

Manganese (Mn) concentration (nmol kg^{-1}) at GP15 stations 1 and 2 along the Alaskan Margin. Red circles indicate measurements from station 1, and blue squares indicate measurements from station 2.

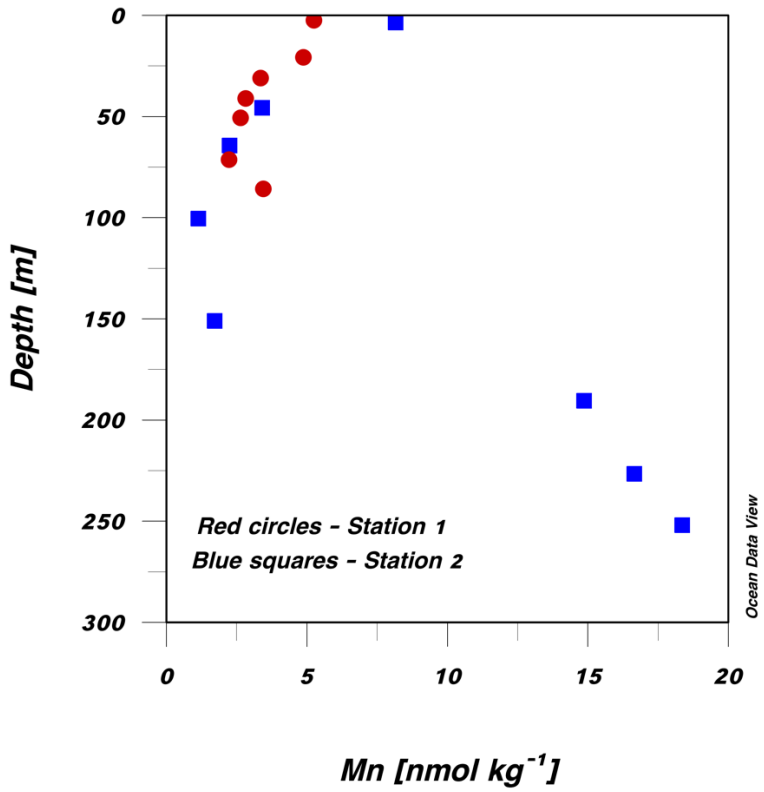

The Temperate North Pacific (30 to 55 °N) included stations 4 to 14. Temperatures increased with decreasing latitude (Fig. 4.14), and salinities observed in near-surface waters were lower than those observed farther south (Fig. 4.15). Some of the lowest CH_4 fluxes measured on the GP15 cruise were found around 40 to 55 °N (Fig. 4.7). Multiple stations had fluxes that could not be determined to be significantly different from zero (e.g., 0 ± 1σ µmol CH_4 m^{-2} d^{-1}; Table A.1). Additionally, CH_4 fluxes could be lower if the system was near equilibrium, such as where wind speed and k were relatively high (> 7.5 m s^{-1} and > 1.5 m d^{-1}, respectively) but CH_4 flux was low (Fig. 4.11

and 4.12). In the absence of additional coastal, benthic, or atmospheric sources, CH_4 fluxes were expected to be lower with CH_4 oxidation as the primary sink (e.g., Reeburgh 2007). As a result, CH_4 oxidation could have been an important factor at Temperate North Pacific stations, driving lower CH_4 flux values (e.g., Pack et al. 2015).

Subtropical North Pacific (10 to 30 °N) included stations 15 to 21. In this section, CH_4 fluxes increased with decreasing latitude (Fig. 4.7). Some of the maximum values seen at the open ocean stations were measured in this latitudinal range (Fig. 4.10). Temperatures increased with decreasing latitude (Fig. 4.15), and salinity increased relative to salinities observed in the Subarctic and Temperate North Pacific (Fig. 4.16). Subtropical salinity maxima are common because of excess evaporation compared to precipitation (Levitus 1982). U_{10} wind speeds increased moving equatorward (Fig. 4.12). Gas transfer velocity (k) values were higher (> 1.5 m d^{-1}) in this region (Fig. 4.13). Near-surface seawater CH_4 concentrations were variable with some stations having relatively higher CH_4 fluxes than adjacent sections but moderately different CH_4 concentrations (Fig. 4.7 and 4.10). Considering only these physical parameters does not fully explain the differences in CH_4 fluxes observed in the Subtropical North Pacific.

Finally, the Equatorial (North and South)/South Pacific region (10 °N to 20 °S) included stations 22 to 39. Physical drivers in this region include equatorial currents, upwelling, and changing wind regimes. Equatorial currents and countercurrents drive advective fluxes of water poleward through Ekman transport (Levitus 1982). Atmospheric CH_4 (measured as bow air CH_4) decreased with decreasing latitude when moving from subtropical to equatorial waters (Fig. 4.8). Equatorial upwelling can also introduce higher nutrient waters, which fuels greater rates of primary productivity. As

previously mentioned, upwelled waters can contain lower concentrations of CH_4. Perhaps this could help explain why CH_4 fluxes appeared to decrease relative to those measured in the Subtropical North Pacific (Fig. 4.10). Interestingly, CH_4 fluxes in the equatorial waters and South Pacific were not significantly different, suggesting that another factor besides equatorial upwelling could be influencing CH_4 fluxes in both regions. In the subsequent sections, biogeochemical factors that may influence CH_4 flux along the GP15 transect will be discussed.

Differences between the regions of GP15 transect may be influenced by seasonal changes. Samples were collected from September to November 2018. Mixed layer depth (MLD) exhibits temporal changes (Monterey and Levitus 1997). In the Pacific Ocean, the mixed layer typically deepens between August and October then reaches its deepest points between November and January (Monterey and Levitus 1997; Levitus 1982). There is some evidence of mixed layer deepening moving from ~10 °N to 10 °S (Fig. 4.18). There appears to be some deepening of MLD from ~40 to 20 °N (Fig. 4.18). Vertical mixing may be a more pronounced factor in winter months (Monterey and Levitus 1997; Ganachaud and Wunsch. 2000). Although the seasonality of these factors can certainly influence CH_4 fluxes and CH_4 distribution, no clear trends could be distinguished in the GP15 dataset.

Figure 4.18 *Mixed layer depth with latitude and average mixed layer methane color bar*

Mixed layer depth (m) with latitude (°N) for the GP15 transect. Colors indicate average mixed layer CH_4 concentration (nmol kg^{-1}).

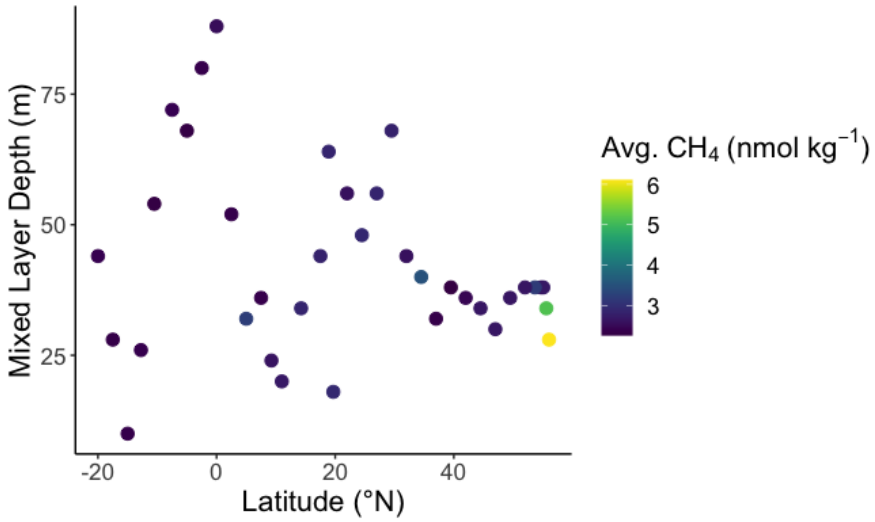

4.4 NUTRIENT REGIMES

Stations in the Subarctic North Pacific and around 10 °N exhibit some of the highest surface water nitrate (NO_3) and phosphate (PO_4) concentrations observed along the GP15 transect (Fig. 4.19 and 4.20, respectively; Table A.3). Throughout the Subtropical North Pacific and South Pacific, surface water NO_3 and PO_4 concentrations were lower (Fig. 4.19 and 4.20, respectively). It is well-documented that NO_3 and PO_4 concentrations are often low in open surface ocean waters (e.g., Broecker et al. 1998; Paytan and McLaughlin 2007; Dugdale and Goering 1967). Changes in NO_3 and PO_4 concentrations between 10 °N and 10 °S suggested influences of equatorial upwelling on nutrient abundance north and south of the equator (Fig. 4.19 and 4.20, respectively). Upwelling brings deeper, more nutrient-rich waters to the surface, which can fuel primary productivity (e.g., Paytan and McLaughlin 2007; Burnett, Roe, and Piper 1983).

Figure 4.19 *Nitrate concentration in upper 500 m*

Nitrate concentration (µmol kg^{-1}) in upper 500 m of water column of GP15 transect. Black dots indicate sampling locations.

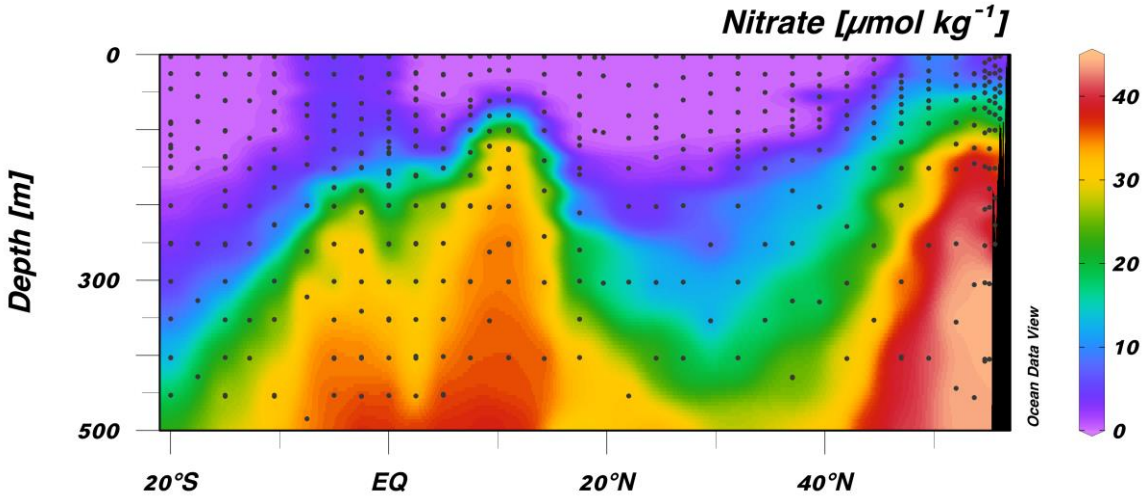

Figure 4.20 *Phosphate concentration in upper 500 m*

Phosphate concentration (µmol kg^{-1}) in upper 500 m of water column of GP15 transect. Black dots indicate sampling locations.

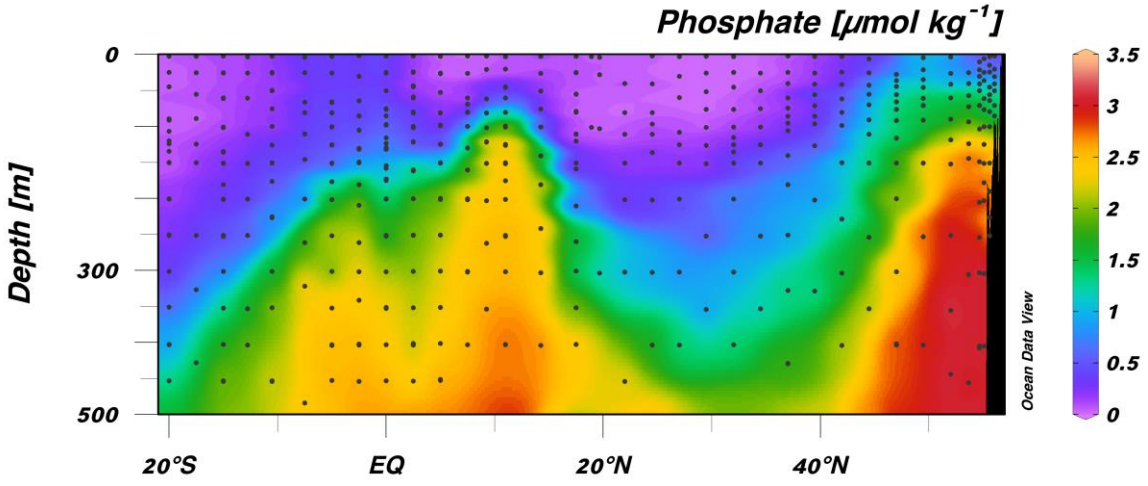

Examining average NO_3 and PO_4 concentrations in the mixed layer provides more insight into processes that could influence CH_4 fluxes. Average mixed layer NO_3 concentrations peaked in the Subarctic North Pacific (~50 °N; Fig. 4.21). Throughout the Subtropical and Temperate North Pacific, average mixed layer NO_3 concentrations were below detection (Fig. 4.21). Average mixed layer NO_3 concentrations increased south of the equator then dropped below detection limits around 10 °S (Fig. 4.21). Average mixed layer PO_4 concentrations exhibited similar trends with fewer data points below detection (Fig. 4.22). The lowest observed average mixed layer PO_4 concentrations were in the Subtropical North Pacific and in the Equatorial North Pacific (Fig. 4.22). Average CH_4 fluxes were higher in the Subtropical North Pacific and Equatorial North and South Pacific than in the Temperate North Pacific. Limitations in PO_4 availability may have influenced utilization of MPn, resulting in higher CH_4 mixed layer concentrations and fluxes (Table 4.2). Average mixed layer PO_4 concentrations increased near the equator then declined moving south beyond ~5 °S (Fig. 4.22). These data suggest that nutrient conditions were not limiting in the Subarctic North Pacific and in portions near the equator, whereas portions of the Temperate and Subtropical North Pacific may have been nutrient stressed at the time of sampling (Fig. 4.21 and 4.22).

Figure 4.21 *Mixed layer average nitrate concentration with latitude*

Average mixed layer NO_3 concentration (µmol kg^{-1}) with latitude (°N) for GP15 transect. Black triangles indicate measurements that were above detection, and open triangles indicate measurements that were below detection (≤ 0.02 µmol kg^{-1}). Dashed lines at 10 °N, 30 °N, and 55 °N represent changes in regime from Equatorial North and South Pacific to Subtropical North Pacific to Temperate North Pacific and to Alaskan Margin, respectively.

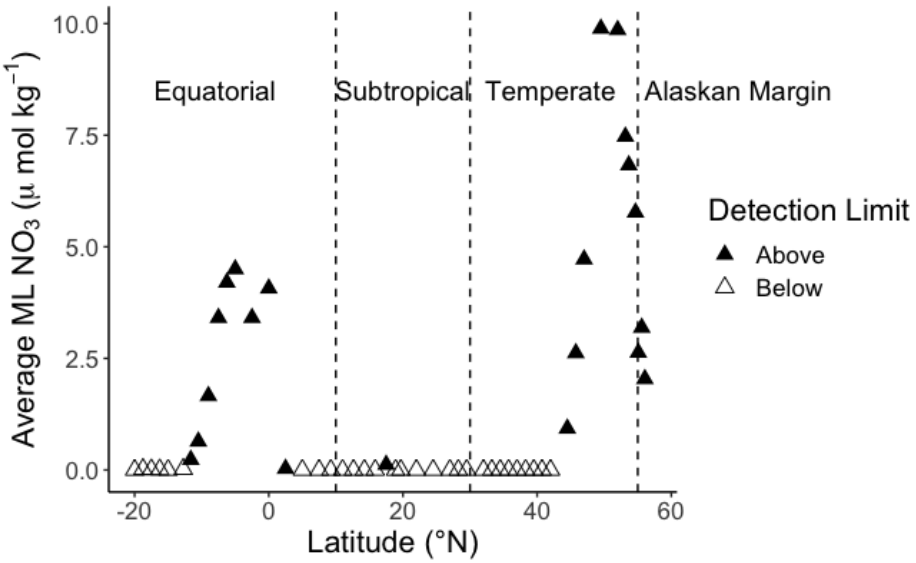

Figure 4.22 *Mixed layer average phosphate concentration with latitude*

Average mixed layer PO_4 concentration (µmol kg^{-1}) with latitude (°N) for GP15 transect. Black triangles indicate measurements that were above detection, and open triangles indicate measurements that were below detection (≤ 0.02 µmol kg^{-1}). Dashed lines at 10 °N, 30 °N, and 55 °N represent changes in regime from Equatorial North and South Pacific to Subtropical North Pacific to Temperate North Pacific and to Alaskan Margin, respectively.

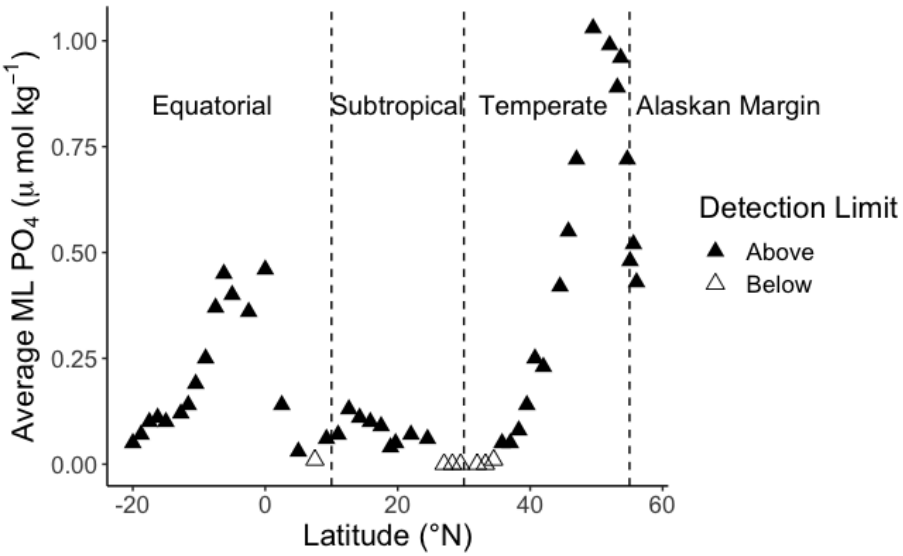

Calculating phosphate star (P*) allows for further assessment of nutrient limitation. However, these calculations are controlled by detection limit for nutrient analyses. P* values were calculated using Equation 19 as described in Deutsch et al. (2007):

(19)

$$P^* = [PO_4] - (1/16) \times [NO_3]$$

P* and N* trends were inverse of each other, as would be expected (Fig. 4.23 and A.3). N* was calculated as described in Gruber and Sarmiento 1997:

(20)

$$N^* = [NO_3] - 16[PO_4] + 2.9$$

P* values were highest in the Subarctic North Pacific and northernmost parts of the Temperate North Pacific (Fig. 4.23). Throughout the Subtropical North Pacific and South Pacific, P* values were near-zero (Fig. 4.23). Near-zero P* values suggest conditions of phosphate limitation (e.g., Broecker et al. 1998). Previous studies have documented MPn utilization in the oligotrophic Subtropical Pacific Ocean (e.g., Karl et al. 2008; Del Valle & Karl 2014; Repeta et al. 2016). MPn utilization uses MPn as a substitute for PO_4 in conditions where PO_4 is low, which produces CH_4 as a by-product (e.g., Karl et al. 2008; Metcalf et al. 2012; Repeta et al. 2016; Sosa et al. 2019). Although MPn utilization rates were not measured directly on the GP15 cruise, stations with higher CH_4 air-sea fluxes in the Subtropical North Pacific associated with near-zero P* values could be correlated with MPn utilization, such as at stations 18.3 to 20 (Table 4.2). The primary limitation of assessment was measurements of $[NO_3]$ below detection. P* values calculated using dissolved oxygen rather than $[NO_3]$ data followed the same trend and can be found in Figure A.4.

Figure 4.23 *Mixed layer average P* with latitude*

Average P* in mixed layer (P^*_{ML}; µmol kg^{-1}) with latitude (°N) for GP15 transect. Black triangles indicate [NO_3] measurements that were above detection, and open triangles indicate [NO_3] measurements that were below detection (≤ 0.02 µmol kg^{-1}). Dashed lines at 10 °N, 30 °N, and 55 °N represent changes in regime from Equatorial North and South Pacific to Subtropical North Pacific to Temperate North Pacific and to Alaskan Margin, respectively.

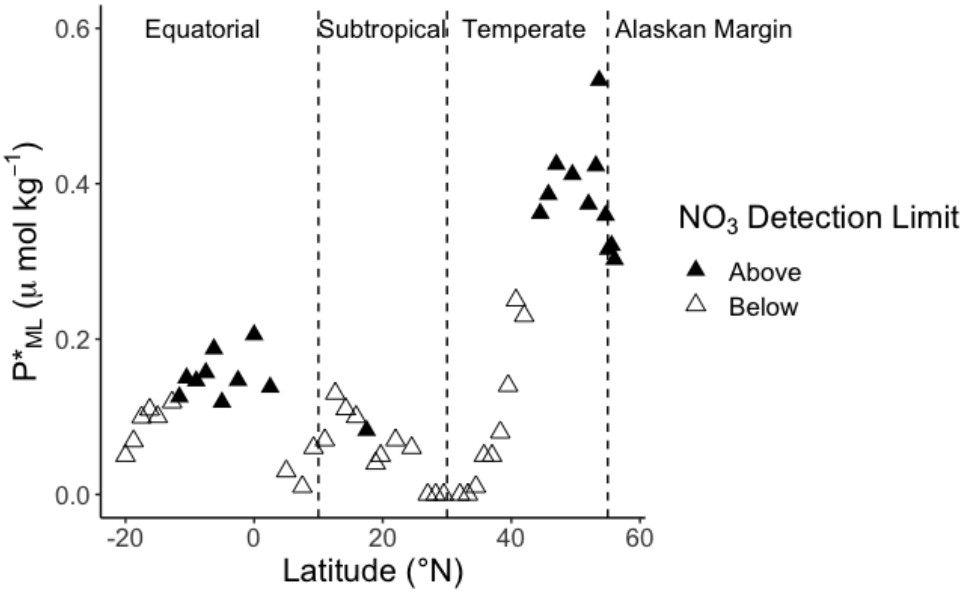

Table 4.2 *Mixed layer nutrient and methane concentration for all stations*

Nutrient ([NO_3] and [PO_4]) and methane (air-sea fluxes, [CH_4], and CH_4 inventory) data within the mixed layer at each GP15 station. ML stands for mixed layer. No mixed layer [CH_4] or CH_4 inventory values are provided for intermediate stations because only near-surface samples were collected with insufficient data for analysis of mixed layer depth. Red font indicates [NO_3] and [PO_4] measurements that were below detection ($\leq$ 0.02 µmol kg^{-1}).

Station	Latitude (°N)	Avg $[NO_3]_{ML}$ (µmol kg^{-1})	Avg $[PO_4]_{ML}$ (µmol kg^{-1})	Avg P^*_{ML} (µmol kg^{-1})	CH_4 Flux (µmol m^{-2} d^{-1})	Avg $[CH_4]_{ML}$ (nmol L^{-1})	CH_{4ML} Inventory (mol)
1	56.06	2.46	0.47	0.31	4.85	6.11	171
2	55.60	3.33	0.54	0.33	2.74	5.15	175
3	55.08	6.12	0.72	0.33	-0.88	2.69	102
4	54.66	5.56	0.72	0.37	-0.31	2.67	101
5	53.67	6.81	0.86	0.43	1.78	3.17	121
5.5	53.16	7.47	0.89	0.42	0.40	NA	NA
6	52.00	9.77	0.98	0.37	-0.24	2.63	99.9
7	49.50	9.90	1.04	0.42	0.13	2.63	94.7
8	47.00	4.72	0.72	0.43	0.08	2.65	79.6
8.5	45.77	2.62	0.55	0.39	0.21	NA	NA
9	44.50	0.89	0.42	0.36	0.68	2.65	90.0
10	42.00	0	0.24	0.24	-0.01	2.4501	88.2
10.5	40.73	0	0.25	0.25	0.22	NA	NA
11	39.50	0	0.15	0.15	-0.14	2.26	85.8
11.5	38.28	0	0.08	0.08	0.03	NA	NA
12	37.00	0	0.06	0.06	0.31	2.33	74.7
12.5	35.75	0	0.05	0.05	-0.06	NA	NA
13	34.50	0	0.01	0.01	2.66	3.50	140

Table 4.2 (continued)

Station	Latitude (°N)	Avg $[NO_3]_{ML}$ ($\mu mol\ kg^{-1}$)	Avg $[PO_4]_{ML}$ ($\mu mol\ kg^{-1}$)	Avg P^*_{ML} ($\mu mol\ kg^{-1}$)	CH_4 Flux ($\mu mol\ m^{-2}\ d^{-1}$)	Avg $[CH_4]_{ML}$ ($nmol\ L^{-1}$)	CH_{4ML} Inventory (mol)
13.5	33.25	0	0	0.00	0.35	NA	NA
14	32.00	0	0	0.00	0.67	2.57	113
15	29.50	0	0	0.00	1.26	2.80	190
15.5	28.25	0	0	0.00	0.44	NA	NA
16	27.00	0	0	0.00	0.50	2.86	160
17	24.50	0	0.06	0.06	0.80	2.90	139
18	22.00	0	0.07	0.07	0.81	2.57	144
18.3	19.68	0	0.05	0.05	1.65	2.91	52.3
18.6	18.91	0	0.04	0.04	2.17	2.86	183
19	17.50	0.06	0.10	0.09	1.04	2.81	124
19.5	15.86	0	0.10	0.10	2.52	NA	NA
20	14.25	0	0.11	0.11	2.89	2.85	96.8
20.5	12.63	0	0.13	0.13	1.96	NA	NA
21	11.00	0	0.07	0.07	1.59	2.69	53.8
22	9.25	0	0.06	0.06	2.11	2.61	62.7
23	7.50	0	0.02	0.02	0.62	2.37	85.4
25	5.00	0	0.03	0.03	1.03	3.20	103
27	2.50	0.03	0.13	0.13	0.68	2.36	123
29	0.00	4.19	0.49	0.23	1.67	2.52	222
31	-2.50	3.46	0.39	0.18	0.62	2.37	190
33	-5.00	4.56	0.40	0.11	0.93	2.28	155
33.5	-6.25	4.20	0.45	0.19	1.33	NA	NA

Table 4.2 (continued)

Station	Latitude (°N)	Avg $[NO_3]_{ML}$ (µmol kg^{-1})	Avg $[PO_4]_{ML}$ (µmol kg^{-1})	Avg P^*_{ML} (µmol kg^{-1})	CH_4 Flux (µmol m^{-2} d^{-1})	Avg $[CH_4]_{ML}$ (nmol L^{-1})	CH_{4ML} Inventory (mol)
34	-7.50	3.44	0.38	0.16	0.79	2.42	174
34.5	-9.00	1.66	0.25	0.15	1.09	NA	NA
35	-10.50	0.58	0.18	0.14	0.46	2.2737	123
35.5	-11.63	0.23	0.14	0.13	0.86	NA	NA
36	-12.75	0.01	0.12	0.11	0.65	2.40	62.3
37	-15.00	0	0.10	0.10	0.48	2.34	23.4
37.5	-16.25	0.01	0.11	0.11	0.42	NA	NA
38	-17.50	0.01	0.09	0.09	1.21	2.33	65.1
38.5	-18.75	0.02	0.07	0.07	0.81	NA	NA
39	-20.00	0.00	0.04	0.04	0.87	2.41	106

4.5 RARE EARTH ELEMENTS AND TRANSITION METALS

Lanthanum (La) concentrations were highest near the continental margin (Fig. 4.24). Higher La concentrations below 300 m depth near 20 °N than at stations farther south were observed (Fig. 4.24). Previous work by Jenkins et al. (2020) noted hydrothermal sources of REEs from Loihi Seamount and Puna Ridge sources, but these inputs would not influence near-surface conditions. Although hydrothermal sources introduce REEs into the water column, LREEs can be preferentially removed through scavenging in hydrothermal systems (e.g., Pol et al. 2014). Throughout surface waters in the rest of the transect, La concentrations were less than 5 pmol kg^{-1} (Fig. 4.24).

Figure 4.24 *Lanthanum concentration in upper 500 m*

Lanthanum (La) concentration (pmol kg^{-1}) in upper 500 m of water column for GP15 transect. Black dots indicate sampling locations.

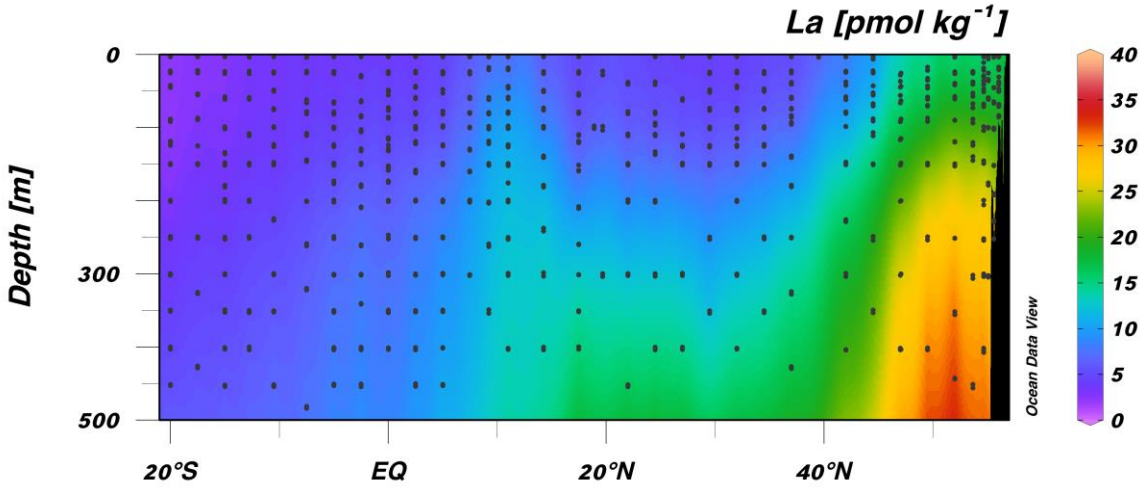

To further assess enrichments and depletions of LREEs, the La anomaly was calculated using praseodymium (Pr) and neodymium (Nd) concentrations normalized to Post-Archaean Australian Shale (PAAS) as described in Wang et al. (2020; Eq. 11 and 12). Molar concentrations of Pr and Nd in the upper 500 m are shown in Figures A.5 and A.6. The presence of La anomalies can be used as a proxy for past methanotrophic activity (Wang et al. 2020; Meyer et al. 2021; Wang et al. 2021) because LREEs can be depleted during CH_4 oxidation for use as co-factors in enzymes, such as MDH (Semrau et al. 2018; Pol et al. 2014; Shiller et al. 2017; Daumann 2019). Therefore, lower La anomalies can be indicative of CH_4 oxidation. The La anomaly is essentially the ratio of measured La to La* as predicted from Pr and Nd (with all values shale-normalized). Thus, I refer to La anomaly values as "positive" when greater than 1 and "negative" when less than 1 (Fig. 4.25; Eq. 11 and 12).

Along the continental margin, negative to slightly positive La anomalies were observed in the upper 100 m. Coinciding signals of negative La anomalies and the highest and lowest CH_4 fluxes are compatible with CH_4 oxidation as a driver of change from steady state at these stations. Stations throughout the Subtropical North Pacific, Equatorial Pacific, and South Pacific exhibited negative La anomalies in the upper 100 m, providing additional support for CH_4 oxidation as a driver of air-sea exchange CH_4 fluxes in surface waters (Fig. 4.25). Some stations in the Temperate North Pacific also exhibited positive La anomalies in surface waters (Fig. 4.25). Photo-inhibition of some methanotrophs in the upper water column has been reported (e.g., Shelley et al. 2017; Kimura et al. 1999). Therefore, as reported by Meyer et al. (2021), depletions of LREEs may not be observed in near-surface waters. The same process may have influenced positive La anomalies south of 10 °S (Fig. 4.25).

In the North Pacific, waters below 100 m frequently exhibited negative La anomalies. Methane oxidation was expected to be the primary sink of CH_4 below surface waters, and observations of negative La anomalies support this assessment, perhaps through use of LREEs as a co-factor in XoxF MDH (Semrau et al. 2018; Pol et al. 2014; Alibo and Nozaki 1999). Furthermore, even though CH_4 oxidation rates are slow in this region (Pack et al. 2015), it is still an important oceanic CH_4 sink.

Figure 4.25 *Lanthanum anomaly in upper 500 m*

Lanthanum (La) anomaly in the upper 500 m of the water column. “Positive” and “negative” anomalies are determined relative to 1, meaning colors in red to yellow are positive, and colors in blue are negative anomalies.

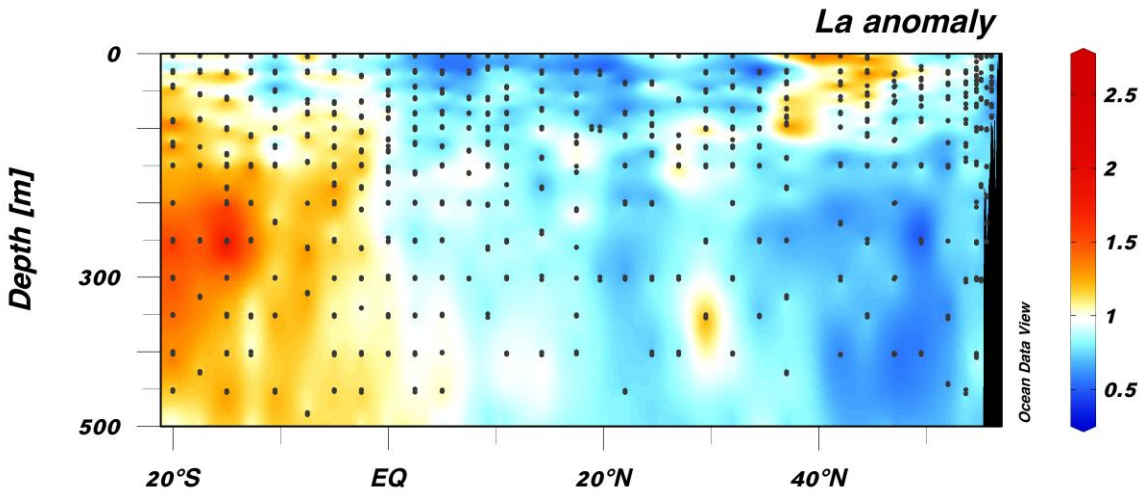

Some of the GP15 stations exhibited higher CH_4 fluxes coinciding with negative La anomalies. When performing a linear regression, there was minor correlation (R = 0.354) between more negative La anomalies and higher CH_4 fluxes (Fig. 4.26). However, this trend was best applied to specific stations (i.e., stations 1 and 2) rather than the entire transect. It is worth noting that the continental margin stations exhibited the extremes of the range for both CH_4 fluxes and La anomalies. When excluding these stations, no significant correlations between CH_4 fluxes and La anomalies were observed (Fig. A.7). While depletions in La can be indicative of CH_4 oxidation, this factor alone does not explain the trends in CH_4 fluxes for the GP15 transect.

Figure 4.26 *Linear regression of lanthanum anomaly versus methane air-sea exchange fluxes*

Methane air-sea fluxes (µmol m^{-2} d^{-1}) with lanthanum (La) anomaly for all stations. The linear regression (blue line) is y = -0.304x + 2.016 (R = 0.354).

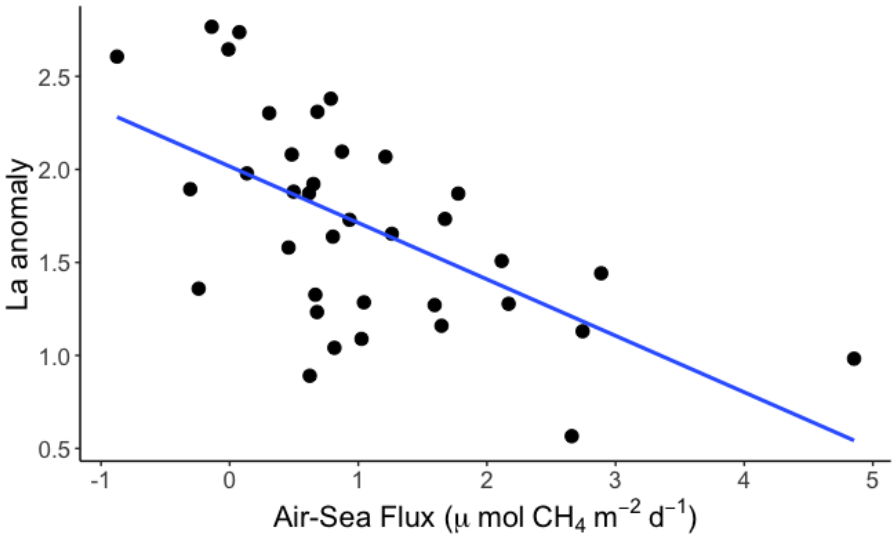

Analysis of La/Yb ratios and LREEs to HREEs allow for another method of assessing drawdown of LREEs. Regions with lower La/Yb and LREE/HREE ratios coinciding with lower CH_4 concentrations could be indicative of CH_4 oxidation. In the upper 500 m of the water column, La/Yb ratios were highest near the continental margin; higher La/Yb ratios continued to around 40 °N (Fig. 4.27). The persistence of this signal across two physical regimes suggests possible advective fluxes from the Subarctic North Pacific to Temperate North Pacific. La/Yb ratios were lower in the Subtropical North Pacific and South Pacific (Fig. 4.27). Some of the lowest values were observed in equatorial waters, which may be indicative of upwelling (Fig. 4.27). Waters below the euphotic zone have been noted to have active biologically mediated uptake of REEs, with fractionation due to preferential uptake of LREEs, which results in upwelled waters

having greater REE fractionation than surface waters (Meyer et al. 2021; Jensen et al. 2008). La/Yb ratios from ~10 °N to ~10 °S were markedly lower than those from 10 to 20 °N (Fig. 4.27). Furthermore, CH_4 fluxes were significantly different between the Subtropical North Pacific and Equatorial North/South Pacific (Fig. 4.7 and 4.10). It is plausible that differences in REE fractionation and use of LREEs for methanotrophy could have influenced the differences in CH_4 flux between these regions.

Figure 4.27 *Lanthanum to ytterbium ratio in upper 500 m*

Ratio of lanthanum (La) to ytterbium (Yb) in upper 500 m of water column for GP15 transect. Black dots indicate sampling locations.

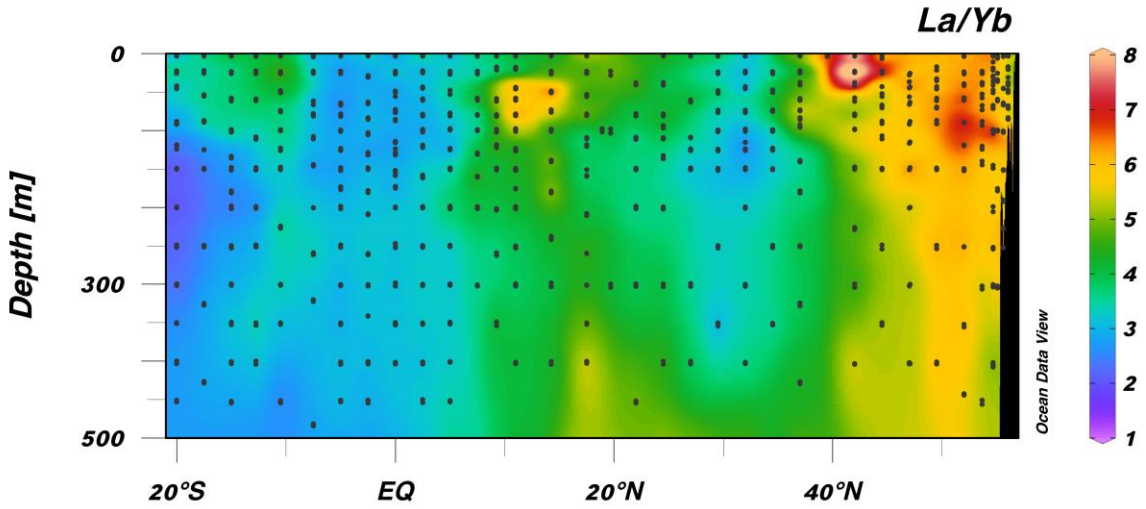

LREE/HREE ratios can also be a potential marker of methanotrophy (Meyer et al. 2021). Other trivalent LREEs than La can be used as enzyme co-factors (e.g., Daumann 2019; Chistoserdova 2019). Drawdown of LREEs would result in lower LREE/HREE values, which could be indicative of CH_4 oxidation. Lower values of LREE/HREE ratios, relative to surface waters, observed in deeper waters (Fig. 4.28) could be indicative of

CH_4 oxidation, a known primary sink for oceanic CH_4 below surface waters (e.g., Chan et al. 2019; Meyer et al. 2021). Some of the highest LREE/HREE ratios are observed near the continental margin (Fig. 4.28). LREE fractionation could be influenced by inputs from the continental margin, thereby leading to higher ratios of La to Yb and LREEs to HREEs at stations closest to the Alaskan Margin (Fig. 4.27 and 4.28). Elevated LREE/HREE ratios around 20 °N in the upper 150 m were unlikely to have been influenced by hydrothermal activity at Loihi Seamount and Puna Ridge (Fig. 4.28), as noted by Jenkins et al. (2020). Analysis of REEs provides support for CH_4 oxidation influencing CH_4 fluxes along the GP15 transect.

Figure 4.28 *Light rare earth elements to heavy rare earth elements ratio in upper 500 m*

Ratio of light rare earth elements (LREEs; La, Pr, and Nd) to heavy rare earth elements (HREEs; Sm, Eu, Gd, Tb, Dy, Ho, Er, Tm, Yb, and Lu) in upper 500 m of water column for GP15 transect. Black dots indicate sampling locations.

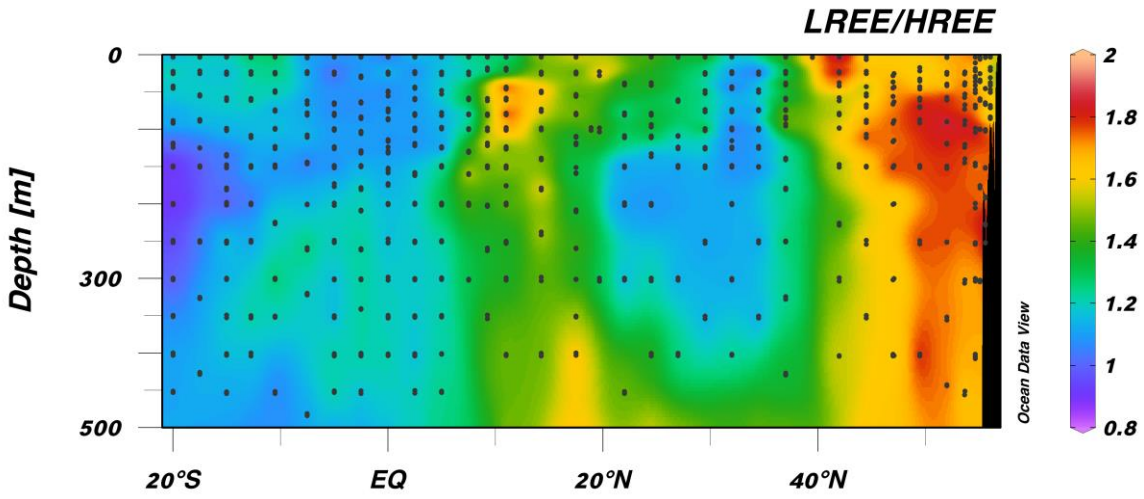

Finally, some transition metals have been noted to be associated with methanotrophy (e.g., Semrau et al. 2018). Particulate MMO uses Cu as a co-factor; therefore, Cu depletions can be indicative of CH_4 oxidation (Semrau et al. 2018). Near-

surface waters south of 40 °N exhibited lower Cu concentrations than those along the continental margin (Fig. 4.29). Lower Cu concentrations, relative the continental margin, do not necessarily suggest its use in pMMO for methanotrophy (Fig. 4.29). Rather, it is possible that Cu concentration was low because it is a trace metal present in lower abundance for a given region, rather than depletion through use in CH_4 oxidation, although this CH_4 sink was certainly important in this region.

Figure 4.29 *Copper concentration in upper 500 m*

Copper (Cu) concentration (nmol kg^{-1}) in upper 500 m of water column for GP15 transect. Black dots indicate sampling locations. Light peach color indicates concentration > 2.5 nmol kg^{-1}.

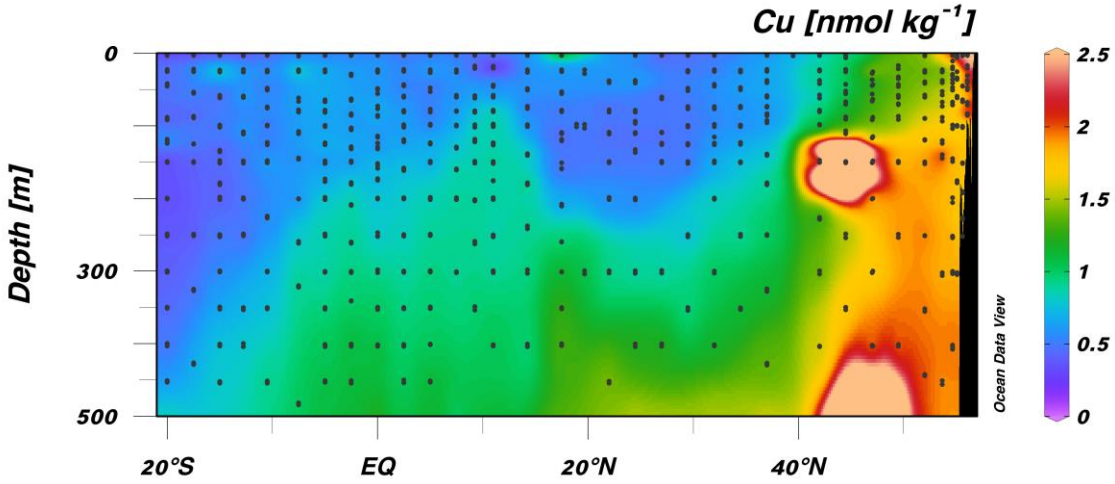

Like Cu, nickel (Ni) showed higher concentrations along the continental margin (Fig. 4.30). Near-surface waters had lower Ni concentrations than intermediate waters (Fig. 4.30). As with Cu, Ni concentrations may be low due to its naturally lower abundance in the water column rather than depletion associated with CH_4 oxidation. Furthermore, there were few correlations observed to suggest that Cu and Ni concentrations were driven by use as enzyme co-factors for CH_4 oxidation in surface waters (Fig. 4.29 and 4.30, respectively).

Figure 4.30 *Nickel concentration in upper 500 m*

Nickel (Ni) concentration (nmol kg^{-1}) in upper 500 m of water column for GP15 transect. Black dots indicate sampling locations.

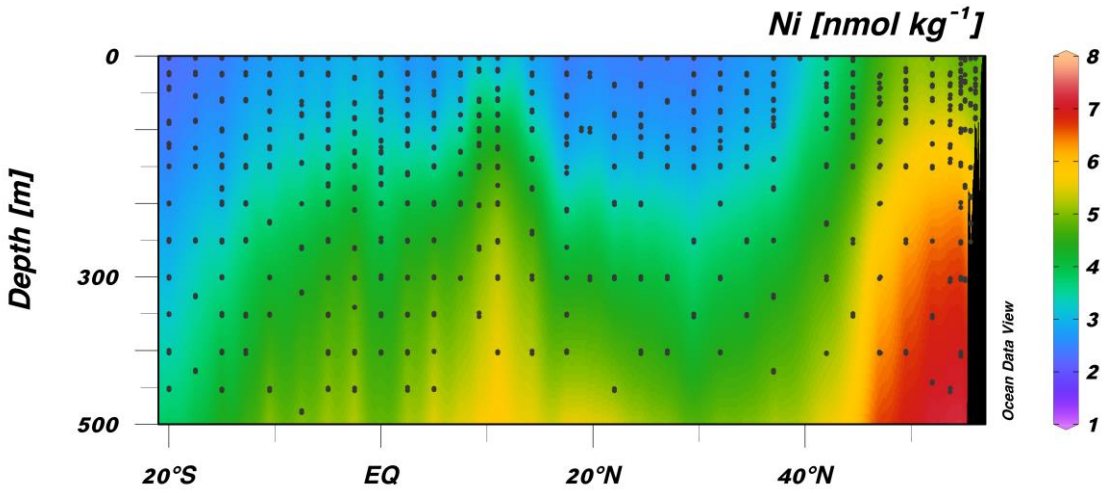

Mn in the upper 500 m of the water column exhibited similar trends to Ni and Cu in that it also had its highest concentrations near the continental margin (Fig. 4.31). Elevated Mn concentrations relative to other open ocean stations were observed around 20 °N, which coincides with Loihi Seamount and Puna Ridge (Fig. 4.5 and 4.31). However, hydrothermal activity was unlikely to have influenced Mn concentrations in the upper 200 m of the water column. Cerium (Ce) was also higher around 20 °N, suggesting that both Mn and Ce were influenced by redox processes (e.g., Mofflet 1994) near these stations (Fig. 4.31 and 4.32, respectively). However, there were no clear trends with Mn and Ce distribution in near-surface waters throughout the transect (Fig. 4.31 and 4.32, respectively).

Figure 4.31 *Manganese concentration in upper 500 m*

Manganese (Mn) concentration (nmol kg^{-1}) in upper 500 m of water column for GP15 transect. Black dots indicate sampling locations.

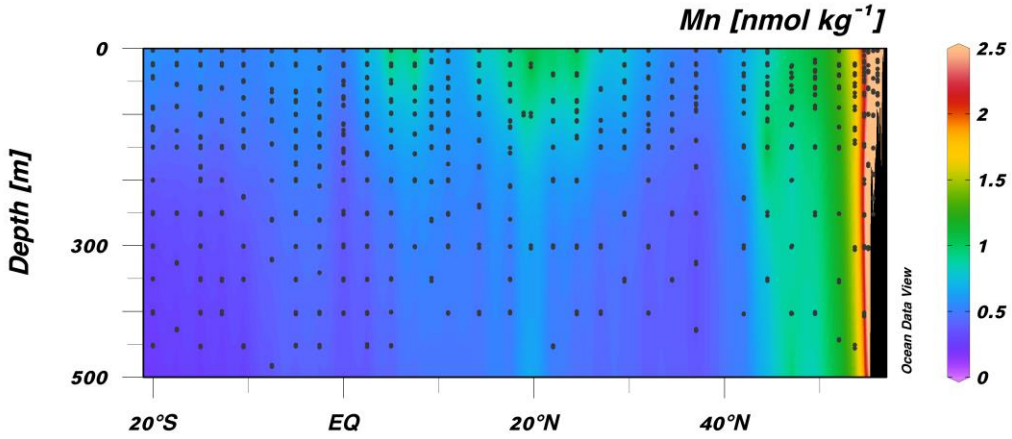

Figure 4.32 *Cerium concentration in upper 500 m*

Cerium (Ce) concentration (pmol kg^{-1}) in upper 500 m of water column for GP15 transect. Black dots indicate sampling locations.

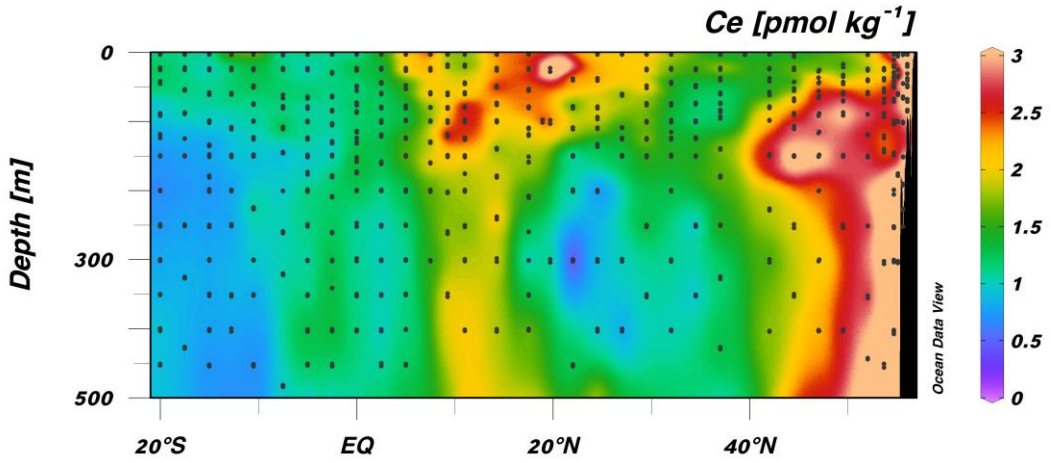

CHAPTER V – SUMMARY

The GEOTRACES GP15 Pacific Meridional Transect (PMT) cruise was conducted from the Aleutian Islands (USA) to Papeete (Tahiti), covering a variety of oceanographic regimes. Samples were collected for methane (CH_4), transition metals (TMs), and rare earth elements (REEs).

Bow air [CH_4], near-surface seawater [CH_4], and U_{10} wind speeds significantly differed between the Northern and Southern Hemispheres. Despite differences in parameters that contribute to CH_4 flux calculations, no significant differences in CH_4 fluxes between the North and South Pacific were observed. However, significant differences between gyre regimes were observed. Average CH_4 fluxes in the Temperate North Pacific (30 to 55 °N) significantly differed from average fluxes in the Subtropical North Pacific (10 to 30 °N) and Equatorial North and South Pacific (10 °N to 20 °S). Although average CH_4 fluxes in the Alaskan Margin (55 to 57 °N) did not significantly differ from the other gyre regimes, the highest and lowest fluxes were measured in this region. Despite the variety of unique sampling regimes, calculated GP15 air-sea CH_4 fluxes fell within the range of previously reported values.

Previous studies in the central Pacific and other oligotrophic regions have noted MPn utilization in P-limiting conditions, which produces CH_4 as a by-product (e.g., Karl et al. 2008; Metcalf et al. 2012; Repeta et al. 2016; Sosa et al. 2018). In the subtropical North Pacific near 20 °N, higher CH_4 fluxes and seawater CH_4 concentrations compared to the temperate North Pacific and the equatorial Pacific were observed. Negative P* values were calculated at these stations, suggesting P-limiting conditions. These observations suggest a possibility of MPn utilization influencing greater CH_4

concentrations in the mixed layer, leading to higher CH_4 fluxes at these stations relative to other open ocean ones.

Negative La anomalies in portions of the subtropical North Pacific and the equatorial Pacific suggest La depletion. La/Yb and LREE/HREE ratios were also lower in portions of these regions, coinciding with lower CH_4 concentrations. It is possible that CH_4 oxidation using LREE-dependent enzymes occurred to reduce CH_4 concentrations and fluxes in the subtropical North and the equatorial Pacific. At open ocean stations in the South Pacific with lower CH_4 fluxes relative to those around 20 °N, CH_4 concentrations and La/Yb ratios were lower than those observed north of the equator, suggesting possible La depletions associated with CH_4 oxidation.

Future improved measurements could expand the understanding of this dataset and the biogeochemical and physical processes influencing CH_4 distribution and air-sea exchange fluxes in the Pacific Ocean. Direct methane oxidation measurements would greatly aid analyses of GP15 trace element and CH_4 data. Work by Pack et al. (2015) and Chan et al. (2019) outlines methods for methane oxidation incubation experiments. As noted by Pack et al. (2015), studies of CH_4 oxidation rates in the open ocean are rare, so further research would greatly improve scientific understanding of CH_4 oxidation outside of active hydrocarbon seep sites. Direct measurements of MPn utilization along the GP15 transect would also have been very beneficial. Previous work by Karl et al. (2008) and Repeta et al. (2016) have reported MPn utilization in the Pacific Ocean. Rate measurements from the GP15 cruise would offer more direct comparisons between CH_4 fluxes measured at open ocean stations and MPn utilization. Furthermore, measurements using nanomolar nutrient (or nanonutrient) techniques aboard the GP15 cruise may

provide support for conditions of nutrient limitation in the Subtropical North Pacific. Nitrate and phosphate measurements were frequently below detection in this region. Nanonutrient data would allow for more accurate data and determination of nutrient limitations through P* and N* calculations. Methods for nanonutrient techniques can be found in Cutter et al. (2017) and Becker et al. (2019). Having MPn utilization rates and nanonutrient data would be extremely beneficial for analysis of the proposed hypotheses regarding CH_4 fluxes in the open ocean. Despite these sampling limitations, the various types of data collected on the GP15 cruise allow for broader comparisons to CH_4 distribution to better elucidate the influences of various biogeochemical and physical processes and build on the existing knowledge, especially for the open ocean, which has, historically, been less frequently sampled.

APPENDIX

Table A.1 *Methane air-sea exchange flux and mixed layer parameters for all stations*

A summary of parameters relating to methane (CH_4) air-sea exchange flux calculations and mixed layer CH_4 concentration. BA means bow air, D means discrete near-surface seawater, and ML means mixed layer. Depth indicates depth at which CH_{4D} was collected. Standard deviation (SD) determined by propagation of errors are included with CH_4 fluxes. Red font indicates stations for which CH_4 flux could not be determined to be significantly different from zero (within 0 ± SD μmol CH_4 m^{-2} d^{-1}).

Station	**Latitude (°N)**	**Depth (m)**	**Mixed Layer Depth (m)**	**CH_{4BA} (nmol kg^{-1})**	**CH_{4D} (nmol kg^{-1})**	**U_{10AVE} (m s^{-1})**	**k (m d^{-1})**	**Air Sea CH_4 Flux ± SD (μmol CH_4 m^{-2} d^{-1})**	**Average CH_{4ML} (nmol kg^{-1})**
1	56.0585	2.5	28	2.93	5.41	10.56	1.96	4.9 ± 2.1	6.11
2	55.5958	3.6	34	2.89	4.29	10.52	1.97	2.7 ± 1.01	5.15
3	55.0803	6.2	38	2.77	2.35	10.79	2.10	-0.88±0.27	2.69
4	54.6602	10.8	38	2.76	2.61	10.87	2.12	-0.31±0.31	2.67
5	53.6671	25.5	38	2.74	3.67	9.61	1.90	1.8 ± 0.61	3.17
5.5	53.1551	3.5	NA	2.73	2.94	9.50	1.92	0.40 ± 0.32	NA
6	52.0020	3.8	38	2.72	2.60	9.53	1.90	-0.24±0.25	2.63
7	49.5002	4.7	36	2.67	2.77	6.57	1.34	0.13 ± 0.14	2.63
8	47.0001	28	30	2.60	2.65	7.16	1.50	0.08 ± 0.16	2.65
8.5	45.7690	3.5	NA	2.45	2.53	11.56	2.48	0.21 ± 0.40	NA
9	44.5003	6.4	34	2.50	2.77	11.50	2.52	0.68 ± 0.51	2.65
10	42.0003	3.5	36	2.42	2.41	7.56	1.71	-0.01±0.17	2.45
10.5	40.7278	3.5	NA	2.31	2.47	5.98	1.39	0.22 ± 0.12	NA
11	39.5002	3.6	38	2.29	2.18	5.53	1.32	-0.14±0.08	2.26
11.5	38.2812	3.5	NA	2.27	2.29	5.40	1.31	0.03 ± 0.09	NA

Table A.1 (continued)

Station	Latitude (°N)	Depth (m)	Mixed Layer Depth (m)	CH_{4BA} (nmol kg^{-1})	CH_{4D} (nmol kg^{-1})	U_{10AVE} (m s^{-1})	k (m d^{-1})	Air Sea CH_4 Flux ± SD (µmol CH_4 m^{-2} d^{-1})	$CH_{4ML\ AVE}$ (nmol kg^{-1})
12	37.0002	2.7	32	2.24	2.51	4.72	1.16	0.31± 0.09	2.33
12.5	35.7500	3.5	NA	2.22	2.19	7.25	1.79	-0.06±0.15	NA
13	34.4991	26.1	40	2.19	3.50	8.14	2.03	2.7 ± 0.79	3.50
13.5	33.2501	3.5	NA	2.17	2.40	6.12	1.55	0.35± 0.14	NA
14	32.0003	3.2	44	2.15	2.50	7.50	1.91	0.67± 0.25	2.57
15	29.4998	2.8	68	2.11	2.94	5.81	1.52	1.3 ± 0.26	2.80
15.5	28.2500	3.5	NA	2.10	2.52	3.98	1.05	0.4 ± 0.08	NA
16	26.9997	3.2	56	2.08	2.54	4.16	1.09	0.5 ± 0.09	2.86
17	24.4999	2.6	48	2.05	3.27	2.43	0.66	0.80 ±0.07	2.89
18	22.0004	40.9	56	2.03	2.57	5.46	1.52	0.81± 0.18	2.57
18.3	19.6808	4.2	18	2.00	3.36	4.30	1.22	1.7 ± 0.27	2.91
18.6	18.9064	3.6	64	1.99	2.86	8.96	2.51	2.2 ± 0.70	2.86
19	17.5000	3.1	44	1.95	2.39	8.33	2.37	1.04± 0.36	2.81
19.5	15.8621	3.5	NA	1.94	2.85	9.63	2.76	2.5 ± 0.87	NA
20	14.2517	2.9	34	1.93	3.36	7.06	2.02	2.9 ± 0.79	2.85
20.5	12.6250	3.5	NA	1.92	2.65	9.33	2.67	2.0 ± 0.66	NA
21	11.0002	3.2	20	1.91	2.68	7.05	2.05	1.6 ± 0.40	2.69
22	9.2472	2.4	24	1.89	3.01	6.48	1.90	2.1 ± 0.50	2.61
23	7.4995	2.3	36	1.88	2.31	4.90	1.44	0.62± 0.13	2.37

Table A.1 (continued)

Station	Latitude (°N)	Depth (m)	Mixed Layer Depth (m)	CH_{4BA} (nmol kg^{-1})	CH_{4D} (nmol kg^{-1})	U_{10AVE} (m s^{-1})	k (m d^{-1})	Air Sea CH_4 Flux ± SD(µmol CH_4 m^{-2} d^{-1})	$CH_{4ML\ AVE}$ (nmol kg^{-1})
25	5.0003	2.9	32	1.87	2.30	7.97	2.34	1.03 ± 0.33	3.20
27	2.4998	2.3	52	1.85	2.33	4.94	1.43	0.68 ± 0.13	2.36
29	0.0023	2.7	88	1.84	2.58	8.06	2.27	1.7 ± 0.46	2.52
31	-2.4998	2	80	1.87	2.28	5.17	1.48	0.62 ± 0.13	2.37
33	-5.0004	3.2	68	1.86	2.27	8.11	2.31	0.93 ± 0.31	2.28
33.5	-6.2500	3.5	NA	1.84	2.33	9.52	2.72	1.3 ± 0.47	NA
34	-7.5001	4.3	72	1.82	2.23	6.65	1.92	0.79 ± 0.21	2.42
34.5	-9.0000	3.5	NA	1.82	2.45	6.00	1.74	1.1 ± 0.23	NA
35	-10.5002	2.8	54	1.82	2.30	3.28	0.95	0.46 ± 0.06	2.27
35.5	-11.6250	3.5	NA	1.82	2.25	7.03	2.05	0.86 ± 0.24	NA
36	-12.7503	3.9	26	1.82	2.42	3.74	1.09	0.65 ± 0.09	2.40
37	-15.0001	2.6	10	1.83	2.34	3.23	0.94	0.48 ± 0.06	2.34
37.5	-16.2500	3.5	NA	1.83	2.25	3.51	1.01	0.42 ± 0.06	NA
38	-17.4999	3	28	1.85	2.44	7.14	2.05	1.2 ± 0.31	2.33
38.5	-18.7500	3.5	NA	1.87	2.38	5.71	1.60	0.81 ± 0.17	NA
39	-19.9998	3	44	1.89	2.59	4.44	1.24	0.87 ± 0.13	2.41

Table A.2 *Comparisons between hemispheres of methane air-sea exchange flux parameters*

Averages and standard deviations of various parameters that influence CH_4 flux. P values were used to determine if values observed in North Pacific were significantly different from those observed in the South Pacific. An asterisk indicates a significant p value (defined as $p < 0.05$). P values were determined using paired Student's two-tailed, unequal variance t test.

Parameter	North Pacific average ± standard deviation	South Pacific average ± standard deviation	p value
Average CH_4 flux ($\mu mol\ CH_4\ m^{-2}\ d^{-1}$)	1.01 ± 1.2	0.81 ± 0.28	> 0.05
Discrete CH_4 ($nmol\ kg^{-1}$)	2.8 ± 0.63	2.4 ± 0.104	< 0.001*
Bow air CH_4 ($nmol\ kg^{-1}$)	2.3 ± 0.34	1.8 ± 0.022	< 0.001*
Gas transfer velocity ($m\ d^{-1}$)	1.8 ± 0.501	1.6 ± 0.57	> 0.05
U_{10} wind speed ($m\ s^{-1}$)	7.4 ± 2.4	5.7 ± 2.0	< 0.05*

Table A.3 *Near-surface physical and chemical parameters at all stations*

A summary of parameters relating to near-surface conditions. Depth indicates shallowest CTD cast depth at each station. Red font indicates $[NO_3]$ and $[PO_4]$ measurements that were below detection ($\leq 0.02\ \mu mol\ kg^{-1}$).

Station	Latitude (°N)	Salinity	Temperature (°C)	Surface NO_3 ($\mu mol\ kg^{-1}$)	Surface PO_4 ($\mu mol\ kg^{-1}$)	Discrete CH_4 ($nmol\ kg^{-1}$)	Depth (m)
1	56.06	31.70	10.73	2.04	0.43	5.41	2.5
2	55.60	31.80	11.06	3.19	0.52	4.29	3.6
3	55.08	32.35	12.61	2.63	0.48	2.35	6.2
4	54.66	32.38	12.66	5.77	0.72	2.61	10.8
5	53.67	32.44	13.11	6.83	0.96	3.67	25.5
5.5	53.16	32.39	13.91	7.47	0.89	2.94	3.5
6	52.00	32.32	13.44	9.86	0.99	2.60	3.8

Table A.3 (continued)

Station	Latitude (°N)	Salinity	Temperature (°C)	Surface NO_3 (μmol kg^{-1})	Surface PO_4 (μmol kg^{-1})	Discrete CH_4 (nmol kg^{-1})	Depth (m)
7	49.50	32.24	14.26	9.89	1.03	2.77	4.7
8	47.00	32.24	15.21	4.72	0.72	2.65	28
8.5	45.77	32.38	16.37	2.62	0.55	2.53	3.5
9	44.50	32.37	17.11	0.93	0.42	2.77	6.4
10	42.00	32.94	18.44	0	0.23	2.41	3.5
10.5	40.73	33.01	19.41	0	0.25	2.47	3.5
11	39.50	33.26	20.54	0	0.14	2.18	3.6
11.5	38.28	33.57	21.23	0	0.08	2.29	3.5
12	37.00	33.85	21.88	0	0.05	2.51	2.7
12.5	35.75	34.03	22.01	0	0.05	2.19	3.5
13	34.50	34.50	22.52	0	0.01	3.50	26.1
13.5	33.25	34.99	23.00	0	0	2.40	3.5
14	32.00	35.09	23.26	0	0	2.50	3.2
15	29.50	35.37	24.35	0	0	2.94	2.8
15.5	28.25	35.29	24.78	0	0	2.52	3.5
16	27.00	35.39	24.68	0	0	2.54	3.2
17	24.50	34.73	25.96	0	0.06	3.27	2.6
18	22.00	34.68	27.15	0	0.07	2.57	40.9
18.3	19.68	34.45	27.69	0	0.05	3.36	4.2
18.6	18.91	34.67	27.35	0	0.04	2.86	3.6
19	17.50	34.36	27.97	0.12	0.09	2.39	3.1
19.5	15.86	33.75	28.39	0	0.1	2.85	3.5
20	14.25	33.82	28.27	0	0.11	3.36	2.9

Table A.3 (continued)

Station	Latitude (°N)	Salinity	Temperature (°C)	Surface NO_3 (µmol kg^{-1})	Surface PO_4 (µmol kg^{-1})	Discrete CH_4 (nmol kg^{-1})	Depth (m)
21	11.00	33.44	28.99	0	0.07	2.68	3.2
22	9.25	33.34	29.30	0	0.06	3.01	2.4
23	7.50	33.35	29.55	0	0.01	2.31	2.3
25	5.00	33.91	29.48	0	0.03	2.30	2.9
27	2.50	34.56	28.91	0.03	0.14	2.33	2.3
29	0.00	35.23	27.59	4.07	0.46	2.58	2.7
31	-2.50	35.45	28.30	3.41	0.36	2.28	2
33	-5.00	35.51	28.02	4.5	0.4	2.27	3.2
33.5	-6.25	35.53	28.16	4.2	0.45	2.33	3.5
34	-7.50	35.63	28.69	3.41	0.37	2.23	4.3
34.5	-9.00	35.78	28.88	1.66	0.25	2.45	3.5
35	-10.50	35.85	28.92	0.64	0.19	2.30	2.8
35.5	-11.63	35.98	29.01	0.23	0.14	2.25	3.5
36	-12.75	36.20	28.90	0.02	0.12	2.42	3.9
37	-15.00	35.97	28.84	0	0.1	2.34	2.6
37.5	-16.25	36.20	28.61	0.01	0.11	2.25	3.5
38	-17.50	36.14	28.36	0.01	0.1	2.44	3
38.5	-18.75	36.11	27.25	0.02	0.07	2.38	3.5
39	-20.00	36.08	27.13	0	0.05	2.59	3

Table A.4 *Summary of primary data including methane concentration (ppm)*

A summary of primary CH_4 data (ppm and nmol kg^{-1}), temperature, and salinity for each station, which were used in CH_4 flux calculations. BA means bow air, and D means discrete near-surface seawater. Depth indicates depth at which CH_{4D} was collected.

Station	Latitude (°N)	Depth (m)	Salinity	Temperature (°C)	CH_{4BA} (ppm)	CH_{4BA} (nmol kg^{-1})	CH_{4D} (ppm)	CH_{4D} (nmol kg^{-1})
1	56.0585	2.5	31.70	10.73	1.92	2.93	0.131	5.41
2	55.5958	3.6	31.80	11.06	1.92	2.89	0.106	4.29
3	55.0803	6.2	32.35	12.61	1.91	2.77	0.0639	2.35
4	54.6602	10.8	32.38	12.66	1.90	2.76	0.0675	2.61
5	53.6671	25.5	32.44	13.11	1.91	2.74	0.0694	3.67
5.5	53.1551	3.5	32.39	13.91	1.90	2.73	0.0759	2.94
6	52.0020	3.8	32.32	13.44	1.91	2.72	0.0642	2.60
7	49.5002	4.7	32.24	14.26	1.91	2.67	0.0722	2.77
8	47.0001	28	32.24	15.21	1.90	2.60	0.0690	2.65
8.5	45.7690	3.5	32.38	16.37	1.90	2.45	0.0663	2.53
9	44.5003	6.4	32.37	17.11	1.90	2.50	0.0719	2.77
10	42.0003	3.5	32.94	18.44	1.90	2.42	0.0634	2.41
10.5	40.7278	3.5	33.01	19.41	1.89	2.31	0.0633	2.47
11	39.5002	3.6	33.26	20.54	1.89	2.29	0.0559	2.18
11.5	38.2812	3.5	33.57	21.23	1.89	2.27	0.0608	2.29
12	37.0002	2.7	33.85	21.88	1.89	2.24	0.0654	2.51
12.5	35.7500	3.5	34.03	22.01	1.89	2.22	0.0595	2.19
13	34.4991	26.1	34.50	22.52	1.88	2.19	0.0886	3.50
13.5	33.2501	3.5	34.99	23.00	1.88	2.17	0.0581	2.40

Table A.4 (continued)

Station	Latitude (°N)	Depth (m)	Salinity	Temperature (°C)	CH_{4BA} (ppm)	CH_{4BA} (nmol kg^{-1})	CH_{4D} (ppm)	CH_{4D} (nmol kg^{-1})
14	32.0003	3.2	35.09	23.26	1.88	2.15	0.0624	2.50
15	29.4998	2.8	35.37	24.35	1.89	2.11	0.0761	2.94
15.5	28.2500	3.5	35.29	24.78	1.88	2.10	0.0635	2.52
16	26.9997	3.2	35.39	24.68	1.87	2.08	0.0649	2.54
17	24.4999	2.6	34.73	25.96	1.89	2.05	0.0839	3.27
18	22.0004	40.9	34.68	27.15	1.91	2.03	0.0661	2.57
18.3	19.6808	4.2	34.45	27.69	1.89	2.00	0.0863	3.36
18.6	18.9064	3.6	34.67	27.35	1.88	1.99	0.0700	2.86
19	17.5000	3.1	34.36	27.97	1.85	1.95	0.0590	2.39
19.5	15.8621	3.5	33.75	28.39	1.85	1.94	0.0670	2.85
20	14.2517	2.9	33.82	28.27	1.85	1.93	0.0823	3.36
20.5	12.6250	3.5	33.83	28.30	1.85	1.92	0.0639	2.65
21	11.0002	3.2	33.44	28.99	1.85	1.91	0.0636	2.68
22	9.2472	2.4	33.34	29.30	1.84	1.89	0.0713	3.01
23	7.4995	2.3	33.35	29.55	1.84	1.88	0.0564	2.31
25	5.0003	2.9	33.91	29.48	1.84	1.87	0.0564	2.30
27	2.4998	2.3	34.56	28.91	1.82	1.85	0.0575	2.33
29	0.0023	2.7	35.23	27.59	1.81	1.84	0.0637	2.58
31	-2.4998	2	35.45	28.30	1.80	1.87	0.0555	2.28
33	-5.0004	3.2	35.51	28.02	1.79	1.86	0.0554	2.27
33.5	-6.2500	3.5	35.53	28.16	1.78	1.84	0.0574	2.33
34	-7.5001	4.3	35.63	28.69	1.77	1.82	0.0549	2.23

Table A.4 (continued)

Station	Latitude (°N)	Depth (m)	Salinity	Temperature (°C)	CH_{4BA} (ppm)	CH_{4BA} (nmol kg^{-1})	CH_{4D} (ppm)	CH_{4D} (nmol kg^{-1})
34.5	-9.0000	3.5	35.78	28.88	1.77	1.82	0.0598	2.45
35	-10.5002	2.8	35.85	28.92	1.78	1.82	0.0569	2.30
35.5	-11.6250	3.5	35.98	29.01	1.78	1.82	0.0544	2.25
36	-12.7503	3.9	36.20	28.90	1.78	1.82	0.0577	2.42
37	-15.0001	2.6	35.97	28.84	1.78	1.83	0.0573	2.34
37.5	-16.2500	3.5	36.20	28.61	1.79	1.83	0.0540	2.25
38	-17.4999	3	36.14	28.36	1.79	1.85	0.0597	2.44
38.5	-18.7500	3.5	36.11	27.25	1.79	1.87	0.0568	2.38
39	-19.9998	3	36.08	27.13	1.78	1.89	0.0544	2.59

Figure A.1 *Bow air methane extrapolation*

Polynomial fit (0.00023x2 + 0.0034x +1.84) used to extrapolate bow air CH_4 concentration (nmol kg^{-1}) in data gaps of GP15 cruise between 20 °N and 5 °S when CRDS analyzer was turned off. Green dots are measured bow air CH_4 concentrations, and green dashed line is polynomial fit for these data. Yellow dots are extrapolated bow air CH_4 concentrations using polynomial fit.

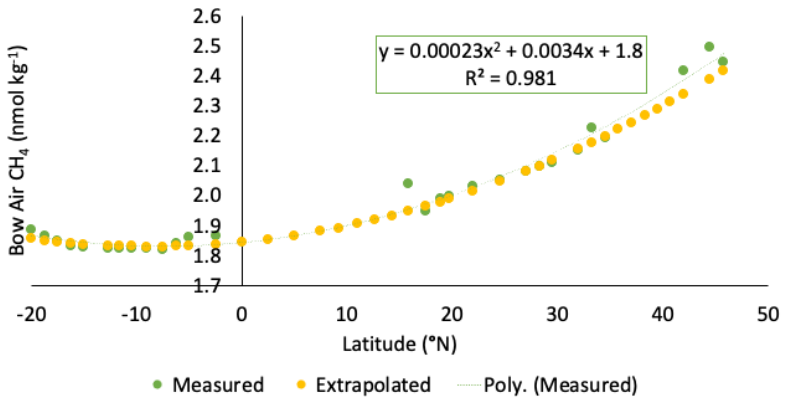

Figure A.2 *Methane concentration for entire transect*

Methane (CH_4) concentration (nmol kg^{-1}) for GP15 transect. Black dots indicate sampling locations.

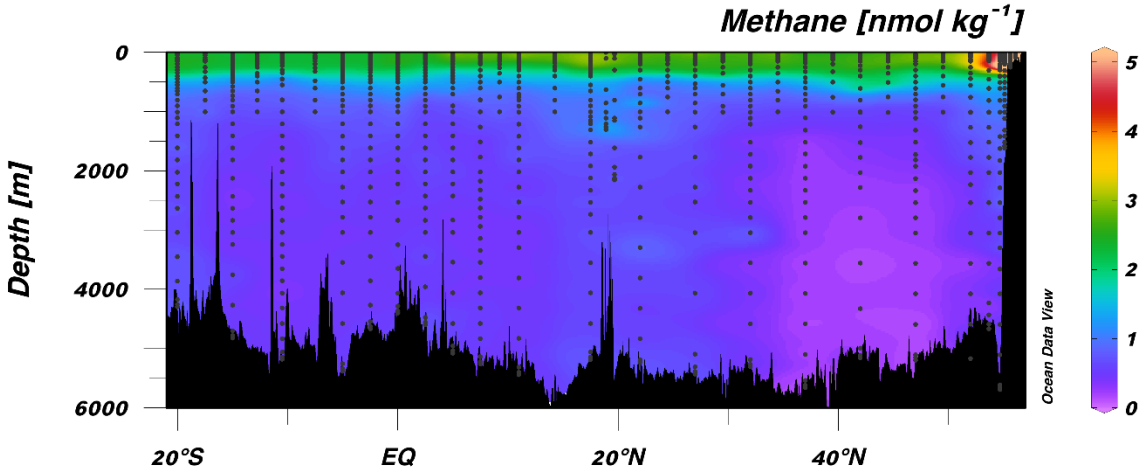

Figure A.3 *N* in mixed layer with latitude*

Nitrate star (N*) in mixed layer (N^*_{ML}; µmol kg^{-1}) with latitude (°N) for GP15 transect. Values calculated using equation $N^* = [NO_3] - 16[PO_4] + 2.9$ as described in Gruber and Sarmiento (1997).

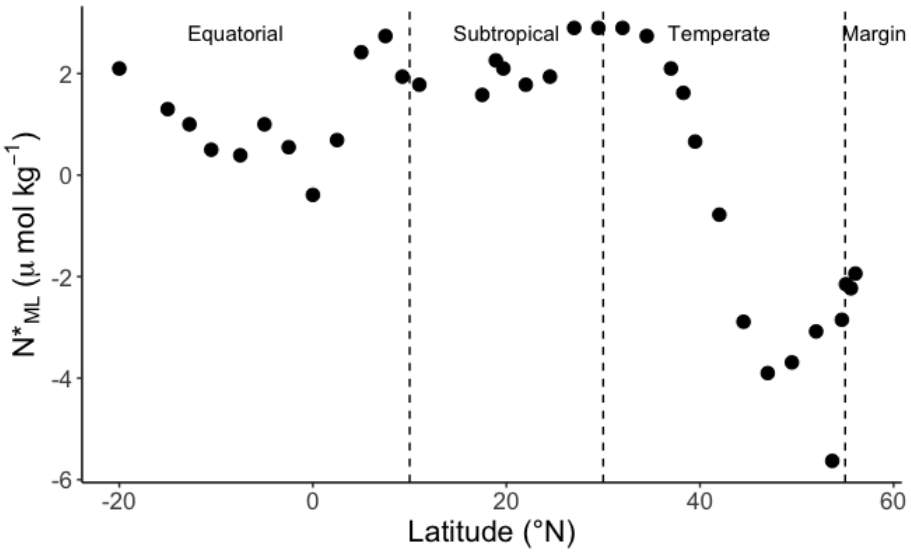

Figure A.4 *P* in mixed layer with latitude calculated using oxygen*

Phosphate star (P*) in mixed layer (P^*_{ML}; µmol kg^{-1}) with latitude (°N) for GP15 transect using equation P* = $[PO_4]$ – (1/175) x [dissolved O_2] as described in Broecker et al. (1998). Black triangles indicate $[PO_4]$ measurements that were above detection, and open triangles indicate $[PO_4]$ measurements that were below detection ($\leq$ 0.02 µmol kg^{-1}). Stations where dissolved oxygen measurements were unavailable are excluded. Dashed lines at 10 °N, 30 °N, and 55 °N represent changes in regime from Equatorial North and South Pacific to Subtropical North Pacific to Temperate North Pacific and to Alaskan Margin, respectively.

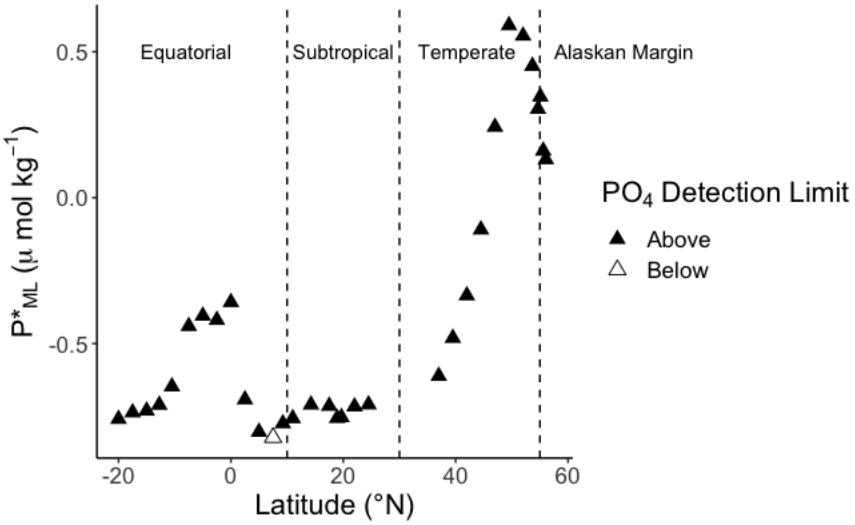

Figure A.5 *Praseodymium concentration in upper 500 m*

Praseodymium (Pr) concentration (pmol kg^{-1}) upper 500 m for GP15 transect. Black dots indicate sampling locations.

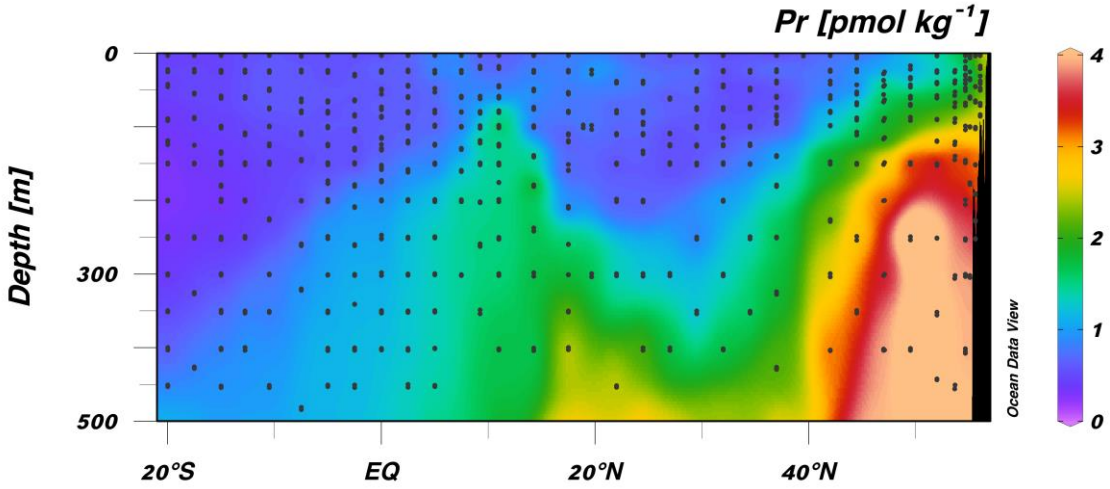

Figure A.6 *Neodymium concentration in upper 500 m*

Neodymium (Nd) concentration (pmol kg^{-1}) in upper 500 m for GP15 transect. Black dots indicate sampling locations.

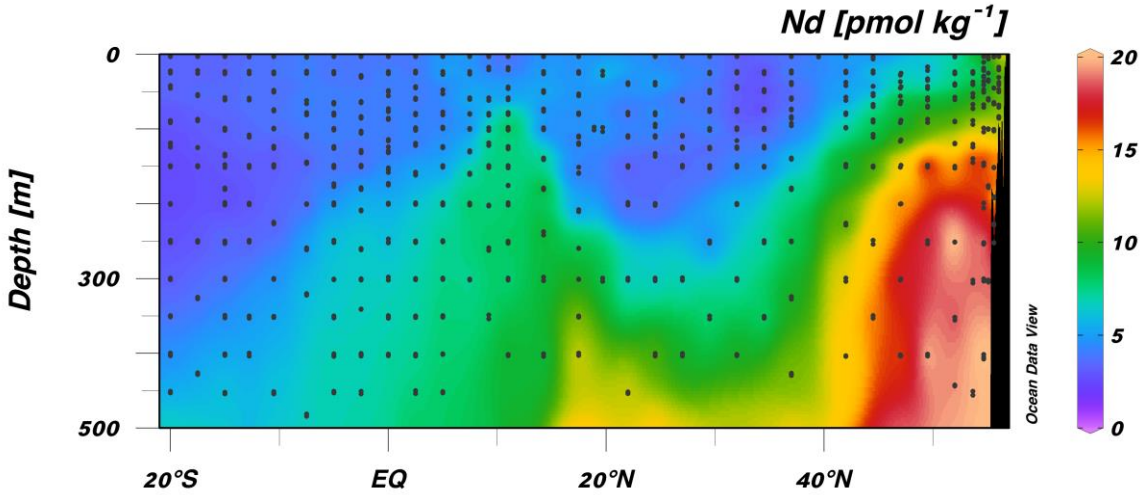

Figure A.7 *Methane air-sea exchange fluxes with lanthanum anomaly for open ocean stations*

Methane air-sea fluxes (µmol m^{-2} d^{-1}) with lanthanum (La) anomaly for open ocean stations (4-39). The linear regression (blue line) is y = -0.356x + 2.043 (R = 0.276).

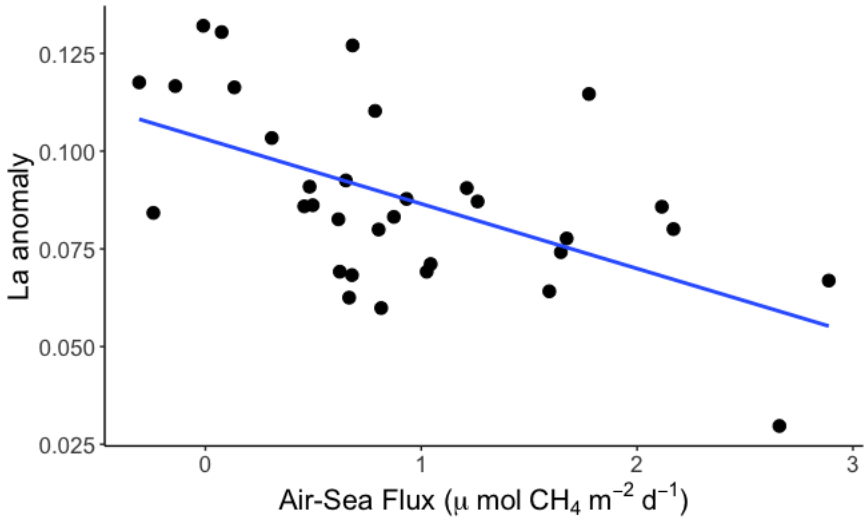

Figure A.8 *Cerium concentration for entire transect*

Cerium (Ce) concentration (pmol kg^{-1}) for GP15 transect. Black dots indicate sampling locations.

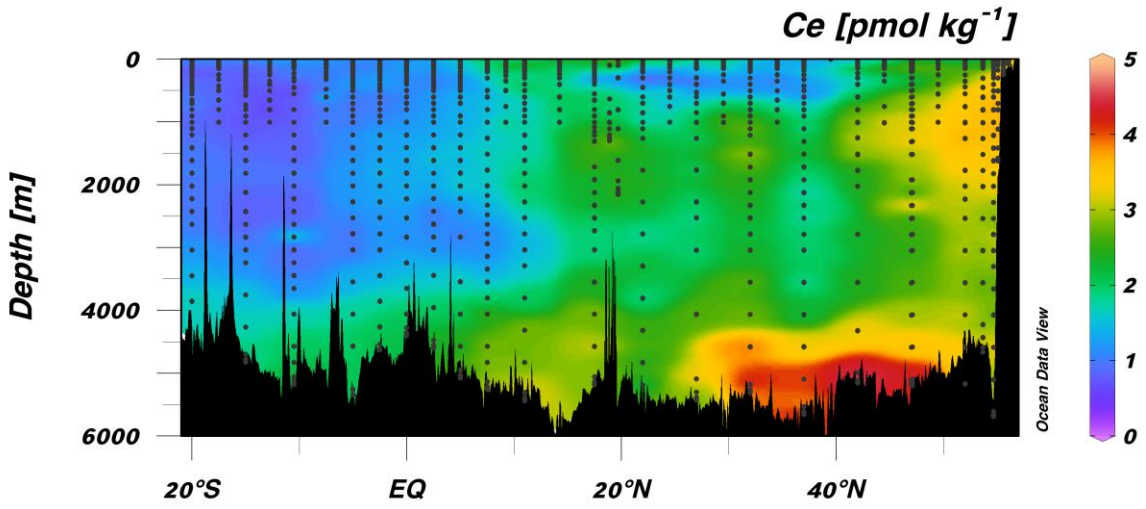

Figure A.9 *Lanthanum concentration for entire transect*

Lanthanum (La) concentration (pmol kg^{-1}) for GP15 transect. Black dots indicate sampling locations.

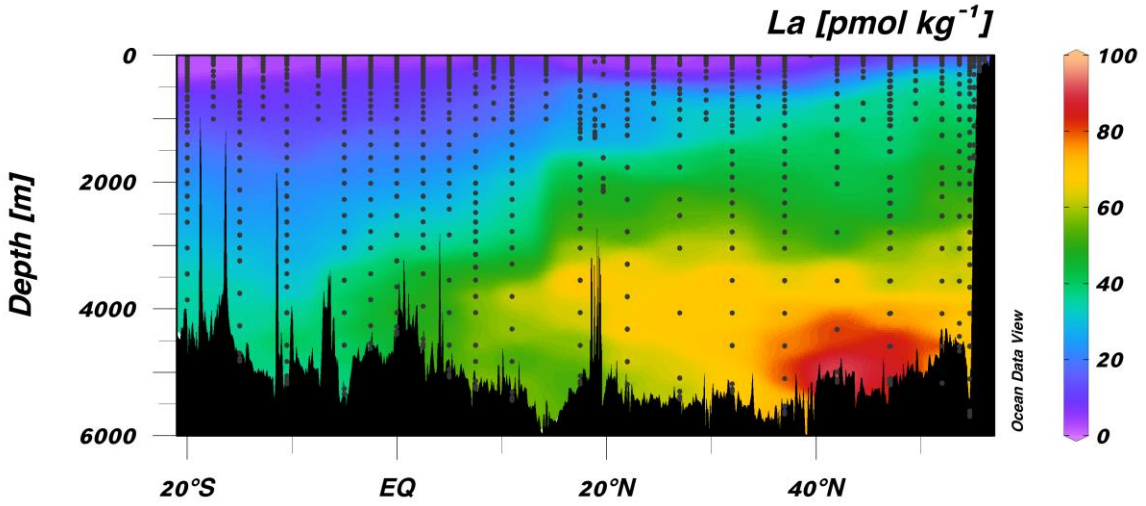

Figure A.10 *La anomaly for entire transect*

Lanthanum (La) anomaly for GP15 transect. Black dots indicate sampling locations. “Positive” and “negative” anomalies are determined relative to 1, meaning colors in red to yellow are positive, and colors in blue are negative anomalies.

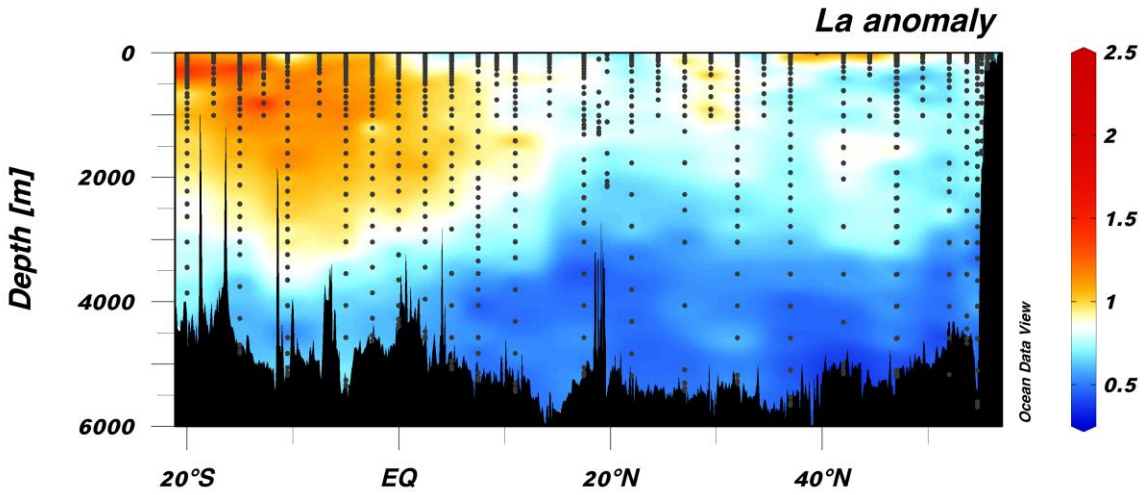

Figure A.11 *Lanthanum to ytterbium ratio for entire transect*

Lanthanum (La) to ytterbium (Yb) ratio for GP15 transect. Black dots indicate sampling locations.

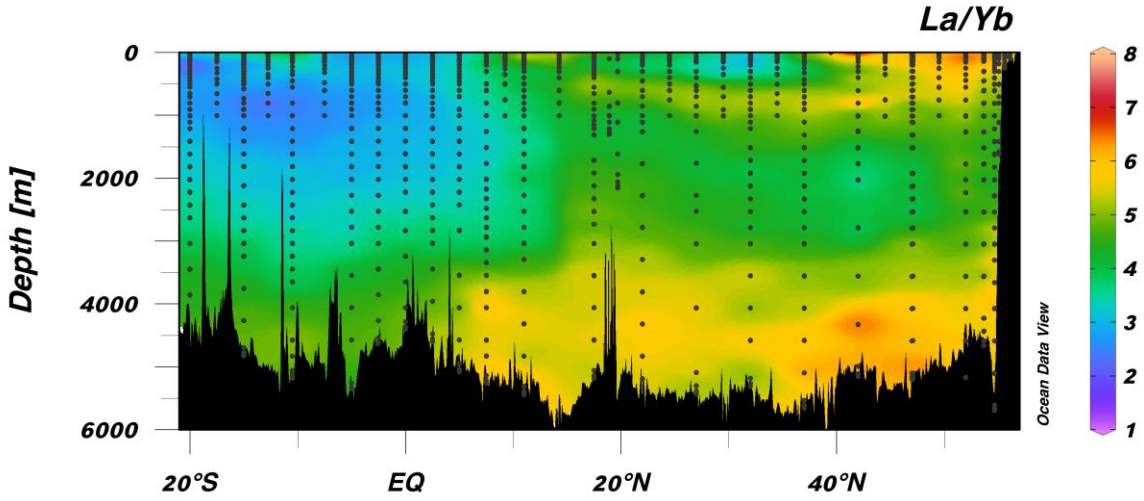

Figure A.12 *Light rare elements to heavy rare earth elements ratio for entire transect*

Light rare earth elements (LREEs) to heavy rare earth elements (HREEs) ratio for GP15 transect. LREEs include La, Pr, and Nd. HREEs include Sm, Eu, Gd, Tb, Dy, Ho, Er, Tm, Yb, and Lu. Black dots indicate sampling locations.

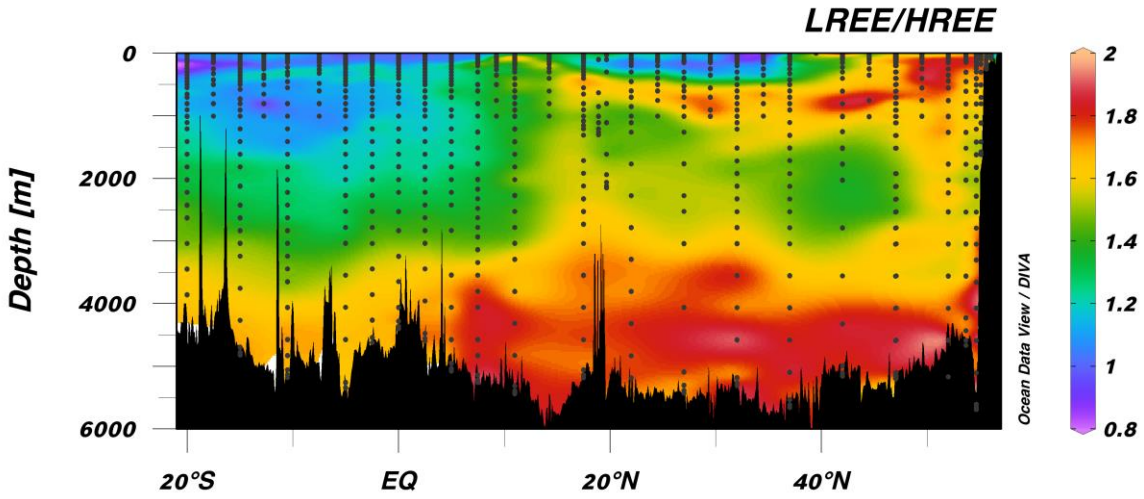

Figure A.13 *Manganese concentration for entire transect*

Manganese (Mn) concentration (nmol kg^{-1}) for GP15 transect. Black dots indicate sampling locations.

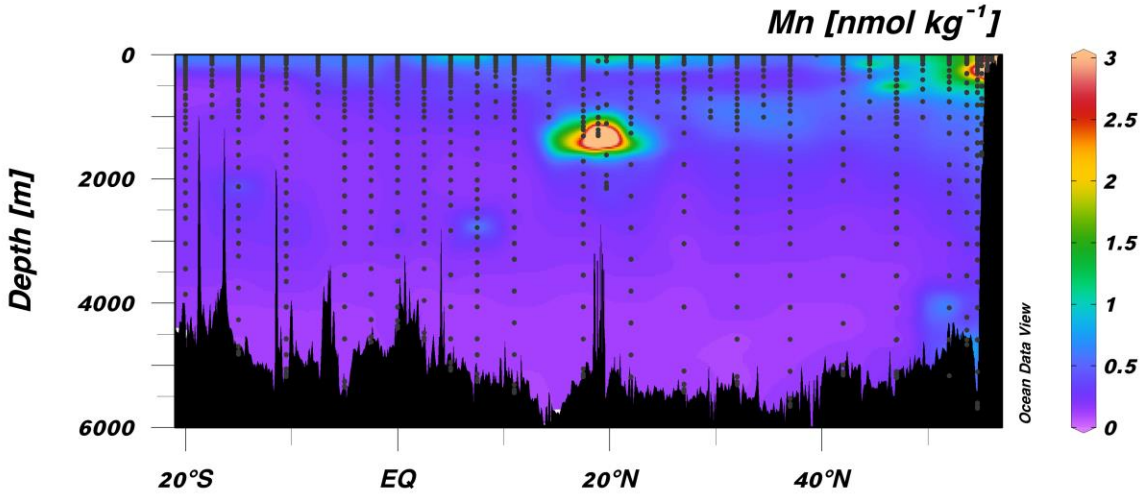

Figure A.14 *Praseodymium concentration for entire transect*

Praseodymium (Pr) concentration (pmol kg^{-1}) for GP15 transect. Black dots indicate sampling locations.

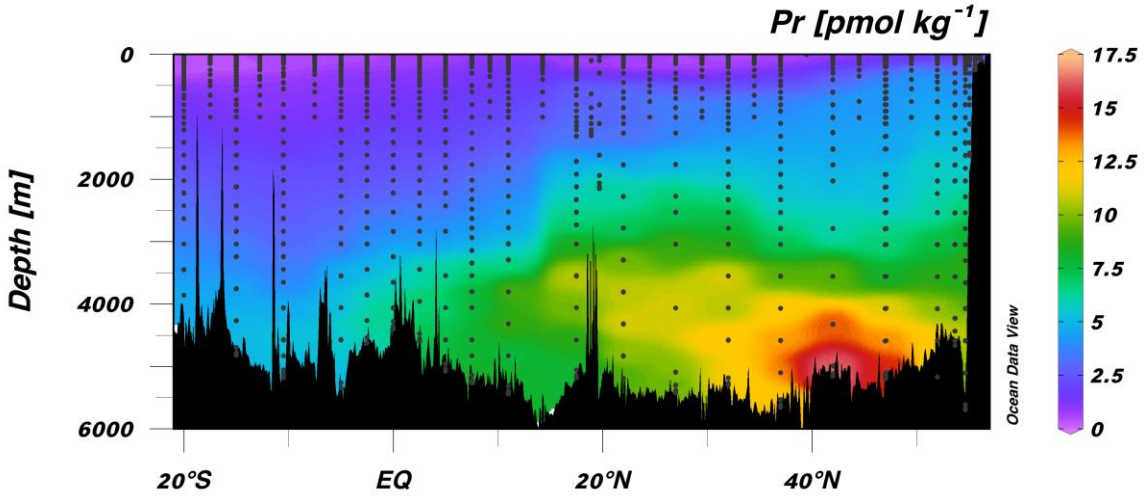

Figure A.15 *Neodymium concentration for entire transect*

Neodymium (Nd) concentration (pmol kg^{-1}) for GP15 transect. Black dots indicate sampling locations.

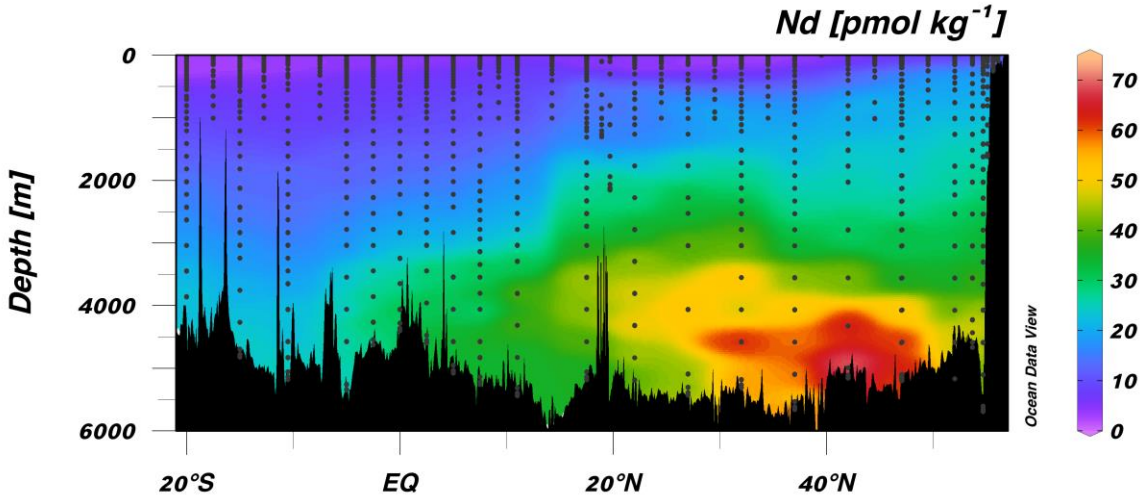

Figure A.16 *Ytterbium concentration for entire transect*

Ytterbium concentration (pmol kg^{-1}) for GP15 transect. Black dots indicate sampling locations.

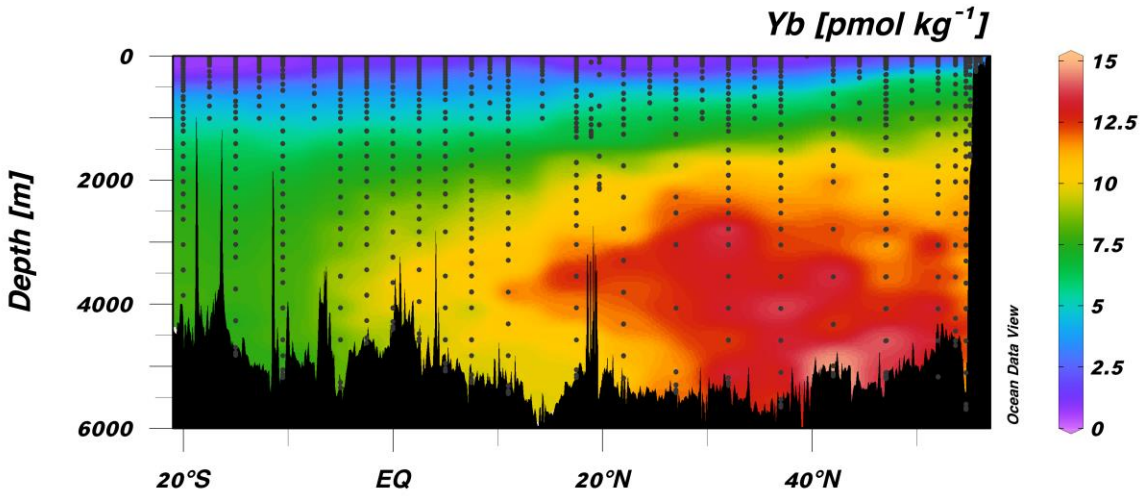

Figure A.17 *Copper concentration for entire transect*

Copper concentration (nmol kg^{-1}) for GP15 transect. Black dots indicate sampling locations.

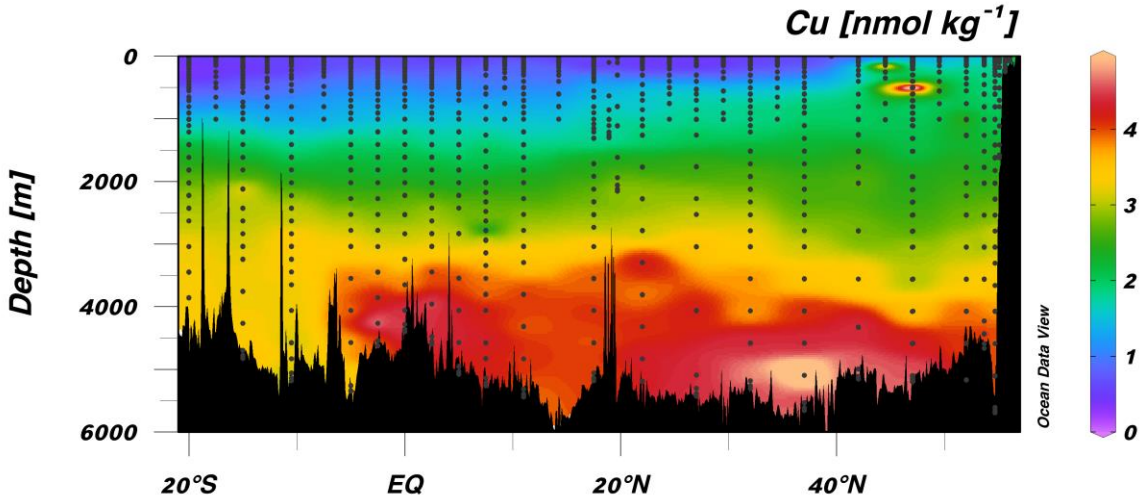

Figure A.18 *Nickel concentration for entire transect*

Nickel (Ni) concentration (nmol kg^{-1}) for GP15 transect. Black dots indicate sampling locations.

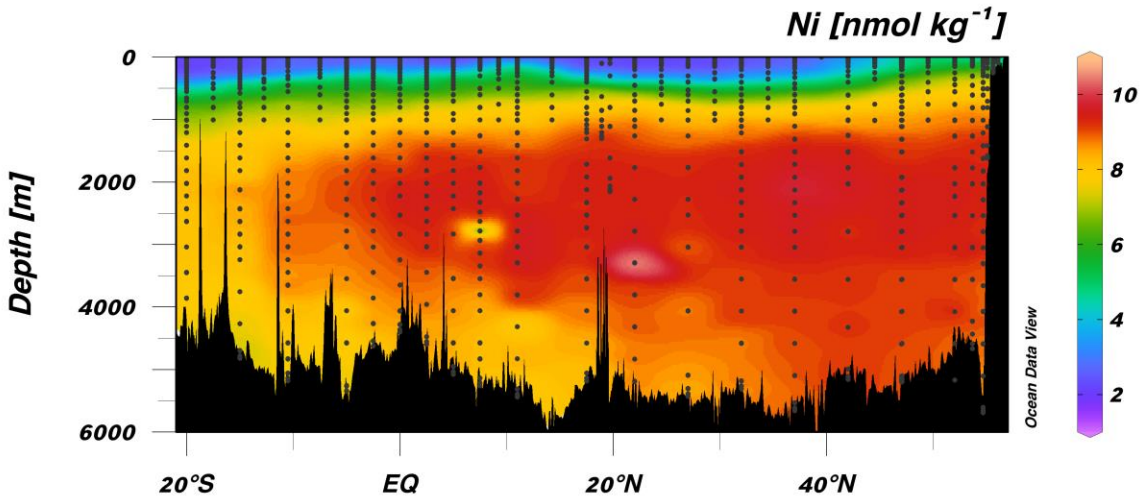

REFERENCES

Alibo, D.S. and Y. Nozaki. 1999. Rare earth elements in seawater: Particle association, shale-normalization, and Ce oxidation. Geochim. Cosmochim. Acta. 63, 363-372.

Anderson, L.A., and J.L. Sarmiento. 1994. Redfield ratios of remineralization determined by nutrient data analysis. Global Biogeochem. Cy. 8(1), 65-80.

Bange, H.W. et al. 1994. Methane in the Baltic and North Seas and a reassessment of the marine emissions of methane. Global Biogeochem. Cy. 8, 4, 465-480.

Bange, H. W. et al. 2009. MEMENTO: a proposal to develop a database of marine nitrous oxide and methane measurements. Environ. Chem. 6, 195-197. DOI: 10.1071/en09033.

Bates, T.S. et al. 1996. A reevaluation of the open ocean source of methane to the atmosphere. J. Geophys. Res. 101(D3), 6953-6961.

Beal, E.J., C.H. House, and V.J. Orphan. 2009. Manganese- and iron-dependent marine methane oxidation. Sci. 325, 184-187.

Becker, S. et al. 2019. GO-SHIP repeat hydrography manual: The precise and accurate determination of dissolved inorganic nutrients in seawater, using continuous flow analysis methods. In: GO-SHIP Repeat Hydrography Manual: A Collection of Expert Reports and Guidelines. Version 1.1, [56pp.]. DOI: http://dx.doi.org/10.25607/OBP-555. Available online at: http://www.go-ship.org/HydroMan.html

Bishop, J.K.B. and T.J. Wood. 2009. Year-round observations of carbon biomass and flux variability in the Southern Ocean. Global Biogeochem. Cy. 23, GB2019.

Bižić, M., et al. 2020. Aquatic and terrestrial cyanobacteria produce methane. Sci. Adv. 6, 5343.

Borges, A.V. et al. 2016. Massive marine methane emissions from near-shore coastal areas. Nat. Sci. Reports. 6, 27908; doi: 10.1038/srep27908

Borges, A.V. et al. 2017. Productivity and temperature as drivers of seasonal and spatial variations of dissolved methane in the Southern Bight of the North Sea. Ecosys. DOI: 10.1007/s10021-017-0171-7

Broecker et al. 1998. How much deep water is formed in the Southern Ocean? J. Geophys. Res. 103(C8), 15833-15843.

Burke Jr., R.A. et al. 1983. Upper water column methane geochemistry in the eastern tropical North Pacific. Limnol. Oceanogr. 28(1), 19-32.

Burnett, W.C., K.K. Roe, and D.Z. Piper. 1983. Upwelling and phosphorite formation in the ocean. In: Coastal Upwelling its Sediment Record. Eds. E. Suess and J. Thiede. Springer, Boston, MA, 1983. 377-397.

Casciotti, K., Cutter, G., Lam, P. 2020. CTD profiles from the ODF rosette on the US GEOTRACES Pacific Meridional Transect (PMT) cruise (GP15) from September to November 2018. Biological and Chemical Oceanography Data Management Office (BCO-DMO). (Version 2) Version Date 2020-07-22. doi:10.26008/1912/bco-dmo.778168.2 Access Date 2021-12-29.

Casciotti, K. L., Cutter, G. A., Lam, P. J. 2021a. Bottle file from Leg 1 (Seattle, WA to Hilo, HI) of the US GEOTRACES Pacific Meridional Transect (PMT) cruise (GP15, RR1814) on R/V Roger Revelle from September to October 2018. Biological and Chemical Oceanography Data Management Office (BCO-DMO). (Version 6) Version Date 2021-05-05. doi:10.26008/1912/bco-dmo.777951.6 Access Date 2021-12-29.

Casciotti, K. L., Cutter, G. A., Lam, P. J. 2021b. Bottle file from Leg 2 (Hilo, HI to Papeete, French Polynesia) of the US GEOTRACES Pacific Meridional Transect (PMT) cruise (GP15, RR1815) on R/V Roger Revelle from October to November 2018. Biological and Chemical Oceanography Data Management Office (BCO-DMO). (Version 5) Version Date 2021-05-05. doi:10.26008/1912/bco-dmo.824867.5 Access Date 2021-12-29.

Chan, E. W. et al. 2019. Investigations of aerobic methane oxidation in two marine seep environments: Part 1—Chemical kinetics. J. Geophys. Res.: Oceans, 124, 8852-8868. https://doi.org/10.1029/2019JC015594

Charlou et al. 1998. Intense CH_4 plumes generated by serpentinization of ultramafic rocks at the intersection of the 15°20’N fracture zone and the Mid-Atlantic Ridge. Geochim. Et Cosmo. Acta. 62, 13, 2323-2333.

Chistoserdova, L. 2019. New pieces to the lanthanide puzzle. Mol. Microbio. 0(0), 1-5. doi:10.1111/mmi.14210.

Chronopoulou, P-M. et al. 2017. Origin and fate of methane in the Eastern Tropical North Pacific oxygen minimum zone. Int. Soc. Microb. Ecol. 11, 1386-1399.

Ciais, P., C. et al. 2013. Carbon and Other Biogeochemical Cycles. In: Climate Change 2013: The Physical Science Basis. Contribution of Working Group I to the Fifth Assessment Report of the Intergovernmental Panel on Climate Change [Stocker, T.F., D. Qin, G.-K. Plattner, M. Tignor, S.K. Allen, J. Boschung, A. Nauels, Y. Xia, V. Bex and P.M. Midgley (eds.)]. Cambridge University Press, Cambridge, United Kingdom and New York, NY, USA.

Conrad, R., and W. Seiler. 1988. Methane and hydrogen in seawater (Atlantic Ocean). Deep Sea Res. Part A. Oceanogr. Res. Papers. 35(12), 1903-1917).

Cook, P.J. and C.M. Carleton [eds]. 2000. Continental Shelf Limits: The Scientific and Legal Interface. Oxford University Press.

Crespo-Medina, M. et al. 2014. The rise and fall of methanotrophy following a deepwater oil-well blowout. Nat. Geosci. 7(6), 423–427. https://doi.org/10.1038/NGEO2156

Cutter, G.A., and K.W. Bruland. 2012. Rapid and noncontaminating system for trace elements in global ocean surveys. Limnol. Oceanogr. Methods. 10, 425-436.

Cutter, G. et al. 2017. Sampling and sample-handling protocols for GEOTRACES cruises. https://geotracesold.sedoo.fr/images/Cookbook.pdf

Cynar, F.J. and A.A. Yayanos. 1992. The distribution of methane in the upper waters of the southern California Bight. J. Geophys. Res. 97, C7, 11269-11285.

D'Hondt, S. et al. 2004. Distributions of microbial activities in deep subseafloor sediments. Sci. 306, 2216-2221.

Daumann, L.J. 2019. Essential and ubiquitous: The emergence of lanthanide metallobiochemistry. Angew. Chem. Int. Ed. 58, 12795-12802. DOI:10.1002/anie.201904090

DeAngelis, M.A., M.D. Lilley, and J.A. Baross. 1993. Methane oxidation in deep-sea hydrothermal plumes of the endeavour segment of the Juan de Fuca Ridge. Deep Sea Res. Part 1: Oceanogr. Res. Papers. 40, 6: 1169-1186.

De Baar, H.J.W. et al. 2018. Low cerium among dissolved rare earth elements in the central North Pacific Ocean. Geochim. Cosmochim. Acta. 236, 5-40.

Del Valle, D.A. and D.M. Karl. 2014. Aerobic production of methane from dissolved water-column methylphosphonate and sinking particles in the North Pacific Subtropical Gyre. Aquat. Microbiol. Ecol. 73, 93-105.

Deutsch, C., et al. 2001. Denitrification and N_2 fixation in the Pacific Ocean. Global Biogeochem. Cy. 15(2), 483-506.

Dlugokencky, E. 2021. Trends in CH_4. NOAA/GML. www.esrl.noaa.gov/gmd/ccgg/trends_ch4/

Dugdale, R.C., and J.J. Goering. 1967. Uptake of new and regenerated forms of nitrogen in primary productivity. Limnol. Oceanogr. 12, 196-206.

Forster, G. et al. 2009. Nitrous oxide and methane in the Atlantic Ocean between 50 N and 52 S: Latitudinal distribution and sea-to-air flux. Deep Sea Res. Part II Top. Stud. Oceanogr. 56(15), 964-976.

Ganachaud A, and C. Wunsch. 2000. Improved estimates of global ocean circulation, heat transport and mixing from hydrographic data transport. Nat. 408: 453–57.

Glover, D., S. Doney, and W.J. Jenkins. 2011. Modeling Methods in Marine Science. Cambridge University Press.

Gruber, N., and J.L. Sarmiento. 1997. Global patterns of marine nitrogen fixation and denitrification. Global Biogeochem. Cy. 11(2), 235-266.

Hamdan, L.J. and K.P. Wickland. 2016. Methane emissions from oceans, coasts, and freshwater habitats: New perspectives and feedbacks on climate. Limnol. Oceanogr. 61, S3-S12.

Hartmann, D. L., Klein Tank, A. M. G., Rusticucci, M. & Alexander, L. V. in Climate Change 2013 – The Physical Science Basis: Working Group I Contribution to the Fifth Assessment Report of the Intergovernmental Panel on Climate Change (ed. Change Intergovernmental Panel on Climate) 159–254 (Cambridge University Press, 2014).

Hathorne, E.C., et al. 2012. Online preconcentration ICP-MS analysis of rare earth elements in seawater. Geochem. Geophys. Geosyst. 13(1), doi:10.1029/2011GC003907

Ho, P. et al. 2018. The distribution of dissolved and particulate Mo and V along the U.S. GEOTRACES East Pacific Zonal Transect (GP16): The roles of oxides and biogenic particles in their distributions in the oxygen deficient zone and the hydrothermal plume. Mar. Chem. 201, 242-255.

Holmes, M.E., et al. 2000. Methane production, consumption, and air-sea exchange in the open ocean: An evaluation based on carbon isotopic ratios. Global Biogeochem. Cy. 14(1), 1-10.

Hsu, S.A., E.A. Meindl, and D.B. Gilhousen. Determining the power-law wind-profile exponent under near-neutral stability conditions at sea. J. Appl. Meteorol. 33, 757-765.

Huang, J., Yu, Z., & Chistoserdova, L. 2018. Lanthanide-dependent methanol dehydrogenases of XoxF4 and XoxF5 clades are differentially distributed among methylotrophic bacteria and they reveal different biochemical properties. Front. Microbiol. 9(1366). https://doi.org/10.3389/fmicb.2018.01366

Jenkins, W.J. et al. 2020. An intermediate-depth source of hydrothermal ^{3}He and dissolved iron in the North Pacific. Earth Planet. Sci. Letters. 539, 116223. https://doi.org/10.1016/j.epsl.2020.116223

Jensen, L.T., et al. 2020. Assessment of stability, sorption, and exchangeability of marine dissolved and colloidal metals. Mar. Chem. 220, 103754. https://doi.org/10.1016/j.marchem.2020.103754

Jensen, S. et al. 2008. Methane assimilation and trophic interactions with marine Methylomicrobium in deep-water coral reef sediment off the coast of Norway. FEMS Microbiol. Ecol. 66(2), 320-330.

Johnson, J.E. 1999. Evaluation of a seawater equilibrator for shipboard analysis of dissolved oceanic trace gases. Anal. Chim. Acta. 395, 119-132.

Kalyuzhnaya, M. G., Yang, S., Rozova, O., Smalley, N., Clubb, J., Lamb, A., et al. 2013. Highly efficient methane biocatalysis revealed in a methanotrophic bacterium. Nat. Comm., 4, 2785. https://doi.org/10.1038/ncomms3785

Karl, D.M. et al. 2008. Aerobic production of methane in the sea. Nat. Geosci. 1, 473-478.

Kelly, T.B. 2019. _TheSource: It will hold your beer. Zenodo. DOI: 10.5281/zenodo.3468524

Kimura, T. et al. 1999. Isolation and characterization of two marine methanotrophs from coastal sediments. Fish. Sci. 65(4), 558-562.

Kirschke, S. et al. 2013. Three decades of global methane sources and sinks. Nat. Geosci. 6(10), 813-823.

Klintzsch ,T. et al. 2019. Methane production by three widespread marine phytoplankton species: release rates, precursor compounds, and potential relevance for the environment. Biogeosci. 16, 4129-4144. https://doi.org/10.5194/bg-16-4129-2019

Lagerstrom, M.E., et al. 2013. Automated on-line flow-injection ICP-MS determination of trace metals (Mn, Fe, Co, Ni, Cu, and Zn) in open ocean seawater: Application to the GEOTRACES program. Mar. Chem. 155, 71-80.

Lenhart, K. et al. 2016. Evidence for methane production by the marine algae *Emiliania huxleyi*. Biogeosci, 13, 3163– 3174, https://doi.org/10.5194/bg-13-3163-2016

Levitus, S. 1982. Climatological atlas of world ocean. NOAA Professional Paper 13.

Lim, S. and S.J. Franklin. 2004. Lanthanide-binding peptides and the enzymes that might have been. Cell. Mol. Life Sci. 61, 2184-2188. Doi:10.1007/s00018-004-4156-2.

Massee, R., F.J.M.J. Maessen, and J.J.M. De goeij. 1981. Losses of silver, arsenic, cadmium, selenium and zinc traces from distilled water and artificial sea-water by sorption on various container surfaces. Anal. Chim. Acta. 127, 181-193.

Mau, S. et al. 2013. Vertical distribution of methane oxidation and methanotrophic response to elevated methane concentrations in stratified waters of the Arctic fjord Storfjorden (Svalbard, Norway). Biogeosci. 10(10), 6267-6278.

McGinnis, D. F. et al. 2006. Fate of rising methane bubbles in stratified waters: How much methane reaches the atmosphere? J. Geophys. Res. 111, https://doi.org/10.1029/2005jc003183

Metcalf, W.W. et al. 2012. Synthesis of methylphosphonic acid by marine microbes: A source for methane in the aerobic ocean. Sci. 337, 1104-1107.

Meyer, A.C.S., D. Grundle, and J.T. Cullen. 2021. Selective uptake of rare earth elements in marine systems as an indicator of and control on aerobic bacterial methanotrophy. Earth Planet. Sci. Letters. 558, 116756. https://doi.org/10.1016/j.epsl.2021.116756

Mofflet, J.W. 1994. The relationship between cerium and manganese oxidation in the marine environment. Limnol. Oceanogr. 39, 1309-1318.

Monterey, G. and S. Levitus. 1997. Seasonal variability of the global ocean mixed layer depth. NOAA Atlas NESDIS 14.

Pack, M.A. et al. 2015. Methane oxidation in eastern tropical North Pacific Ocean water column. J. Geophys. Res. Biogeosci. 120. doi:10.1002/2014JG002900.

Paytan, A. and K. McLaughlin. 2007. The oceanic phosphorus cycle. Chem. Rev. 107(2), 563-576. https://doi.org/10.1021/cr0503613

Picone, N. and H.J.M. Op den Camp. 2019. Role of rare earth elements in methanol oxidation. Curr. Opin. Chem. Biol. 49, 39–44. https://doi.org/10.1016/j.cbpa.2018.09.019

Pol, A. et al. 2014. Rare earth metals are essential for methanotrophic life in volcanic mudpots. Environ. Microbiol. 16 (1), 255-264. https://doi.org/10.1111/1462-2920.12249

Popp, B.N. et al. 1995. Determination of concentration and carbon isotopic composition of dissolved methane in sediments and nearshore waters. Anal. Chem. 67 (2), 405-411.

R Core Team. 2021. R: A language and environment for statistical computing. R Foundation for Statistical Computing, Vienna, Austria. https://www.R-project.org/.

Redfield, A.C. 1934. On the proportions of organic derivatives in sea water and their relation to the composition of plankton. James Johnstone memorial volume, 176-192.

Reeburgh, W.S. 2007. Oceanic methane biogeochemistry. Chem. Rev. 107, 486-513.

Repeta, D.J. 2016. Marine methane paradox explained by bacterial degradation of dissolved organic matter. Nat. Geosci. 9, doi:10.1038/NGEO2837.

Rhee, T.S., A.J. Kettle, and M.O. Andreae. 2009. Methane and nitrous oxide emissions from the ocean: A reassessment using basin-wide observations in the Atlantic. J. Geophys. Res. 114, D12304. doi:10.1029/2008JD011662

Roberts, H.M. and A.M. Shiller. 2015. Determination of dissolved methane in natural waters using headspace analysis with cavity ring-down spectroscopy. Anal. Chim. Acta. 856: 68-73.

Ruppel, C. D., & Kessler, J. D. 2017. The interaction of climate change and methane hydrates. Rev. of Geophys, 55(1), 126–168. https://doi.org/10.1002/2016RG000534

Schlitzer, R. 2021. Ocean Data View. https://odv.awi.de

Schmale, O. et al. 2018. The contribution of zooplankton to methane supersaturation in the oxygenated upper waters of the central Baltic Sea. Limnol. Oceanogr. 63, 412-430.

Scranton, M.I. and P.G. Brewer. 1977. Consumption of dissolved methane in the deep ocean. Limnol. Oceanogr. 23(6): 1207-1213.

Semrau, J.D. et al. 2018. Metals and Methanotrophy. Appl. Environ. Microbiol. 84, e002289-17. https://doi.org/10.1128/AEM.02289-17

Shelley, F. et al. 2017. Bringing methanotrophy in rivers out of the shadows. Limnol. Oceanogr. 62, 2345-2359.

Shiller, A.M. 2010. Dissolved rare earth elements in a seasonally snow-covered, alpine/subalpine watershed, Loch Vale, Colorado. Geochim. Et Cosmo. Acta. 74, 2040-2052.

Shiller, A. M. 2021a. Dissolved concentrations of Ba, Cd, Cu, Ga, Mn, Nd, Ni, and Pb from Leg 1 (Seattle, WA to Hilo, HI) of the US GEOTRACES Pacific Meridional Transect (PMT) cruise (GP15, RR1814) on R/V Roger Revelle from September to October 2018. Biological and Chemical Oceanography Data Management Office (BCO-DMO). (Version 3) Version Date 2021-05-12. doi:10.26008/1912/bco-dmo.835589.3 Access Date 2021-12-29.

Shiller, A. M. 2021b. Dissolved concentrations of Ba, Cd, Cu, Ga, Mn, Nd, Ni, and Pb from Leg 2 (Hilo, HI to Papeete, French Polynesia) of the US GEOTRACES Pacific Meridional Transect (PMT) cruise (GP15, RR1815) on R/V Roger Revelle from Oct-Nov 2018. Biological and Chemical Oceanography Data Management Office (BCO-DMO). (Version 2) Version Date 2021-05-12. doi:10.26008/1912/bco-dmo.836121.2 Access Date 2021-12-29.

Shiller, A.M. et al. 2017. Light rare earth element depletion during Deepwater Horizon blowout methanotrophy. Nat. Sci. Rep. 7: 10389.

Sosa, O.A. et al. 2019. Phosphate-limited ocean regions select for bacterial populations enriched in the carbon-phosphorus lyase pathway for phosphonate degradation. Environ. Microbiol. 21, 2402-2414.

Tilbrook, B.D. and D.M. Karl. 1995. Methane sources, distributions and sinks from California coastal waters to the oligotrophic North Pacific gyre. Mar. Chem. 49, 1, 51-64.

Valentine et al. 2001. Water column methane oxidation adjacent to an area of active hydrate dissociation, Eel River Basin. Geochim. Et Cosmo. Acta. 65(16): 2633-2640.

Wang, Q. et al. 2021. Aerobic bacterial methane synthesis. PNAS. 118(27), e2019229118. Doi:10.1073/pnas.2019229118.

Wang, X., J.-A. Barrat, G. Bayon, L. Chauvaud, and D. Feng. 2020. Lanthanum anomalies as fingerprints of methanotrophy. Geochem. Persp. Let. 14, 26-30. doi:10.7185/geochemlet.2019

Wanninkhof, R. 2014. Relationship between wind speed and gas exchange over the ocean revisited. Limnol. Oceanogr.: Methods 12: 351-362.

Ward, B.B. 1992. The subsurface methane maximum in the Southern California Bight. Cont. Shelf Res. 12, 5-6: 735-752.

Ward, B. B. and K. A. Kilpatrick. 1993. Methane oxidation associated with mid-depth methane maxima in the Southern California Bight. Cont. Shelf Res. 13, 1111–1122.

Weber, T.W., N.A. Wiseman, and A. Kock. 2019. Global ocean methane emissions dominated by shallow coastal waters. Nat. Comm. 10: 4584.

White, A.K. and W.W. Metcalf. 2007. Microbial metabolism of reduced phosphorus compounds. Annu. Rev. Microbiol. 61:379-400.

Wiesenburg, D.A. and N.L. Guinasso. 1979. Equilibrium solubilities of methane, carbon monoxide, and hydrogen in water and sea water. J. Chem. Eng. Data. 24, 4, 356-360.

Yoshikawa, C. et al. 2014. Methane sources and sinks in the Subtropical South Pacific along 17 ºS as traced by stable isotope ratios. Chem. Geol. 382, 24-31.

Zachos, J.C. et al. 2001. Trends, rhythms, and aberrations in global climate 65 Ma to present. Sci. 292, 686-693.

Zachos, J.C., Dickens, G.R., and Zeebe, R.E. 2008. An early Cenozoic perspective on greenhouse warming and carbon-cycle dynamics. Nat. 451, 279-283. doi:10.1038/nature06588

Zhang, X. et al. 2011. In situ Raman-based measurements of high dissolved methane concentrations in hydrate-rich sediments. J. Geophys. Res. Lett. 38, L08605. Doi:10.1029/2011GL04714.